

**University of Nebraska - Lincoln**  
**DigitalCommons@University of Nebraska - Lincoln**

---

Mechanical (and Materials) Engineering --  
Dissertations, Theses, and Student Research

Mechanical & Materials Engineering, Department  
of

Fall 12-2011

# Anisotropic Thermal Property Measurement of Carbon-fiber/Epoxy Composite Materials

Tian Tian  
*University of Nebraska-Lincoln*, [yuersunny@gmail.com](mailto:yuersunny@gmail.com)

Follow this and additional works at: <http://digitalcommons.unl.edu/mechengdiss>

 Part of the [Heat Transfer, Combustion Commons](#)

---

Tian, Tian, "Anisotropic Thermal Property Measurement of Carbon-fiber/Epoxy Composite Materials" (2011). *Mechanical (and Materials) Engineering -- Dissertations, Theses, and Student Research*. Paper 27.  
<http://digitalcommons.unl.edu/mechengdiss/27>

This Article is brought to you for free and open access by the Mechanical & Materials Engineering, Department of at DigitalCommons@University of Nebraska - Lincoln. It has been accepted for inclusion in Mechanical (and Materials) Engineering -- Dissertations, Theses, and Student Research by an authorized administrator of DigitalCommons@University of Nebraska - Lincoln.

ANISOTROPIC THERMAL PROPERTY MEASUREMENT OF  
CARBON-FIBER/EPOXY COMPOSITE MATERIALS

by

Tian Tian

A DISSERTATION

Presented to the Faculty of  
The Graduate College at the University of Nebraska  
In Partial Fulfillment of Requirements  
For the Degree of Doctor of Philosophy

Major: Interdepartmental Area of Engineering

(Mechanical Engineering)

Under the Supervision of Professor Kevin D. Cole

Lincoln, Nebraska

December 2011

# ANISOTROPIC THERMAL PROPERTY MEASUREMENT OF CARBON-FIBER/EPOXY COMPOSITE MATERIALS

Tian Tian, Ph. D.

University of Nebraska, 2011

Advisor: Kevin D. Cole

This work originated from a need for understanding heat transfer in carbon-fiber/epoxy natural-gas tanks undergoing rapid heating during refilling. The dissertation is focused on the determination of the anisotropic thermal properties of carbon-fiber/epoxy composite materials for in-plane and through-thickness directions. An effective anisotropic parameter estimation system consisting of the  $3\omega$  experimental technique and an anisotropic two-dimensional heat transfer model is developed.

In the present work, the  $3\omega$  method, an experimental technique that has been well established to evaluate the thermal properties of isotropic materials, especially thin film materials, is extended to treat the thermal properties of bulk anisotropic materials. A platinum film deposited on the sample surface is periodically heated by a sinusoidally oscillating current at frequency  $\omega$ , and thereby causes a time-harmonic electrical resistance variation at frequency  $2\omega$ . The heat-induced resistance variation at frequency  $2\omega$  coupled with the current at frequency  $\omega$  produces a voltage variation component at frequency  $3\omega$ . The phase and amplitude data of the voltage signal at frequency  $3\omega$  are collected from the experiment. An impedance analysis model is employed to convert the voltage data to temperature data.

The anisotropic thermal properties are deduced from an inverse parameter estimation model, which is a least-square systematic comparison between experimental data and the theoretical model. The anisotropic theoretical model is based on the Green's function approach. A careful sensitivity analysis is used to demonstrate the feasibility of simultaneous estimation of the in-plane and through-thickness thermal conductivities. Poly methyl methacrylate (PMMA) samples were applied as reference samples to verify the measurement system. The parameter estimation result for experimental data from PMMA samples agree very well with handbook values. Experimental results from carbon-fiber/epoxy samples are presented.

## Acknowledgement

The author owes an immense debt of gratitude to her advisor, Kevin D. Cole, for his guidance and encouragement, for his knowledge and relaxed demeanor, for the countless long conversations and small chats, and especially for providing her the academic freedom to work at her own pace throughout research for this dissertation. With fervent admiration, the author would also like to thank Dr. Cole for being everything a true scholar should be. It has been a great fortune and honor to have had his advising and mentoring.

Grateful acknowledgement is extended to the other members of the guidance committee: Dr. John Barton, Dr. Zhaoyan Zhang, and Dr. Florin Bobaru, for their helpful discussions, suggestions and challenges.

Sincere appreciation goes to Dr. Mathias Schubert. His instruction on experimental design and his help with subsequent analysis was invaluable. The success of this experimental work would not have been possible without his gracious involvement.

Many thanks go to Dr. Hao Wang and Dr. Xiaojun Wu for the stimulating and inspiring discussions that provided much-needed clarity on this and other matters. Their friendship and professional insight has meant a great deal.

The author would like to thank the current department chair, Dr. Jeffery Shield, for his tremendous understanding and support. The author is also greatly indebted to the previous department chair, Dr. David Lou, who introduced her to UNL.

Essential recognition goes to all the author's colleagues at Nutech Ventures, for the opportunity to work in a professional learning environment, for the warm memories of happy hours, and for the many new and lasting friendships she has made there.

With gratitude the author acknowledges Ai Pheeng Wee, Brian Todd Sink, Emily Kisling, Eric Montgomery, Fiona Nah, Jian Zhou, Kris Reiswig, Mark Stroup, Nan Rowe, Paul Marxhausen, Summayia Khan, Xi He, and YuyanXue who have offered help and warmed her heart.

Special thanks go to Jessica Zhang, Philip Onyeforo and Haorong Li for all the love, care and support, for being a pillar of strength, and for being there through her good and bad times.

And never enough thanks, to the one who prefers to remain unnamed. He is content to be known to himself and to the author.

Finally, the author's deepest appreciation goes to her parents, whose love and support is always the first reason she is able to do anything of value.

# **Table of Contents**

**Abstract**

**Acknowledgement**

**List of tables**

**List of figures**

**List of symbols**

**Chapter 1 Introduction.....** 1

    1.1 Motivations ..... 1

    1.2 Dissertation outline ..... 4

**Chapter 2 Literature review .....** 6

    2.1 Thermal property estimation of composite materials ..... 6

        2.1.1 Based on constituent components..... 6

        2.1.2 Based on heat transfer measurement ..... 8

        2.1.3 Comparison of the two approaches ..... 10

    2.2 The  $3\omega$  method..... 11

        2.2.1 The  $3\omega$  method on isotropic materials..... 12

        2.2.2 The  $3\omega$  method on anisotropic materials ..... 15

**Chapter 3 Forward model development.....** 22

    3.1 Anisotropic heat transfer model..... 22

        3.1.1 Assumptions ..... 22

        3.1.2 Anisotropic heat transfer equations ..... 23

3.1.3 Converting the anisotropic model to isotropic.....	24
<b>3.2 Analytical temperature solution.....</b>	<b>26</b>
3.2.1 Introduction .....	26
3.2.2 Temperature solution in time domain.....	27
3.2.3. Improvement of series convergence .....	31
3.2.4 Temperature solution in frequency domain.....	36
3.2.5 Average temperature solution.....	38
3.2.6 Comparison of the temperature solutions .....	39
<b>3.3 Phase results.....</b>	<b>41</b>
3.3.1 Parameters in the analytical solution .....	42
3.3.2 The influence of convection .....	43
3.3.3 The effect of thickness.....	45
3.3.4 The effect of $k_x$ and $k_y$ .....	47
<b>3.4 Sensitivity analysis.....</b>	<b>48</b>
3.4.1 The effect of $l_0$ and $a_0$ on the sensitivity coefficients .....	49
3.4.2 The best frequency range for estimating $k_x$ and $k_y$ .....	50
<b>3.5 Summary .....</b>	<b>51</b>
<b>Chapter 4 Experiment .....</b>	<b>62</b>
4.1 Experimental principle.....	62
4.2 Sample preparation .....	62
4.3 Experimental setup.....	64

4.4 System Calibration.....	67
4.5 Impedance analysis model .....	69
4.6 Experimental results.....	72
4.7 Chapter Summary .....	78
<b>Chapter 5 Parameter estimation: Results and discussion.....</b>	<b>96</b>
5.1 Overview.....	96
5.2 Results for PMMA samples .....	100
5.3 Results for carbon fiber sample .....	106
5.4 Conclusion .....	110
<b>Chapter 6 Conclusions and future work.....</b>	<b>127</b>
6.1 Conclusions.....	127
6.2 Future work.....	130
<b>Reference .....</b>	<b>132</b>
<b>Appendix A.....</b>	<b>146</b>
<b>Appendix B. ....</b>	<b>155</b>

## **List of tables**

Table 5. 1 Summary of the IPE results of PMMA samples.....	105
Table 5. 2 Summary of the IPE results of carbon fiber samples.....	108
Table 5. 3 Thermal conductivity of carbon-fiber/epoxy composite from literature .....	110

## List of figures

Figure 1. 1 Structure of carbon-fiber/epoxy composite .....	5
Figure 2. 1 Fundamental element used in the analogy between transverse heat transfer and longitudinal shear loading by Springer <i>et al.</i> .....	17
Figure 2. 2 Fundamental element used in the analogy between transverse thermal resistance and electrical resistance by Dasgupta <i>et al.</i> .....	17
Figure 2. 3 Schematic of Behhzad <i>et al.</i> 's experimental set-up.....	18
Figure 2. 4 Schematic of Sweeting <i>et al</i> 's experimental set-up .....	18
Figure 2. 5 The hot disk sensor and the conduction model used by Kalaprasad <i>et al.</i> ....	19
Figure 2. 6 Schematic of Birge <i>et al</i> 's experimental setup .....	20
Figure 2. 7 Schematic of Hou <i>et al</i> 's experimental setup .....	21
Figure 2. 8 Schematic of Wang <i>et al</i> 's experimental setup .....	21
Figure 3.1 Heat transfer geometry .....	53
Figure 3.2 Verification of the two analytical temperature solutions numerically .....	54
Figure 3.3 Phase versus frequency for various Biot number .....	54
Figure 3.4 Phase at large Biot for various values of $c_0$ .....	55
Figure 3.5 Phase at small Biot for various values of $c_0$ .....	55
Figure 3.6 Phase versus frequency for various values of $W_0$ .....	56
Figure 3.7 Phase versus frequency for various values of $l_0$ with fixed $W_0$ .....	56
Figure 3.8 Phase versus frequency for various values of $l_0$ with fixed $a_0$ .....	57
Figure 3.9 Phase versus frequency for various values of $a_0$ with fixed $l_0$ .....	57
Figure 3.10 Phase versus frequency for various values of $k_x$ with fixed $k_y$ .....	58
Figure 3.11 Phase versus frequency for various values of $k_y$ with fixed $k_x$ .....	58
Figure 3.12 Sensitivity of phase to $k_x$ for various values of $k_x$ and $k_y$ .....	59
Figure 3.13 Sensitivity of phase to $k_y$ for various values of $k_x$ and $k_y$ .....	59
Figure 3.14 Sensitivity of phase to $k_x$ and $k_y$ .....	60
Figure 3.15 Sensitivity of phase to $k_x$ for various values of $a_0$ and $l_0$ .....	60
Figure 3.16 Sensitivity of phase to $k_y$ for various values of $a_0$ and $l_0$ .....	61

Figure 4. 1 A photographic picture of the carbon-fiber composite sample and a schematic picture of a platinum film .....	80
Figure 4. 2 The AJA sputter system used for deposition.....	80
Figure 4. 3 Result from X-ray reflectively measurement of platinum film on one .....	81
Figure 4. 4 Schematic of the $3\omega$ experimental setup with the Wheatston bridge using a lock-in amplifier as the ac power source .....	82
Figure 4. 5 Photographic picture of SR 830 Lock-in amplifier .....	82
Figure 4. 6 Schematic diagram of the amplifier circuit .....	83
Figure 4. 7 Schematic experimental setup considering the effect of cable capacitance in the circuit .....	84
Figure 4. 8 Amplitude results from NRM measurement with varied resistance combination.....	85
Figure 4. 9 Phase results from NRM measurement with varied resistance .....	86
Figure 4. 10 Curve fit of experimental amplitude and phase data from NRM data and Eq. (4.7) and (4.8) to get the capacitance of cables.....	87
Figure 4. 11 Amplitude of $U_{AB}^{3\omega}$ collected from measurement (Sample P#6) .....	88
Figure 4. 12 Phase of $U_{AB}^{3\omega}$ collected from measurement (Sample P#6) .....	88
Figure 4. 13 Phase of $U_{AB}^{3\omega}$ collected from measurement (Sample P#6) .....	89
Figure 4. 14 Phase of $U_{AB}^{3\omega}$ collected from measurement (Sample P#6) .....	89
Figure 4. 15 Amplitude of calculated $T(2\omega)$ from IA model (Sample P#6).....	90
Figure 4. 16 Phase of calculated $T(2\omega)$ from IA model (Sample P#6).....	90
Figure 4. 17 Amplitude of $U_{AB}^{3\omega}$ collected from measurement (Sample P#8) .....	91
Figure 4. 18 Phase of $U_{AB}^{3\omega}$ collected from measurement (Sample P#8) .....	91
Figure 4. 19 Phase of $U_{AB}^{3\omega}$ collected from measurement (Sample P#8) .....	92
Figure 4. 20 Phase of $U_{AB}^{3\omega}$ collected from measurement (Sample P#8) .....	92
Figure 4. 21 Amplitude of calculated $T(2\omega)$ from IA model (Sample P#8).....	93
Figure 4. 22 Phase of calculated $T(2\omega)$ from IA model (Sample P#8).....	93
Figure 4. 23 Amplitude of $U_{AB}^{3\omega}$ collected from measurement (Sample C#7).....	94
Figure 4. 24 Phase of $U_{AB}^{3\omega}$ collected from measurement (Sample C#7) .....	94
Figure 4. 25 Amplitude of calculated $T(2\omega)$ from IA model (Sample C#7) .....	95
Figure 4. 26 Phase of calculated $T(2\omega)$ from IA model (Sample C#7) .....	95

Figure 5. 1 The basic idea of inverse parameter estimation .....	112
Figure 5. 2 Amplitude and phase used for curve fitting (P#6E#1) .....	113
Figure 5. 3 Amplitude and phase used for curve fitting (P#6E#2) .....	113
Figure 5. 4 Curve-fitting the amplitude and phase data (P#6E#1) .....	114
Figure 5. 5 Curve-fitting the amplitude and phase data (P#6E#2) .....	114
Figure 5. 6 Amplitude and phase used for curve fitting (P#8E#1) .....	115
Figure 5. 7 Amplitude and phase used for curve fitting (P#8E#2) .....	115
Figure 5. 8 Curve-fitting the amplitude and phase data (P#8E#1) .....	116
Figure 5. 9 Curve-fitting the amplitude and phase data (P#8E#2) .....	116
Figure 5. 10 Amplitude and phase used for curve fitting (P#10E#1) .....	117
Figure 5. 11 Amplitude and phase used for curve fitting (P#10E#2) .....	117
Figure 5. 12 Curve-fitting the amplitude and phase data (P#10E#1) .....	118
Figure 5. 13 Curve-fitting the amplitude and phase data (P#10E#2) .....	118
Figure 5. 14 Amplitude and phase used for curve fitting (P#14E#1) .....	119
Figure 5. 15 Amplitude and phase used for curve fitting (P#14E#2) .....	119
Figure 5. 16 Amplitude and phase used for curve fitting (P#14E#3) .....	120
Figure 5. 17 Curve-fitting the amplitude and phase data (P#14E#1) .....	120
Figure 5. 18 Curve-fitting the amplitude and phase data (P#14E#2) .....	121
Figure 5. 19 Curve-fitting the amplitude and phase data (P#14E#3) .....	121
Figure 5. 20 Amplitude and phase used for curve fitting (C#7E#1).....	122
Figure 5. 21 Curve-fitting the amplitude and phase data (C#7E#1).....	122
Figure 5. 22 Amplitude and phase used for curve fitting (C#8E#2).....	123
Figure 5. 23 Curve-fitting the amplitude and phase data (C#8E#2).....	123
Figure 5. 24 Amplitude and phase used for curve fitting (C#13E#2).....	124
Figure 5. 25 Curve-fitting the amplitude and phase data (C#13E#2).....	124
Figure 5. 26 Amplitude and phase used for curve fitting (C#16E#2).....	125
Figure 5. 27 Curve-fitting the amplitude and phase data (C#16E#2).....	125
Figure 5. 28 Photos of the surface of samples C#7, #8, #13 and #16.....	126
Figure A. 1 Amplitude of $U_{AB}^{3\omega}$ collected from measurement (Sample P#9) .....	149
Figure A. 2 phase of $U_{AB}^{3\omega}$ collected from measurement (Sample P#9) .....	149

Figure A. 3 Amplitude of calculated $T(2\omega)$ from IA model (Sample P#9) .....	150
Figure A. 4 Amplitude of $U_{AB}^{3\omega}$ collected from measurement (Sample P#10) .....	150
Figure A. 5 Amplitude of $U_{AB}^{3\omega}$ collected from measurement (Sample P#10) .....	151
Figure A. 6 Amplitude of $U_{AB}^{3\omega}$ collected from measurement (Sample P#10) .....	151
Figure A. 7 Amplitude of calculated $T(2\omega)$ from IA model (Sample P#10) .....	152
Figure A. 8 phase of calculated $T(2\omega)$ from IA model (Sample P#10) .....	152
Figure A. 9 Amplitude of $U_{AB}^{3\omega}$ collected from measurement (Sample P#14) .....	153
Figure A. 10 phase of $U_{AB}^{3\omega}$ collected from measurement (Sample P#14) .....	153
Figure A. 11 Amplitude of calculated $T(2\omega)$ from IA model (Sample P#14).....	154
Figure A. 12 phase of calculated $T(2\omega)$ from IA model (Sample P#14).....	154
Figure B. 1 Amplitude of collected from measurement (Sample C#8) .....	156
Figure B. 2 Phase of collected $U_{AB}^{3\omega}$ from measurement (Sample C#8).....	156
Figure B. 3 Amplitude of collected $U_{AB}^{3\omega}$ from measurement (Sample C#13) .....	157
Figure B. 4 Phase of calculated $T(2\omega)$ from IA model (Sample C#13) .....	157
Figure B. 5 Amplitude of $U_{AB}^{3\omega}$ collected from measurement (Sample C#16) .....	158
Figure B. 6 Phase of $U_{AB}^{3\omega}$ collected from measurement (Sample C#16) .....	158
Figure B. 7 Amplitude of calculated $T(2\omega)$ from IA model (Sample C#8).....	159
Figure B. 8 Phase of calculated $T(2\omega)$ from IA model (Sample C#8) .....	159
Figure B. 9 Amplitude of calculated $T(2\omega)$ from IA model (Sample C#13).....	160
Figure B. 10 Phase of calculated $T(2\omega)$ from IA model (Sample C#13) .....	160
Figure B. 11 Amplitude of calculated $T(2\omega)$ from IA model (Sample C#16).....	161
Figure B. 12 Phase of calculated $T(2\omega)$ from IA model (Sample C#16) .....	161

## List of symbols

$a$	width of platinum heater in converted coordinate system, $m$
$a_0$	actual width of platinum heater, $m$
$a_{02}$	$=a/(2c)$
$A$	$=c/l$
$A_{U_{AB}^{3\omega}}$	amplitude of measured signal $U_{AB}^{3\omega}$ , $V$
$B_2$	Biot number, $=h_2 l/k$
$B_3$	Biot number, $=h_3 c/k$
$c$	half-length of sample in converted coordinate system, $m$
$c_0$	actual half-length of sample in converted coordinate system, $m$
$C_{a,b}$	Capacitance of the cable connecting point A and lock-in amplifier, $pF$
$D_p$	penetration depth, $m$
$f$	frequency, $Hz$
$G$	Green function (GF)
$G_{X23}$	Green function for boundary condition X23
$G_{Y23}$	Green function for boundary condition Y23
$G_{X23Y23}$	Green function for two dimensional geometry
$h_{20}$	heat transfer coefficient at $y=l_0$ , $W/(m^2K)$
$h_{30}$	heat transfer coefficient at $x=c_0$ , $W/(m^2K)$
$h_2$	heat transfer coefficient at $y=l$ , $W/(m^2K)$
$h_3$	heat transfer coefficient at $x=c$ , $W/(m^2K)$
$H$	$= h_2 / h_3$
$k_c$	thermal conductivity of composite , $W/(m^2K)$

$k_f$	thermal conductivity of fiber, $W/(m^2K)$
$k_m$	thermal conductivity of matrix, $W/(m^2K)$
$k_x$	in-plane thermal conductivity, $W/(m^2K)$
$k_y$	through-thickness thermal conductivity, $W/(m^2K)$
$k$	reference thermal conductivity, $=(k_x k_y)^{1/2}$ , $W/(m^2K)$
$l_0$	actual thickness of sample, $m$
$l$	sample thickness in converted coordinate system, $m$
$P$	$=\alpha \left( \frac{\beta_m^2}{l^2} + \frac{\beta_n^2}{c^2} \right)$ , Eq. (3.28)
$q$	$=Q\cos^2(\omega t)$ , Eq. (3.20)
$Q$	quantity of heat transfer, $W/m^2$
$R$	$=\frac{k\sigma-h_2}{k\sigma+h_2}$ , Eq. (3.48)
$R_{b,A,B}$	normal resistors, $\Omega$
$R_{1,2,3}$	normal resistors, $\Omega$
$S_{kx}, S_{ky}$	Sensitivity to $k_x, k_y$
$t$	time, second
$T$	temperature, $K$
$\tilde{T}$	temperature in complex form, $K$
$T^+$	$=T^*Ql/k$ , normalized temperature
$\bar{T}$	average temperature, $K$
$\Delta T(2\omega)$	temperature variation in sample, $K$
$\Delta T_{IA}$	temperature result obtained from experimental data $U_{AB}^{3\omega}$ using IA model, $K$
$\Delta T_{HT}$	temperature result calculated from heat transfer model, $K$
$U_{AB}^{3\omega}$	the $3\omega$ party of the voltage difference between points A and B, $V$

$U_{A,B}$	voltage difference between point A and ground, $V$
$U_{CD}^\omega$	the supplying signal at frequency $\omega$ between points C and D, $V$
$V_f$	volume of fiber, $m^3$
$V_m$	volume of matrix, $m^3$
$V_p$	volume of porosity, $m^3$
$W$	$=l/a$
$W_0$	$=l_0/a_0$
$x, y$	major coordinate axes, $m$
$X_{a,b}$	impedance of the cable from point A to lock-in amplifier, $X_{a,b} = \frac{1}{i\omega C_{a,b}}$
$X_{A,B}$	combined impedance of $R_{a,b}$ and $X_{a,b}$ , $X_{A,B} = \frac{R_{a,b} X_{a,b}}{R_{a,b} + X_{a,b}}$
$x^+, y^+$	normalized coordinate axes, $x^+, y^+ = \frac{x, y}{l}$
X23	with the 2 <sup>nd</sup> and 3 <sup>rd</sup> kind of BC on sides $x=0$ and $x=c$ , respectively
Y23	with the 2 <sup>nd</sup> and 3 <sup>rd</sup> kind of BC on sides $y=0$ and $y=l$ , respectively

## Greek symbols

$\alpha$	thermal diffusivity, $m^2/s$
$\beta_m$	eigenvalues in y direction
$\beta_n$	eigenvalues in x direction
$\omega$	frequency $= 2\pi f$ , radiance/second
$\omega^+$	normalized frequency, $= \frac{\omega \alpha^2}{l}$ ,
$\tau$	dummy time variable, second

$\emptyset$	phase, <i>degree</i>
$\emptyset_{U_{AB}^{3\omega}}$	phase of measured signal $U_{AB}^{3\omega}$ , <i>degree</i>
$\sigma^2$	$= \frac{\beta_m^2}{l^2} + \frac{1}{\alpha} 2\omega i$
$\sigma^+$	$= \sigma l$

## Acronyms

AmpC	the circuit including two operational amplifiers and a multiplying DAC
AC	alternative current
BC	boundary condition
BriC	the electrical circuit that contains a Wheatstone bridge
C#X	carbon-fiber/epoxy composite sample marked with number X
C#XE#Y	experiment # Y on carbon-fiber/epoxy composite sample #X
DAC	data to analog converter
GF	Green function
NRM	Normal resistor measurement
DSP	digital signal processing
P#X	PMMA sample marked with number X
P#XE#Y	experiment # Y on PMMA sample #X
TPS	transient plane source

# Chapter 1 Introduction

## 1.1 Motivations

Composite materials, hereafter denoted composites, are engineered or naturally occurring materials made from two or more constituent materials with significantly different physical or chemical properties which remain separate and distinct at the macroscopic or microscopic scale within the finished structure. Most composites have strong, stiff fibers in a matrix which is weaker and less stiff. The objective is usually to make a component which is strong and stiff, often with a low density. Commercial materials commonly have glass or carbon fibers in matrices based on thermosetting polymers, such as epoxy or polyester resins. For the most part, they are still in a developmental stage, with problems of high manufacturing costs yet to be overcome.

The subject of this work is thermal properties of carbon-fiber/epoxy composites. Carbon fiber, alternatively graphite fiber or carbon graphite, is a material consisting of extremely thin fibers about 0.005–0.010 mm in diameter and composed mostly of carbon atoms. Figure 1.1(a) shows a single carbon filament with 6 micrometer diameter compared to a human hair. The carbon filaments can be twisted together to form carbon fiber yarns shown in Fig. 1.1(b). To make carbon fiber take on a permanent shape, these fibers are combined with epoxy resins to form composites as shown in Fig. 1.1(c). Carbon-fiber composites are commonly referred to by the name of their reinforcing fibers “carbon fiber”.

Carbon-fiber/epoxy composites are considered as replacements for metals in situations where excellent specific strength properties, e.g. strength/weight and or stiffness/weight

ratios are needed. They have gained popularity (despite their generally high cost) in high-performance products that need to be lightweight, yet strong enough to take harsh loading conditions such as aerospace components (tail, wing, fuselage, propeller), boat and scull hulls, bicycle frames and racing car bodies. For example, the Lockheed-Martin F-22 Raptor Raptor's airframe is made up of mostly carbon fiber composite panels and titanium. The new Boeing 787 Dreamliner contains approximately 23 tons of carbon fibers [4].

Although extensive research has been conducted on the mechanical properties of carbon-fiber composites, research on their thermal properties is relatively limited. A better understanding of carbon fiber composite material's thermal behavior will enable engineers to produce an optimum design for a structure. This project originated from a need for understanding the heat conduction behavior of carbon-fiber composite natural gas tanks during rapid filling. During the raid filling process, the temperature of the gas in the tank increases substantially. With the increasing usage of composites in commercial and military aircrafts, heat dissipation from aircraft systems is increasingly important, due to rapid increase in thermal load imposed on engine, which is expected to reach 10,000 kW [5]. For safe operation of such vehicles, using extensive carbon fiber composite work, the accumulated heat must be conducted away. Learning the thermal properties of the composite material is a key to understanding the related heat transfer behaviors.

Composites present high thermal anisotropy in along-fiber and perpendicular-to-fiber direction. Based on Hwan-Boh Shim et al [5], the thermal conductivity ratio between these two direction can be varied between 40~130. In practice, the in-plane direction of

fiber-composite often aligns with the along-fiber direction, and through-thickness-direction is often the perpendicular-to-fiber direction. In many applications, both in-plane heat spreading and through-thickness heat removal are important for effective heat dissipation. The thermal conduction behavior of an isotropic matrix reinforced with cylindrically orthotropic fibers is fully characterized by the values of its in-plane and through-thickness thermal conductivity [6].

A detailed literature review will be presented in Chapter 2. For a quick glance, there are mainly two different approaches researchers have been using to predict the thermal properties of composite material. They are based on the composite constituent component properties and the steady-state heat transfer measurements, respectively. Using the former approach, having an accurate knowledge about the component material properties is essential, however this information is often not available or difficult to obtain. As for the steady-state heat transfer measurement approach, quantifying the related heat amount is considerably challenging. In this work, a steady-periodic heating technique (named the  $3\omega$  method) is used to estimate the anisotropic thermal properties of carbon-fiber/epoxy composite material. The major feature of the steady periodic heating compared to steady state heating is the usage of the frequency dependence of temperature oscillations instead of time domain temperature responses. The steady periodic method has been widely used for studying the thermal properties of isotropic materials, but little previous work has been found for anisotropic materials.

To summarize, the objective of this work is to estimate the in-plane and through-thickness thermal conductivities of carbon-fiber/epoxy composites using a steady-periodic technique.

## 1.2 Dissertation outline

This dissertation includes both theoretical and experimental work. It is divided into six chapters. Chapter 1 is the introduction. Chapter 2 is the literature review on thermal property estimation of composite materials and the  $3\omega$  experimental techniques. Chapter 3 discusses the anisotropic theoretical heat transfer model along with its temperature solution. A careful sensitivity analysis is also included. Chapter 4 describes the experimental setup and reports experimental results. Chapter 5 presents the inverse parameter estimation results for thermal properties, which is a systematic comparison between experimental data and the theoretical temperature solution. Chapter 6 contains the summary and conclusions.



**Figure 1.1 Structure of carbon-fiber/epoxy composite a) A single carbon filament compared to a human hair [1]; b) raw carbon-fiber thread [2]; c) carbon-fiber/epoxy composite [3]**

# Chapter 2 Literature review

The thermal properties of composite materials have been a topic of interest for about a century. Section 2.1 is a review of two conventional approaches.

The three-omega ( $3\omega$ ) method was developed in the 1960's and systematically investigated mainly in the last twenty years, which made the technique practical. The  $3\omega$  method is generally used for estimating thermal properties of isotropic materials. Section 2.2 is a review of the previous researchers' work on using the  $3\omega$  method for thermal property estimation.

## 2.1 Thermal property estimation of composite materials

There are two different approaches which are often applied for estimating thermal properties of composite materials. One is based on constituent components, and the other is based on heat transfer measurements.

### 2.1.1 Based on constituent components

Since composites have more than one component, heat transfer in composites is governed by each component's thermal properties, their relative volume fractions, their geometrical arrangement and the weave style of fiber, etc. Prediction of thermal properties of composite materials based on the constituent material properties has been of interest for many years.

Regarding the in-plane thermal conductivity (in the along-fiber-axis direction), a simple rule of mixture is generally considered to be valid. Hasselman *et al.* [7], Dasgupta

*el al.* [8], Springer *et al.* [9], Thornburg [10], Harris *et al.* [11], pilling *et al.* [12] and Brennan *et al.* [13] reported the longitudinal thermal conductivity is calculated by the rule of mixtures:

$$k_c = k_f V_f + k_m V_m$$

where  $k$  is the thermal conductivity, the subscripts  $c, f$  and  $m$  refer to the composite, fiber and matrix, respectively. Whittaker *et al.* [14] and Mottram *et al.* [15] gave a more critical evaluation of the porosity distribution and calculated the in-plane thermal conductivity by:

$$k_c = k_f V_f + k_m (1 - V_f - V_p)$$

where  $V_p$  represents the volume of porosity.

Analysis of heat flow in through-thickness direction (transverse thermal conductivity, in the perpendicular-to-fiber-axis direction) presents a considerably more complex and less readily defined problem. A number of mathematical models have been developed to predict the through-thickness thermal conductivity of composite material. Springer *et al.* [9] studied the through-thickness thermal conductivity by means of an analogy between transverse heat transfer and longitudinal shear loading shown by Fig. 2.1. Hashin [16] extended the shear property approach to define upper and lower bounds for through-thickness thermal conductivity of transversely isotropic materials. Dasgupta *et al.* [8] and Thornburgh [10] formulated an expression of transverse thermal conductivity based on an analogy between thermal resistance and electrical resistance shown by Fig. 2.2. Nielsen [17] and Pilling *et al.* [12] treated transverse thermal conductivity of carbon fiber composite on an elasticity analogy approach. Mottram *et al.* [18] concluded that the generalized dispersion approach of Bruggerman [19] which took account of porosity was

the most appropriate one compared to Springer's [9] or Nielson's [7] expression. Hasselman *et al.* [7] modeled the transverse thermal conductivity of uniaxial composite with cylindrically orthotropic carbon fibers and interfacial thermal barrier. Ashton *et al.* [20] developed a model for transverse thermal conductivity using an analogy between in-plane field equations and boundary conditions to the transverse transport coefficient. Krach *et al.* [21] investigated the influence of void shape, void volume and matrix anisotropy on effective thermal conductivity of a three-phase composite. Zou *et al.* [22] derived an analytical solution for transverse thermal conductivities of unidirectional fibrous composites with thermal barrier based on the thermal-electrical analogy technique and on the cylindrical filament-square packing array unit cell model. Pichumani and Yao [23, 24] presented a fractal model for transverse thermal conductivities of unidirectional fiber composites with perfect contact between fiber filament and matrix.

### **2.1.2 Based on heat transfer measurement**

Another approach investigated by many scientists [25-35] for estimating thermal conductivities of composites is based on heat transfer measurement. Some scientists measured the thermal conductivities by means of steady-state method. That is to generate a one-dimensional temperature gradient in a laminate surrounded by an environment designed to eliminate heat flow in directions other than the one to be measured. Behzad *et al.* [25] studied the thermal conductivity of hemp fiber reinforced polymer composites from the steady state temperature drop across samples exposed to a known heat flux. Fig. 2.3(a) shows the apparatus of Behzad, which consists of an electrically heated Kapton thin film as the heat source sandwiched between two similar brick-shaped specimen halves. A homogeneous rate of heat flow is fed into the heater and temperature gradient

on a sample is monitored by two thermocouples placed on both sides of the sample. For transverse and in-plane measurements heat is fed into the sample from different direction as shown in Fig. 2.3(b). The thermal conductivity is then calculated using Fourier's law. Han *et al.* [26], Shim *et al.* [27] and Garnier *et al.* [28] also investigated the thermal conductivities of fiber-reinforced composites using the steady-state hot plate method and Fourier's law. Sweeting *et al.* [29] developed an experimental method on steady-state heating to determine the in-plane and though-thickness thermal conductivities of polymer matrix composites based on steady-state method as shown in Figure 2.4. The temperature gradient in the given direction is recorded using thermocouples and the result is processed numerically by an inverse approach to determine the directional thermal conductivity.

A few researchers used transient plane source (TPS) technique to measure the thermal properties of composite materials. Kalaprasad *et al.* [30] analyzed and presented the thermal conductivity and thermal diffusivity of sisal-reinforced polyethylene, glass-reinforced polyethylene and sisal/glass hybrid fiber reinforced polyethylene composites by the means of TPS method. The TPS technique is based on the three-dimensional heat flow inside a sample which can be regarded as an infinite medium by limiting the total time of transient recording. A disk-shaped TPS sensor shown in Figure 2.5(a) was placed between two cylindrical pieces of the sample. Figure 2.5(b) shows the conduction models corresponding to the in-plane and through-thickness thermal conductivity measurement, respectively. Many scientists have [31-35] also worked on using TPS technique for estimating the thermal properties of composite materials.

The major hurdle of using heat transfer measurement method to determine thermal properties is that an accurate measurement of the quantity of heat flow is often the key for a good estimation. However quantifying the exact amount of heat flux is very challenging with current technology. In practice, the heat flux amount is often calculated based on the characteristic of the heater. A well-engineered experimental setup is usually needed to reduce the heat loss by conduction, convection or radiation. In this work, a steady-periodic heat transfer measurement approach is adopted. It uses the frequency dependence of temperature oscillation instead of the time domain temperature responses, which is inherently insensitive to heat loss.

### **2.1.3 Comparison of the two approaches**

Comparing these two approaches for estimating the thermal properties of composite materials based on constituent material properties and based on heat transfer measurements, the former one has some disadvantages. First, having an accurate knowledge about the properties of each component of the composite is essential for using the constituent-component approach which could be very difficult or impossible since the properties of a large variety of different kinds of fiber and/or epoxy differ greatly. Secondly, the volume fraction of each component and their relative geometric distribution are also necessary using the first approach, which is often impossible to have access to that information. Moreover, with the constituent-component approach the arrangement of fibers has to be assumed in ordered arrays described by a repeating unit which could be far from the actual arrangement in the composite. This reduces the accuracy of the approach based on constituent component properties.

The approach of heat transfer measurements overcomes all the disadvantages of the first approach discussed above. The experimental method in this work is based on heat transfer measurement. However the measurement in this work is based on steady-periodic heating technique, instead of the steady-state method discussed in the previous section.

## 2.2 The $3\omega$ method

The thermal conductivity of solids is usually determined by measuring the temperature gradient produced by a steady flow of heat in a one-dimensional geometry as discussed in the last section. The technique adopted in this work, which is referred as the  $3\omega$  method, is an alternating current (ac) technique closely related hot-wire [36-40] and hot-strip [41-43] techniques for measuring thermal properties. In these techniques a single element is used simultaneously as heater and thermometer. In the hot wire method a heating wire is enclosed in the investigated materials and can be used as a resistance thermometer for instantaneous temperature measurement. The technique has been routinely applied for the determination of liquids and solids. In the hot strip method, a wide rectangular metal film is evaporated onto the surface of the sample. In both the hot-wire and hot-strip techniques, the data analysis is performed in the time domain. The major difference between these two techniques and the  $3\omega$  method is the use of the frequency dependence of temperature oscillations instead of the time-domain response.

In a  $3\omega$  measurement, a thin and narrow metal film is deposited on the surface of the sample with good thermal contact to the sample, serving as both heater and thermometer simultaneously. An alternating current at frequency  $\omega$  passes through the metal film generating heat flux oscillation at frequency  $2\omega$  due to Joule heating. Because of the

thermoreistance effect, the electrical resistance of the wire oscillates with the surface temperature of the sample at the same frequency  $2\omega$ . Thus, the resulting voltage drop across the heating at wire at frequency  $3\omega$  contains the thermal properties information of the sample. Therefore, the direct objective of the measurement is to detect the fairly faint  $3\omega$  signal.

The  $3\omega$  method has several characteristics that make it an attractive alternative for thermal conductivity measurements on a wide range of materials and structures. The periodic nature of  $3\omega$  method is inherently insensitive to radiative and convective heat losses, depending on the test section geometry. Second, a properly chosen frequency input and range can eliminate problematic boundary conditions that may exist between the sample and external test hardware. Finally, since the  $3\omega$  method is a nondestructive technique, certain device geometries and material systems used in the high-powered microelectronic device systems of interest can be examined in their in situ conditions or with minimal post processing.

### **2.2.1 The $3\omega$ method on isotropic materials**

The  $3\omega$  method originated with Corbino [44-45], who first noticed that a very small third-harmonic voltage component appears while applying an alternating current (ac) through a resistive heater. Later on, Rosenthal [46] used the bridge technique to measure the third harmonic signal. The  $3\omega$  method was used to measure the specific heat of the heater by Rosenthal [46] and Holland [47]. The method was further developed to measure the specific heat of substrate materials [48-50] using frequency domain studies [48-53] in the research field of supercooled liquids in the 1980's. Birge and Nagel [49] developed an experimental technique for studying the frequency dependent thermal response of

supercooled liquids, where a thin nickel film was evaporated onto a glass substrate and in contact with the liquid whose properties they are studying (See Fig. 2.6). Fig. 2.6 (b)-(c) shows the schematic experimental setup of Birge's including a frequency tripler. Later this setup was adopted and developed by many scientists. Oxtoby [54] analyzed Birge and Nagel's experiments and showed the relation between the frequency and wave vector dependent thermal conductivity and their frequency dependent specific heat. Dixon [52] indicated that the quantity measured with specific-heat spectroscopy is the frequency-dependent product of the specific heat and thermal conductivity and expanded the technique to decouple the dynamics in the two properties to measure them separately. Using the  $3\omega$  method to measure thermal conductivity of bulk material was documented in detail by Cahill *et al.* [55-58]. With the emergence of a turn-key Lock-in amplifier, a simplified experimental setup relative to Birge and Cahill's were used by Hou *et al.* [59] (See Fig. 2.7), Wang *et al.* [60] (See Fig. 2.8) and Hopkins *et al.* [61] etc. For example, the use of a SR830 digital signal processing lock-in amplifier with higher harmonic detection removes the need for a frequency tripling circuit. In this work, Hou's circuit [59] was adopted.

The thermal properties of a variety of specimens have been investigated using the  $3\omega$  method. The method was introduced to measure the thermal conductivity of isotropic bulk materials exhibiting low thermal conductivity values [55-58, 62-63]. It has since been applied to determine the thermal conductivities of thin film materials ranging from nanometers to micrometers in thickness [57, 64-79], superlattice structures [80-83], nanowires [84-86], and liquids [83, 87-92].

Solving the heater-on-substrate problem in theory is an important part of the  $3\omega$  method. Cahill *et al.* [55-58] made a seminal contribution by obtaining an analytical solution for a vanishingly thin but finite-width heater. They began with the exact solution for the amplitude of the temperature oscillations a distance from a line source of heat, and then integrated the temperature across the heater width to get the average temperature amplitude. A few authors [61-67, 70, 83, 90, 91] have extended this approach to thermal property measurement over certain frequency range by integrating solution for a finite-width heater.

One-dimensional models [55-92], two-dimensional models [93-97] and three-dimensional models [98] had been proposed to analyze the  $3\omega$  component to the thermal conductivity of homogeneous and isotropic materials. Cole [94] solved the two-dimensional conduction problem for  $3\omega$  method with an imposed heat flux using a Green's function. Borca-Tasciuc *et al.* [68] derived a general solution for the two-dimensional heat conduction across a multilayer system. Wang *et al.* [95] established a two-dimensional heat conduction model for the heater-on-substrate  $3\omega$  method which takes into account the finite thickness of the heater. Analytical solutions for the finite-heater problem and the vanishing heater-thickness problem are presented utilizing the method of separation of variables. Battaglia *et al.* [98] achieved an analytical solution of the 3D heat diffusion problem, in the  $3\omega$  experimental technique configurations, using integral transforms. It leads to rapid calculation of the average temperature on the heated area without any numerical problems even if the heater is very narrow.

### 2.2.2 The $3\omega$ method on anisotropic materials

The  $3\omega$  method has been adapted recently for characterization of samples with anisotropic thermal properties. Yang et al. [82] employed a two-wire  $3\omega$  method to measure the in-plane and cross-plane thermal conductivities of superlattices. The cross-plane Seebeck coefficient is deduced by using a differential measurement between the superlattice and reference samples and the cross-plane electrical conductivity is determined through a modified transmission-line method. Tsui et al. [99] used the  $3\omega$  measurement system and a proposed serial-parallel hybrid model to estimate the in-plane and cross-plane thermal conductivities of nanoporous silica film. Borca et al. [68] derived an exact solution of the complex average temperature rise for a heater deposited on a thin layer as a function of thermal conductivity anisotropy (the ratio of in-plane to cross-plane thermal conductivity) based on a two-dimensional heat conduction model. Abramason et al. [100] used the data from the  $3\omega$  measurement and the model of Borca [68] to estimate the effective thermal conductivity (square root of the production of in-plane and cross-plane thermal conductivity) of nanocomposite material, and the specific in-plane and cross-plane thermal conductivity were estimated under the assumption that nanowire filling factor within the composite is known. Borca et al. [101] reported the temperature-dependent, anisotropic thermal conductivity and thermal diffusivity of nanochanneled alumina templates. The  $3\omega$  technique was employed to carry out measurements of the effective thermal conductivity and thermal diffusivity in the direction parallel to the nanochannel axis, while thermal anisotropy of the sample was considered known and calculated.

In the  $3\omega$  measurement system, the lock-in amplifier gives both phase and amplitude information of temperature oscillation. Most researches used the amplitude information only to extract the thermal properties. Few [59, 101] used both phase and amplitude information to study a homogeneous material. In contrast, this paper describes the application of a steady-periodic technique for determining the anisotropic thermal properties of a fiber-wound composite, which has not been treated by  $3\omega$  method yet. The unique aspects of the work include 1) the detailed two-dimensional anisotropic heat transfer model for simultaneous fitting of in-plane and through-thickness thermal conductivities; 2) calibrating cable impedance in the experiment; 3) apply the  $3\omega$  method to fiber composite materials. This model also supports a careful sensitivity study which showed that the multiple unknown parameter estimation was achievable and indicated the important frequency range for getting useful data in the experiment. The Green's function approach is used to obtain the analytical temperature solution. Both amplitude and phase information from the  $3\omega$  experiment are compared with the analytical solution. The thermal conductivity parameters are varied until best-match between measured and calculated temperature distributions are obtained, thereby determining the anisotropic conductivity parameters. PMMA samples were used as reference samples to verify our approach. Both in-plane thermal and through-thickness thermal conductivity parameters of carbon-fiber composite samples were then obtained from our approach, and which are reported in this work.

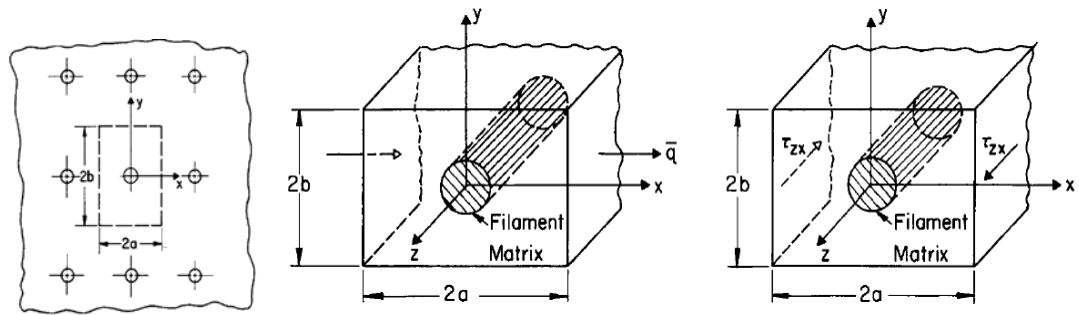


**Figure 2.1 Fundamental element used in the analogy between transverse heat transfer and longitudinal shear loading by Springer *et al.* [3]**

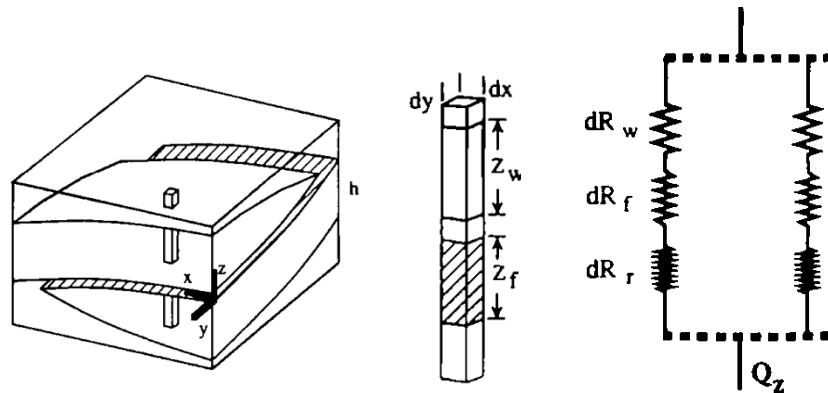


**Figure 2.2 Fundamental element used in the analogy between transverse thermal resistance and electrical resistance by Dasgupta *et al.* [2]**

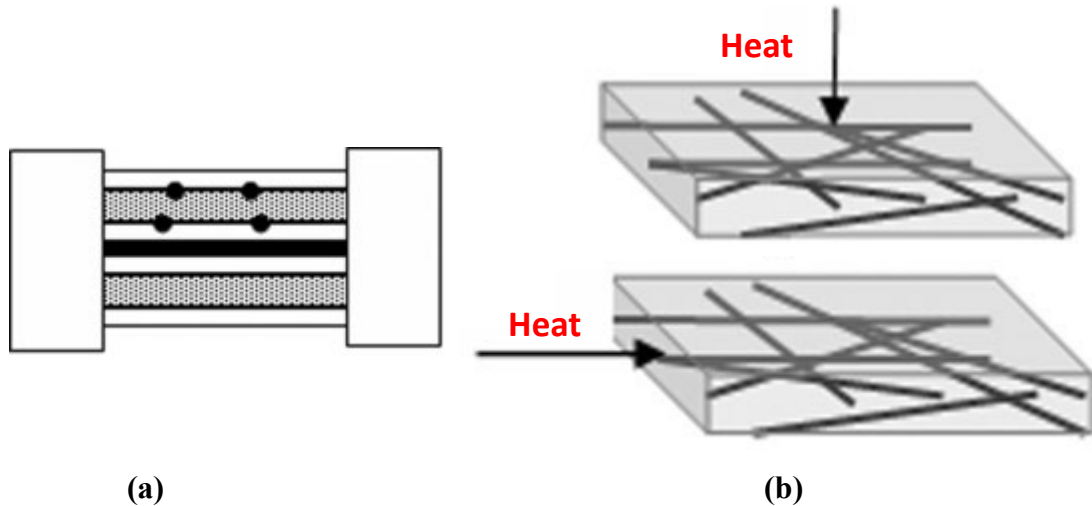


**Figure 2.3 Schematic of Behhzad *et al.*'s experimental set-up [19]** (a) The apparatus used by Behzad; (b) Transverse and in-plane Measurement

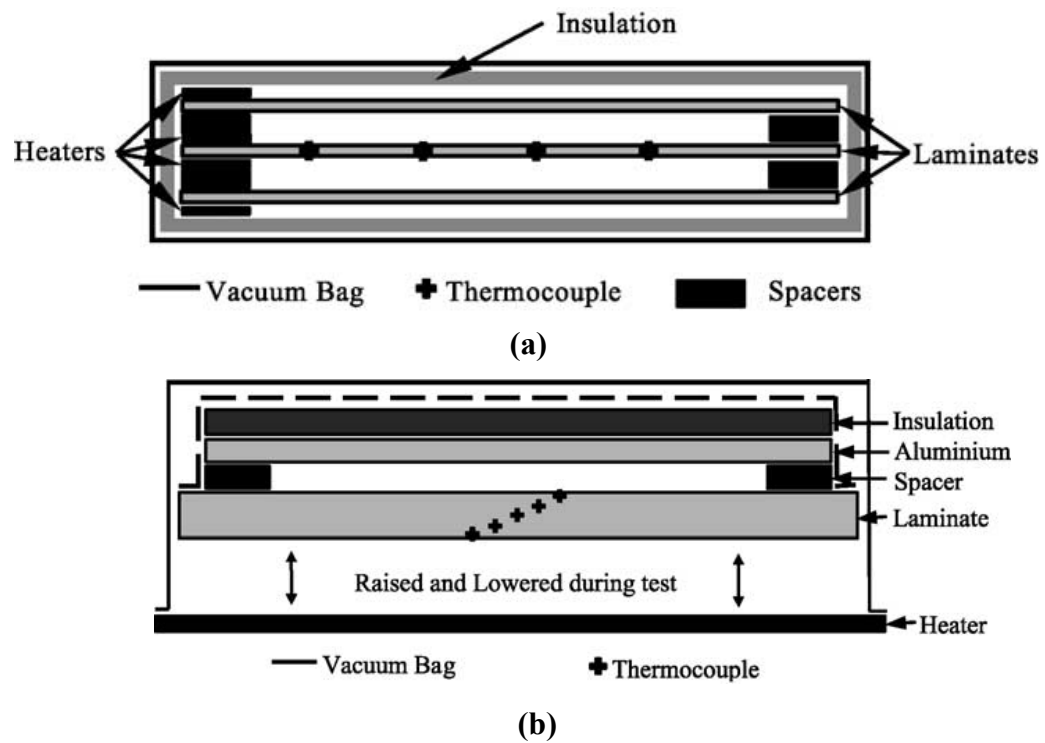


**Figure 2.4 Schematic of Sweeting *et al.*'s experimental set-up [23]** (a) Schematic of in-plane conductivity set-up; (b) Schematic of through-thickness conductivity set-up

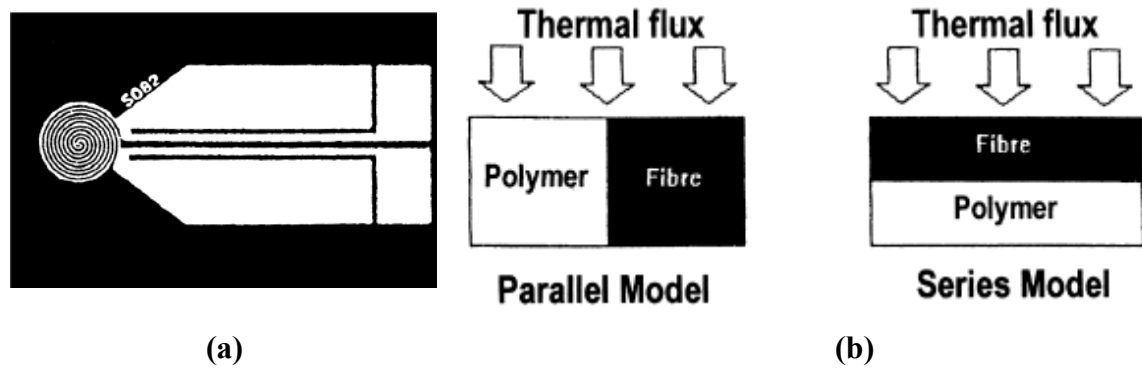


**Figure 2.5** The hot disk sensor and the conduction model used by Kalaprasad *et al.*[24] (a) Sketch of hot disk sensor; (b) the conduction models corresponding in-plane and transverse thermal conductivity measurement, respectively.

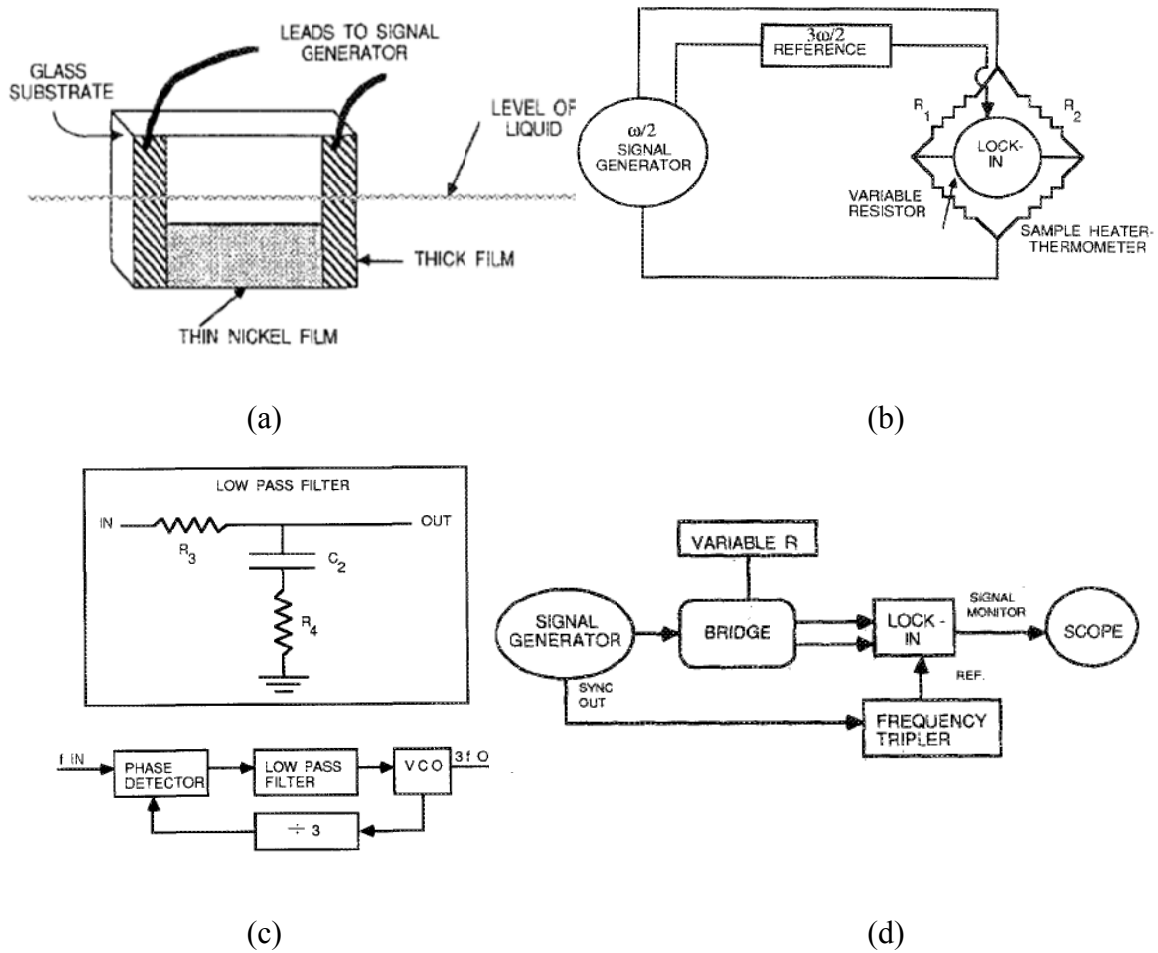


**Figure 2.6 Schematic of Birge *et al*'s experimental setup [43 ](a) schematic diagram of sample heater/thermometer. Heater is a thin nickel film evaporated onto a thick substrate; (b) schematic diagram of experimental setup; (c) block diagram of frequency tripler circuit; (d) block diagram of manual control**

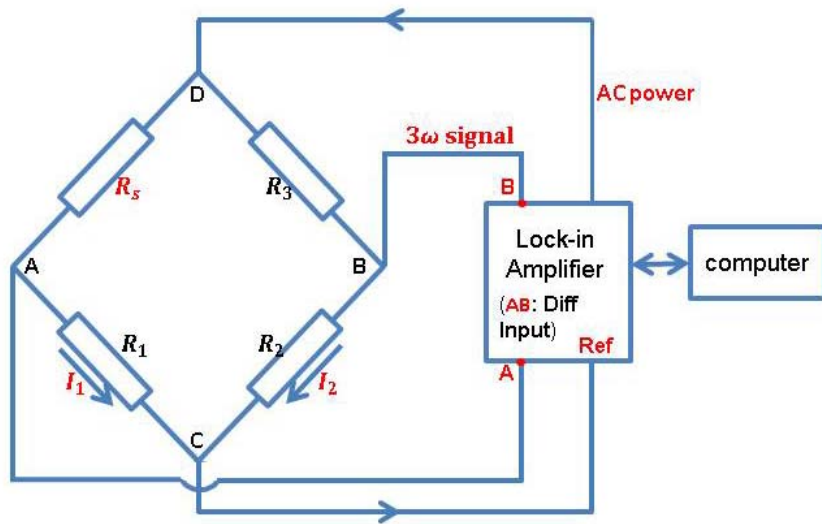


**Figure 2. 7 Schematic of Hou *et al*'s experimental setup [53]**

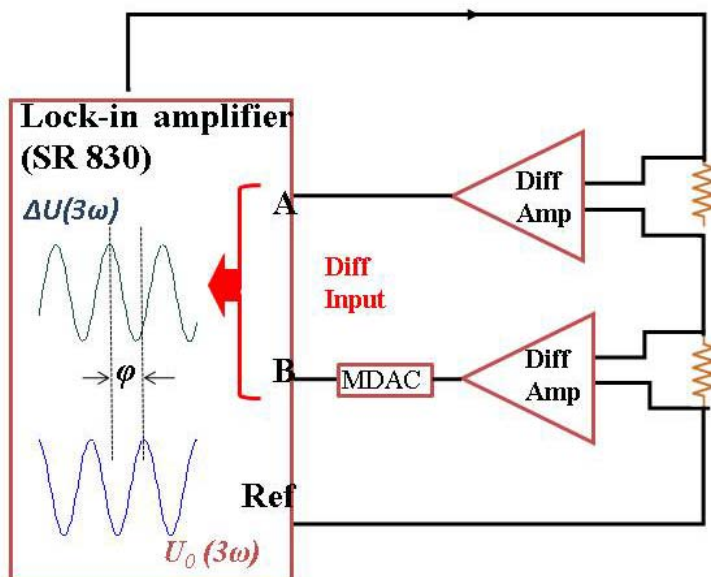


**Figure 2. 8 Schematic of Wang *et al*'s experimental setup [54]**

# Chapter 3

## Forward model development

This chapter is devoted to the derivation of the analytical temperature solution from the anisotropic forward heat transfer model. A careful sensitivity analysis is included, which is an important part of any successful simultaneous estimation of multiple parameters. The temperature solution will be used to curve-fit the experimental data in the subsequent chapters.

### 3.1 Anisotropic heat transfer model

#### 3.1.1 Assumptions

The sample geometry with size  $2c_0 \times 2c_0 \times 2l_0$  is shown in Fig. 3.1. A platinum film with width  $a$  is deposited on one surface of the sample as shown in Fig. 3.1(b). Fig. 3.1 (c) shows the directions of heat flow along the film on the  $x$ - $z$  plane as an electrical current goes through it. Since the platinum length  $z=15$  mm is much larger than its width  $a_0=0.1$  mm, heat flows mainly in the perpendicular-to-length direction ( $x$ -coordinate direction) in the area around the heater, and heat flows in the  $z$  directions only at the ends of the heater. Considering the end of heater to be a ball with diameter  $a_0=0.1$  mm, it can be assumed that heat only flows in the  $x$  direction along about  $\frac{15-2\times0.1}{15} = 98.7\%$  of heater length.

Thus, heating in  $z$ -coordinate direction may be neglected and heat transfer is presumed to occur only in  $x$ - $y$  plane. Therefore, a two-dimensional heat transfer model is developed.

The assumptions for the heat transfer model built in this work are:

1. The heat transfer is two-dimensional as discussed in the previous geometry paragraph.
2. The thermal conductivity is orthotropic, and depends on direction.
3. The thickness of platinum film is neglected. This thickness is approximately 50 nanometers, which is obtained from an X-ray reflectivity experiment (See Section 4.2 for detail).
4. There is perfect thermal contact between the platinum film and the sample.
5. Heat loss by radiation is neglected.
6. Density and heat capacity of the sample are homogeneous.
7. The temperature change caused by heating is small, therefore thermal properties are fixed.

### **3.1.2 Anisotropic heat transfer equations**

Consider the temperature response of the sample in a two-dimensional domain in rectangular coordinates (see Fig. 3.1(c)), the coordinate directions  $x$  and  $y$  are corresponding to the in-plane and through-thickness direction in the sample, respectively. A sinusoidal input current with frequency  $\omega$  generated by an internal oscillator built in the lock-in amplifier passes through the platinum film and causes heating  $q = Q_0 \cos^2(\omega t)$  due to Joule heating, which creates a temperature fluctuation in the sample

at frequency  $2\omega$ . On the other three sides of the sample, the third kind of boundary conditions is applied. With the assumptions described in the last section the periodic temperature distribution in the sample  $T(x, y, t)$  satisfies the following equations:

$$k_x \frac{\partial^2 T}{\partial x^2} + k_y \frac{\partial^2 T}{\partial y^2} = \rho c \frac{\partial T}{\partial t} \quad (3.1)$$

$$-k_x \frac{\partial T}{\partial x} \Big|_{x=0} = 0 \quad (3.2)$$

$$-k_x \frac{\partial T}{\partial x} \Big|_{x=c_0} = -h_{30} T \Big|_{x=c_0} \quad (3.3)$$

$$-k_y \frac{\partial T}{\partial y} \Big|_{y=0, 0 < x < a/2} = Q_0 \cos^2(\omega t) \quad (3.4)$$

$$-k_y \frac{\partial T}{\partial y} \Big|_{y=l_0} = -h_{20} T \Big|_{y=l_0} \quad (3.5)$$

where  $k_x$  and  $k_y$  are the thermal conductivities in coordinate direction  $x$  and  $y$  respectively. We call them in-plane and through-thickness thermal conductivities respectively. Symbol  $h_{20}$  and  $h_{30}$  represent the heat transfer coefficient on the  $x = \pm c_0$  and  $y = l_0$  sides.

### 3.1.3 Converting the anisotropic model to isotropic

Next, the heat transfer equations for the orthotropic solid as given above will be transformed into a standard form based on a coordination-scaling method [102, page 631-632].

We consider equations (3.1)-(3.5) and define new variables  $x'$ ,  $y'$ , as

$$x' = \left(\frac{k}{k_x}\right)^{1/2} x, \quad y' = \left(\frac{k}{k_y}\right)^{1/2} y \quad (3.6)$$

where  $k$  is a reference conductivity.

Then the anisotropic heat transfer model consisting of Eqs. (3.1)-(3.5) under coordinates  $x$  and  $y$  is transformed to a new one under coordinates  $x'$  and  $y'$  consisting of equations (3.7)-(3.11):

$$k\left(\frac{\partial^2 T}{\partial x'^2} + \frac{\partial^2 T}{\partial y'^2}\right) = \rho c \frac{\partial T}{\partial t} \quad (3.7)$$

$$-k \frac{\partial T}{\partial x'}|_{x'=0} = 0 \quad (3.8)$$

$$-k \frac{\partial T}{\partial x'}|_{x'=c} = -h'_3 T|_{x'=c} \quad (3.9)$$

$$-k \frac{\partial T}{\partial y'}|_{y'=0,0 < x' < a'/2} = Q \cos^2(\omega t) \quad (3.10)$$

$$-k \frac{\partial T}{\partial y'}|_{y'=l} = -h'_2 T|_{y'=l} \quad (3.11)$$

The new model relates to an isotropic parameter  $k$  instead of anisotropic parameters  $k_x$  and  $k_y$ . The reference conductivity  $k$  can be determined by energy conservation law. A volume element in the original space  $dxdy$  transforms, under the transformation Eq. (3.6), into

$$dxdy = \frac{(k_x k_y)^{0.5}}{k} dx'dy'$$

If the quantity  $\rho C_p$  defined on the basis of unit volume, has the same physical significance we should have:

$$\frac{(k_x k_y)^{0.5}}{k} = 1$$

Therefore we get

$$k = (k_x k_y)^{0.5} \quad (3.12)$$

$$\text{Here } x' = x \left( \frac{k}{k_x} \right)^{0.5}, y' = y \left( \frac{k}{k_y} \right)^{0.5}, a = a_0 \left( \frac{k_y}{k_x} \right)^{0.25}, c = c_0 \left( \frac{k_y}{k_x} \right)^{0.25}, h_2 = h_{20} \left( \frac{k_x}{k_y} \right)^{0.25}, \\ l = l_0 \left( \frac{k_x}{k_y} \right)^{0.25}, Q = Q_0 \left( \frac{k_x}{k_y} \right)^{0.25}, h_3 = h_{30} \left( \frac{k_y}{k_x} \right)^{0.25} \quad (3.13)$$

Hence, the original anisotropic model consisting of equations (3.1)-(3.5) under coordinates  $x$  and  $y$  is converted to be an isotropic model described by equations (3.7)-(3.11) under new coordinates  $x'$  and  $y'$ . The next section is devoted to derive the analytical temperature solution of this scaled isotropic heat transfer model.

## 3.2 Analytical temperature solution

### 3.2.1 Introduction

In this work, the scaled isotropic heat transfer model is solved with the method of Green's Functions (GFs). This approach provides a comprehensive set of tabulated GFs. By utilizing these tabulated GFs, solutions of the heat conduction problems in this work can be obtained in a straightforward and efficient manner. Two-dimensional GFs can be found by simple multiplication of one-dimensional GFs for the rectangular coordinate system. A detailed description of the Green's function solution for classical thermal conduction applications is given by Cole *et al* [103].

For writing convenience, the scaled coordinates  $x'$  and  $y'$  in equations (3.7)-(3.11) are replaced with  $x$  and  $y$  from this point and those equations are rewritten as equations (4.1-4.5). Note that besides coordinates  $x$  and  $y$ , parameters  $k$ ,  $Q$ ,  $l$ ,  $a$ ,  $c$ ,  $h_2$  and  $h_3$  are all scaled according to Eq. (3.13) as well.

$$k\left(\frac{\partial^2 T}{\partial x^2} + \frac{\partial^2 T}{\partial y^2}\right) = \rho c_p \frac{\partial T}{\partial t} \quad (3.14)$$

$$-k \frac{\partial T}{\partial x} |_{x=0} = 0 \quad (3.15)$$

$$-k \frac{\partial T}{\partial x} |_{x=c} = -h_3 T |_{x=c} \quad (3.16)$$

$$-k \frac{\partial T}{\partial y} |_{y=0, 0 < x < a/2} = Q \cos^2(\omega t) \quad (3.17)$$

$$-k \frac{\partial T}{\partial y} |_{y=l} = -h_3 T |_{y=l} \quad (3.18)$$

In this work, the application is limited to steady-periodic heating, since heating is simply periodic and a phase-lock amplifier is used in the experiments to select the response at the periodic frequency. Steady-periodic heat conduction, of interest for thermal property measurements, may be treated analytically either by time-domain or frequency-domain GFs. Analytical solutions from both approaches are derived in this chapter to verify the accuracy of the solution obtained. Section 3.2.2 gives the fundamental temperature solution using time domain GFs. Section 3.2.3 improves the convergence speed of this solution. Section 3.2.4 presents the analytical temperature solution based on frequency domain GFs. Section 3.2.5 gives a comparison among the three different analytical solutions obtained in the previous sections. Section 3.2.6 describes the average temperature on the heater.

### 3.2.2 Temperature solution in time domain

The solution of this problem can be readily written out in the form of GFs. The two-dimensional GFs are the product of the one-dimensional GFs based on the multiplicative property of the method of GFs. The temperature solution is given by the following integral equation [103, page 212-217]:

$$T(x, y, t) = \frac{\alpha}{k} \int_{\tau=0}^t q \int_{x'=0}^{x'=\frac{a}{2}} G_{X23}(x, t|x', \tau) G_{Y23}(y, t|y' = 0, \tau) dx' d\tau \quad (3.19)$$

where

$$q = Q \cos^2(\omega\tau) \quad (3.20)$$

and  $\tau$  is the dummy time variable used in convolution integrals. The subscripts under the GF, symbol G, denote the direction and the types of boundary conditions. Specifically, the notation  $G_{X23}$  is the GF in the  $x$  direction with boundary conditions of the second kind at  $x = 0$  and the third kind (specified convection) at  $x = c$ . The  $G_{Y23}$  symbol is for the second type of boundary condition at  $y = 0$  and specified convection at  $y = l$ .

At this point, the long cotime ( $u = t - \tau$ ) form of the one dimensional GFs [103, page 600] are used. They are

$$G_{X23}(x, t|x', \tau) = \frac{2}{c} \sum_{n=1}^{\infty} \frac{\beta_n^2 + B_3^2}{\beta_n^2 + B_3^2 + B_3} \exp\left(-\frac{\beta_n^2 \alpha(t - \tau)}{c^2}\right) \cos \frac{\beta_n x}{c} \cos \frac{\beta_n x'}{c} \quad (3.21)$$

$$G_{Y23}(y, t|y', \tau) = \frac{2}{l} \sum_{m=1}^{\infty} \frac{\beta_m^2 + B_2^2}{\beta_m^2 + B_2^2 + B_2} \exp\left(-\frac{\beta_m^2 \alpha(t - \tau)}{l^2}\right) \cos \frac{\beta_m y}{l} \cos \frac{\beta_m y'}{l} \quad (3.22)$$

Eigenvalues in Eqs. (3.21)-(3.22) are given by

$$\beta_n \tan \beta_n = B_3, B_3 \equiv \frac{h_3 c}{k}, \beta_m \tan \beta_m = B_2, B_2 \equiv \frac{h_2 l}{k} \quad (3.23)$$

Substituting Eqs. (3.21) and 3.22) into (3.19) and carrying out integration on  $x'$ , we have

$$T(x, y, t) = \frac{2Q\alpha}{kl} \int_{\tau=0}^t [1 + \cos(2\omega\tau)] \sum_{m=1}^{\infty} \frac{\beta_m^2 + B_2^2}{\beta_m^2 + B_2^2 + B_2} \exp\left(-\frac{\beta_m^2 \alpha(t - \tau)}{l^2}\right) *$$

$$\sum_{n=1}^{\infty} \frac{\beta_n^2 + B_3^2}{\beta_n^2 + B_3^2 + B_3} \exp\left(-\frac{\beta_n^2 \alpha(t-\tau)}{c^2}\right) \frac{\sin\left(\frac{\beta_n a}{2c}\right) \cos\frac{\beta_n x}{c}}{\beta_n}$$

(3.24)

Note: integration over the heated surface has already been calculated as

$$\int_{x'=0}^{x'=\frac{a}{2}} \cos\frac{\beta_n x'}{c} dx' = \frac{c}{\beta_n} \sin\left(\frac{\beta_n a}{2c}\right)$$

(3.25)

Note the formula  $\cos^2(2\omega\tau) = \frac{1}{2}[1 + \cos(2\omega\tau)]$  is used.

This temperature solution contains a double series that can be considered in two parts:  
a steady part caused by constant heating  $q_1 = \frac{Q}{2}$ ; and a steady-periodic part caused by  
heating  $q_2 = \frac{Q\cos(2\omega t)}{2}$ . Since in this study the applications are limited to steady-periodic  
heating, the resultant steady-periodic temperature from heating  $q_2 = Q\cos(2\omega t)/2$  is of  
interest. The temperature response under consideration will be:

$$T(x, y, t) = \frac{2Q\alpha}{kl} \int_{\tau=0}^t [\cos(2\omega\tau)] \sum_{m=1}^{\infty} \frac{\beta_m^2 + B_2^2}{\beta_m^2 + B_2^2 + B_2} \exp\left(-\frac{\beta_m^2 \alpha(t-\tau)}{l^2}\right) \cos\frac{\beta_m y}{l} *$$

$$\sum_{n=1}^{\infty} \frac{\beta_n^2 + B_3^2}{\beta_n^2 + B_3^2 + B_3} \exp\left(-\frac{\beta_n^2 \alpha(t-\tau)}{c^2}\right) \frac{\sin\left(\frac{\beta_n a}{2c}\right) \cos\frac{\beta_n x}{c}}{\beta_n} d\tau$$

(3.26)

And thereby, the resultant temperature  $T(x, y, t)$  could be written as the real part of  
an complex form  $\tilde{T}(x, y, t)$  by replacing  $\cos(2\omega\tau)$  in Eq. (3.26) with  $e^{i2\omega\tau}$ , then Eq.  
(3.26) becomes:

$$\begin{aligned} \tilde{T}(x, y, t) = & \frac{4Q\alpha}{kl} \sum_{m=1}^{\infty} \frac{\beta_m^2 + B_2^2}{\beta_m^2 + B_2^2 + B_2} \cos \frac{\beta_m y}{l} \sum_{n=1}^{\infty} \frac{\beta_n^2 + B_3^2}{\beta_n^2 + B_3^2 + B_3} \frac{\sin \left( \frac{\beta_n a}{2c} \right) \cos \frac{\beta_n x}{c}}{\beta_n} * \\ & \int_{\tau=0}^t e^{i2\omega\tau} \exp \left[ - \left( \frac{\beta_m^2}{l^2} + \frac{\beta_n^2}{c^2} \right) \alpha(t-\tau) \right] d\tau \end{aligned} \quad (3.27)$$

$$\text{Let } P = \alpha \left( \frac{\beta_m^2}{l^2} + \frac{\beta_n^2}{c^2} \right) \quad (3.28)$$

Evaluating the time integral, Eq. (3.27) becomes:

$$\begin{aligned} \tilde{T}(x, y, t) = & \frac{4Q\alpha}{kl} \sum_{m=1}^{\infty} \frac{\beta_m^2 + B_2^2}{\beta_m^2 + B_2^2 + B_2} \cos \frac{\beta_m y}{l} \sum_{n=1}^{\infty} \frac{\beta_n^2 + B_3^2}{\beta_n^2 + B_3^2 + B_3} \frac{e^{i2\omega\tau} - e^{-Pt}}{i2\omega + P} * \\ & \frac{\sin \left( \frac{\beta_n a}{2c} \right) \cos \frac{\beta_n x}{c}}{\beta_n} \end{aligned} \quad (3.29)$$

Take the real part of Eq. (3.29), we get

$$\begin{aligned} T(x, y, t) = & \frac{4Q\alpha}{kl} \sum_{m=1}^{\infty} \frac{\beta_m^2 + B_2^2}{\beta_m^2 + B_2^2 + B_2} \cos \frac{\beta_m y}{l} \sum_{n=1}^{\infty} \frac{\beta_n^2 + B_3^2}{\beta_n^2 + B_3^2 + B_3} * \\ & \frac{P \cos(2\omega t) + 2\omega \sin(2\omega t) - Pe^{-Pt} \sin \left( \frac{\beta_n a}{2c} \right) \cos \frac{\beta_n x}{c}}{4\omega^2 + P^2} \frac{1}{\beta_n} \end{aligned} \quad (3.30)$$

Normalize the temperature result  $\frac{T^+}{T} = \frac{Ql}{k}$

$$T^+(x, y^+, t) = \frac{4\alpha}{l^2} \sum_{m=1}^{\infty} \frac{\beta_m^2 + B_2^2}{\beta_m^2 + B_2^2 + B_2} \cos \frac{\beta_m x}{l} \sum_{n=1}^{\infty} \frac{\beta_n^2 + B_3^2}{\beta_n^2 + B_3^2 + B_3} *$$

$$\left[ \frac{P\cos(2\omega t) + 2\omega\sin(2\omega t) - Pe^{-Pt}}{4\omega^2 + P^2} \right] \frac{\sin\left(\frac{\beta_n a}{2c}\right) \cos\frac{\beta_n y}{c}}{\beta_n} \quad (3.31)$$

This is the time-domain solution for the steady-periodic temperature. This solution converges slowly, which could be attributed to two factors. First, this solution has a double summation. Second, the solution contains a series that should be considered in two parts: a transient part with an exponential factor  $\exp(-Pt)$ ; and, a steady-periodic part with no exponential factor. The transient part contains an exponential factor  $\exp(-Pt)$  where  $P = \alpha \left( \frac{\beta_m^2}{l^2} + \frac{\beta_n^2}{c^2} \right)$ , which promotes rapid series convergence and defines the rate of decay of the transient. The steady-periodic part of the series converges slowly. Evaluating all the terms of the series for accurate numerical values requires very long computer-evaluation times. In the next section, an alternative solution with much faster numerical converging is sought.

### 3.2.3. Improvement of series convergence

In this section, the part of the temperature solution that depends on coordinate x will be carefully converted to a better-converging form. We will start by going back to an earlier step in the derivation of temperature.

Rewriting Eq. (3.27) as

$$\begin{aligned}
\tilde{T}(x, y, t) = & \sum_{m=1}^{\infty} \frac{\beta_m^2 + B_2^2}{\beta_m^2 + B_2^2 + B_2} \cos \frac{\beta_m y}{l} \left\{ \frac{q_0 \alpha}{kl} \exp \left( -\frac{\beta_m^2 \alpha t}{l^2} \right) \int_{\tau=0}^t e^{i 2 \omega \tau} e^{\left( \frac{\beta_m^2 \alpha \tau}{l^2} \right)} * \right. \\
& \left. \sum_{n=1}^{\infty} 4 \frac{\beta_n^2 + B_3^2}{\beta_n^2 + B_3^2 + B_3} \exp \left( -\frac{\beta_n^2 \alpha (t - \tau)}{c^2} \right) \frac{\sin \left( \frac{\beta_n a}{2c} \right) \cos \frac{\beta_n x}{c}}{\beta_n} d\tau \right\} \\
& \quad (3.32)
\end{aligned}$$

The terms in the big bracket are the function of only  $x$ . Let's note them as

$$\begin{aligned}
\tilde{T}_x(x, t) = & \exp \left( -\frac{\beta_m^2 \alpha t}{l^2} \right) \frac{q_0 \alpha}{kl} \int_{\tau=0}^t e^{i 2 \omega \tau} e^{\left( \frac{\beta_m^2 \alpha \tau}{l^2} \right)} * \\
& \sum_{n=1}^{\infty} \frac{\beta_n^2 + B_3^2}{\beta_n^2 + B_3^2 + B_3} \exp \left( -\frac{\beta_n^2 \alpha (t - \tau)}{c^2} \right) \frac{\sin \left( \frac{\beta_n a}{2c} \right) \cos \frac{\beta_n x}{c}}{\beta_n} d\tau \\
& \quad (3.33)
\end{aligned}$$

Thus Eq. (3.33) can be written as:

$$\begin{aligned}
\tilde{T}(x, y, t) = & \sum_{m=1}^{\infty} \frac{\beta_m^2 + B_2^2}{\beta_m^2 + B_2^2 + B_2} \cos \frac{\beta_m y}{l} \tilde{T}_x(y, t) \\
& \quad (3.34)
\end{aligned}$$

Recall Eqs. (3.21) and (3.25), we had

$$\int_{x'=0}^{x'=\frac{a}{2}} G_{X23}(x, t | x, \tau) dy' = 2 \sum_{n=1}^{\infty} \frac{\beta_n^2 + B_3^2}{\beta_n^2 + B_3^2 + B_3} \exp \left( -\frac{\beta_n^2 \alpha (t - \tau)}{c^2} \right) \frac{\sin \left( \frac{\beta_n a}{2c} \right) \cos \frac{\beta_n x}{c}}{\beta_n}$$

$$& \quad (3.35)$$

$\tilde{T}_x(x, t)$  can be re-written as

$$\begin{aligned}
\tilde{T}_x(x, t) = & 2 \exp \left( -\frac{\beta_m^2 \alpha t}{l^2} \right) \left\{ \frac{q_0 \alpha}{kl} \int_{\tau=0}^t e^{i 2 \omega \tau} e^{\left( \frac{\beta_m^2 \alpha \tau}{l^2} \right)} \int_{x'=0}^{x'=\frac{a}{2}} G_{X23}(x, t | x', \tau) dx' d\tau \right\} \\
& \quad (3.36)
\end{aligned}$$

$$\text{Let } \tilde{T}_x(x, t) = \exp\left(-\frac{\beta_m^2 \alpha t}{l^2}\right) T'(x, t) \quad (3.37)$$

Then

$$T'(x, t) = \frac{2q_0\alpha}{kl} \int_{\tau=0}^t d\tau \int_{y'=0}^{y'=\frac{a}{2}} e^{i2\omega\tau} e^{\left(\frac{\beta_m^2 \alpha \tau}{l^2}\right)} G_{X23}(x, t|x', \tau) dx' \quad (3.38)$$

$T'(x, t)$  is the transient conduction temperature solution for the volumetric energy source [103, page 191]:

$$g(t) = \frac{q_0}{l} f(x) e^{i2\omega t} e^{\left(\frac{\beta_m^2 \alpha t}{l^2}\right)}, f(x) = \begin{cases} 1, & 0 < x < \frac{a}{2} \\ 0, & \frac{a}{2} < x < c \end{cases} \quad (3.39)$$

with the associated heat conduction equation:

$$\frac{\partial^2 T'}{\partial x^2} + \frac{1}{k} g(t) = \frac{1}{\alpha} \frac{\partial T'}{\partial t} \quad (3.40)$$

Substituting Eq. (37) into Eq. (3.40), we get

$$\exp\left(\frac{\beta_m^2 \alpha t}{l^2}\right) \left\{ \frac{\partial^2 \tilde{T}_x}{\partial x^2} + \frac{q_0}{lk} f(x) e^{i2\omega t} - \frac{\beta_m^2}{l^2} \tilde{T}_x - \frac{1}{\alpha} \frac{\partial \tilde{T}_x}{\partial t} \right\} = 0 \quad (3.41)$$

Equation (3.41) can be reduced to

$$\frac{\partial^2 \tilde{T}_x}{\partial y^2} + \frac{q_0}{lk} f(x) e^{i2\omega t} - \frac{\beta_m^2}{l^2} \tilde{T}_x - \frac{1}{\alpha} \frac{\partial \tilde{T}_x}{\partial t}, \quad 0 < x < c \quad (3.42)$$

Let

$$\theta(\omega, x) = \tilde{T}_x e^{-i2\omega t}, \tilde{T}_x = \theta e^{i2\omega t},$$

Then

$$\frac{\partial \tilde{T}_x}{\partial t} = 2\omega \theta i e^{i2\omega t} \quad (3.43)$$

Eq.(3.42) becomes

$$e^{i2\omega t} \left( \frac{\partial^2 \theta}{\partial x^2} + \frac{q_0}{lk} f(x) - \frac{\beta_m^2}{l^2} \theta - \frac{1}{\alpha} 2\omega \theta i \right) = 0 \quad (3.44)$$

Eq. (23) can be reduced to

$$\frac{\partial^2 \theta}{\partial x^2} - \left( \frac{\beta_m^2}{l^2} + \frac{1}{\alpha} 2\omega i \right) \theta = -\frac{q_0}{lk} f(x) \quad (3.45)$$

If we try to solve this Helmholtz equation (23b) in the classic way, complex math evaluating must be involved. Fortunately, ‘Fin type’ Green function [103, page 82-89] gives the solution directly.

$$\theta(x, t) = \alpha \int_{x'=0}^{x'=c} \frac{2q_0}{lk} f(x) \bar{G}_{X23}(x, x') dx' \quad (3.46)$$

where  $\bar{G}_{X23}(x, x')$  [103, page 580] is the steady-periodic Green function for the X21 case of Helmholtz equation. It satisfies

$$\frac{\partial^2 \bar{G}}{\partial x^2} - \left( \frac{\beta_m^2}{l^2} + \frac{1}{\alpha} 2\omega i \right) \bar{G} = -\frac{1}{\alpha} \delta(x - x'), \quad 0 < x < c \quad (3.47)$$

Let  $\sigma^2 = \frac{\beta_m^2}{l^2} + \frac{1}{\alpha} 2\omega i$ ,

$$\bar{G}_{X23}(x, x') = \frac{1}{2\alpha\sigma} \frac{e^{-\sigma|x+x'|} + e^{-\sigma|x-x'|} + R[e^{-\sigma(2c-|x-x'|)} + e^{-\sigma|2c-x-x'|}]}{1 - Re^{-2c\sigma}} \quad (3.48)$$

where  $R = \frac{k\sigma-h_2}{k\sigma+h_2}$

Normalize  $\bar{G}_{X23}(x, x')$ , we have

$$\bar{G}_{X23}^+(x^+, (x')^+) = \frac{1}{2\sigma^+} \frac{e^{-\sigma^+|x^+-(x')^+|} + e^{-\sigma^+|x^+-(x')^+|} + Re^{-\sigma^+(2A-|x^+-(x')^+|)} + Re^{-\sigma^+(2A-x^+-(x')^+|)}}{1 - Re^{-2\sigma^+}} \quad (3.49)$$

where

$$x^+ = \frac{x}{l}, \omega^+ = \frac{\omega\alpha^2}{l}, \sigma^+ = \sigma l, A = \frac{c}{l}, \bar{G}_{X23}^+ = \frac{\alpha}{l} \bar{G}_{X23} \quad (3.50)$$

Then

$$\theta(y, t) = \frac{2q_0c^2}{lk} \int_{x'=0}^{x'=\frac{a}{2c}} \bar{G}_{X23}^+(x^+, (x')^+) d(x')^+ \quad (3.51)$$

Software Maple is used to execute the integration. Denote the integration result as Q:

$$\begin{aligned} & \int_{x'=0}^{x'=\frac{a}{2c}} \bar{G}_{X23}^+(x^+, (x')^+) d(x')^+ = \\ & \left\{ \begin{array}{ll} \frac{-Re^{-\sigma^+(2A-x+A*ao2)} + Re^{-\sigma^+(2A-x^+-A*ao2)} + e^{-\sigma^+(x^+-A*ao2)} - e^{-\sigma^+(x^++A*ao2)}}{2\sigma^{+2}(1+e^{-2\sigma^+A})}, & \text{as } A*ao2 < x^+ < A; \\ \frac{1}{(\sigma^+)^2} + \frac{Re^{-\sigma^+(2A+x^+-A*ao2)} + Re^{-\sigma^+(2A-x^+-A*ao2)} - e^{-\sigma^+(-x^++A*ao2)} - e^{-\sigma^+(x^++A*ao2)}}{2(\sigma^+)^2(1-Re^{-2\sigma^+A})}, & \text{as } 0 < x^+ < A*ao2. \end{array} \right. \end{aligned} \quad (3.52)$$

$$\text{where } ao2 = \frac{a}{2c}, A*ao2 = \frac{a}{2l}.$$

Substituting Eq. (3.43) and (3.52) into Eq.(3.51), we have

$$\tilde{T}_x(x, t) = \frac{2q_0l}{k} e^{i2\omega t} * Q \quad (3.53)$$

Substituting Eq. (3.53) to Eq. (3.54), we get the temperature solution with improved convergence

$$\tilde{T}(x^+, y, t) = \frac{2q_0l}{k} e^{i2\omega t} \sum_{m=1}^{\infty} \frac{\beta_m^2 + B_2^2}{\beta_m^2 + B_2^2 + B_2} \cos \frac{\beta_m y}{l} * Q \quad (3.54)$$

Normalize the temperature result Eq. (3.54) by  $\frac{T^+}{T} = \frac{Ql}{k}$

$$\tilde{T}^+(x, y^+, \omega) = 2 \sum_{m=1}^{\infty} \frac{\beta_m^2 + B_2^2}{\beta_m^2 + B_2^2 + B_2} \cos \frac{\beta_m y}{l} * Q \quad (3.55)$$

Take the real part of Eq. (3.55) using Eq. (3.56), we will get the temperature solution  $T(x^+, y^+, t)$  in time range expressed by Eq. (3.57) and we will call it as the solution obtained from the ‘original’ GFs in this chapter.

$$T(x^+, y^+, t) = \text{Real } \tilde{T}(x^+, y^+, t) \quad (3.56)$$

$$T^+(x^+, y, t) = 2\text{Real} \left\{ e^{i2\omega t} \sum_{m=1}^{\infty} \frac{\beta_m^2 + B_2^2}{\beta_m^2 + B_2^2 + B_2} \cos \frac{\beta_m y}{l} * Q \right\} \quad (3.57)$$

### 3.2.4 Temperature solution in frequency domain

In order to verify the temperature solution obtained above, an independent way is employed to seek the temperature solution, that is using frequency range steady-periodic Green’s Functions. Since in this work the applications are limited to steady-periodic heating, the resulting temperature  $T(x, y, t)$  can be written as the real part of a complex-valued  $T(x, y, \omega)$ , which is interpreted as the steady-periodic temperature at a single frequency  $\omega$ . The steady-periodic temperature will be found with the Green’s function method. Cole [104] gives a variety of GFs for steady-periodic heat conduction in two-dimensional bodies in rectangular coordinates. The GF for X23Y23 geometry presented in Cole’s paper is used here.

The steady-periodic temperature is given by the following integral equation (see [103])

$$T(x, y, \omega) = \frac{Q\alpha}{k} \int_0^{x'= \frac{a}{2}} G_{X23Y23}(x, x', y, y' = 0, \omega) dy' \quad (3.58)$$

According to Cole [104], the steady periodic GFs for rectangular body are given below in a single-sum form

$$G_{X23Y23}(x, y, \omega | x', y' = 0) = \sum_{n=1}^{\infty} \frac{Y_n(x) Y_n^*(x')}{N_x} P(y, y' = 0, \sigma) \quad (3.59)$$

where

$$Y_n(x) = \cos(\gamma_n x), Y_n^*(x') = \cos(\gamma_n x'), \quad (3.60)$$

$$\gamma_n c * \tan(\gamma_n c) = B_3, B_3 = \frac{h_3 c}{k}, \quad (3.61)$$

$$N_x^{-1}(\gamma_n) = \frac{2}{c} \frac{(\gamma_n c)^2 + B_3^2}{(\gamma_n c)^2 + B_3^2 + B_3} \quad (3.62)$$

$$P(y, y' = 0, \sigma) = \frac{(k\sigma - h_2)e^{-\sigma(2l-y)} + (k\sigma + h_2)e^{-\sigma y}}{\alpha\sigma[k\sigma + h_2 - (k\sigma - h_2)e^{-2\sigma l}]} \quad (3.63)$$

where  $\sigma^2 = \gamma_n^2 + \frac{\omega j}{\alpha}$ .

Therefore,

$$G_{X23Y23}(x, y, \omega | x', y' = 0) = \sum_{n=0}^{\infty} \cos(\gamma_n x) \cos(\gamma_n x') \frac{2}{c} * \frac{(\gamma_n^+)^2 + B_3^2}{(\gamma_n^+)^2 + B_3^2 + B_3} \frac{(k\sigma - h_2)e^{-\sigma(2l-y)} + (k\sigma + h_2)e^{-\sigma y}}{\alpha\sigma[k\sigma + h_2 - (k\sigma - h_2)e^{-2\sigma l}]} \quad (3.64)$$

After normalizing by  $\frac{T^+}{T} = \frac{Ql}{k}$ , the temperature solution can be obtained as

$$\begin{aligned}
T^+(x, y, \omega) &= 2 \sum_{n=1}^{\infty} \frac{\cos(\gamma_n^+ x^+/A) \sin(\gamma_n^+ a o 2)}{\gamma_n^+ \sigma^+} \frac{(\gamma_n^+)^2 + B_3^2}{(\gamma_n^+)^2 + B_3^2 + B_3} \frac{(\sigma^+ + B_2)e^{-\sigma^+ y^+} + (\sigma^+ - B_2)e^{-\sigma^+ (2-y^+)}}{(\sigma^+ + B_2) - (\sigma^+ - B_2)e^{-2\sigma^+}}
\end{aligned} \tag{3.65}$$

where  $y^+ = \frac{y}{l}$ ,  $\gamma_n = \frac{\gamma_n^+}{c}$ ,  $\sigma^+ = \sqrt{\frac{(\gamma_n^+)^2}{A^2} + j\omega^+}$ ,  $B_2 = \frac{h_2 l}{k}$ .

Take the real part of Eq. (3.65), we will get the temperature solution  $T(x^+, y, t)$  in time domain shown in Eq. (3.66) and we will call it as the solution obtained from the ‘alternative’ GFs in this chapter.

$$\begin{aligned}
T^+(x, y, t) = \text{Real} \left[ 2 \sum_{n=1}^{\infty} \frac{\cos(\gamma_n^+ x^+/A) \sin(\gamma_n^+ a o 2)}{\gamma_n^+ \sigma^+} \frac{(\gamma_n^+)^2 + B_3^2}{(\gamma_n^+)^2 + B_3^2 + B_3} * \right. \\
\left. \frac{(\sigma^+ + B_2)e^{-\sigma^+ y^+} + (\sigma^+ - B_2)e^{-\sigma^+ (2-y^+)}}{(\sigma^+ + B_2) - (\sigma^+ - B_2)e^{-2\sigma^+}} e^{i2\omega t} \right]
\end{aligned} \tag{3.66}$$

### 3.2.5 Average temperature solution

The average temperature over the heating region is of great importance for the  $3\omega$  measurements where information is extracted from a heated film and the average temperature is associated with the collected information. The spatial-average temperature on the heater may be evaluated from the surface temperature by

$$\overline{T^+}(\omega) = \frac{2}{a} \int_0^{x=a/2} T^+(x^+, y=0, \omega) dx = \frac{2}{a} \int_0^{x=a/2} T^+(x^+, y=0, \omega) dx$$

$$\tag{3.67}$$

Substituting the temperature solution Eq. (3.55) into Eq. (3.67) where Software Maple is used to do the integration, the analytical average temperature solution from the “original” GFs is expressed as:

$$\overline{T^+}(\omega) = \sum_{m=1}^{\infty} \left[ \frac{-Re^{-2\sigma^+ A} + Re^{-2\sigma^+ A(1-ao2)} + e^{-2\sigma^+ A*ao2} - 1}{A * ao2(\sigma^+)^3(1 - Re^{-2\sigma^+ A})} + \frac{2}{(\sigma^+)^2} \right] \quad (3.69)$$

where  $R = \frac{\sigma^+ - H*B2}{\sigma^+ + H*B2}$ ,  $H = \frac{h_3}{h_2}$ ,  $\sigma^+ = \sqrt{\beta_m^2 + 2 \frac{\omega l^2}{\alpha} i}$ .

Substituting the temperature solution Eq. (3.65) into Eq. (3.67), the analytical average temperature solution from the ‘alternative’ GF is expressed as:

$$\overline{T^+}(\omega^+) = \frac{2}{ao2} \sum_{n=1}^{\infty} \frac{\sin^2(\gamma_n^+ ao2)}{(\gamma_n^+)^2 \sigma^+} \frac{(\gamma_n^+)^2 + B_3^2}{(\gamma_n^+)^2 + B_3^2 + B_3} \frac{(\sigma^+ + B_2)e^{-\sigma^+ x^+} + (\sigma^+ - B_2)e^{-\sigma^+(2-x^+)}}{(\sigma^+ + B_2) - (\sigma^+ - B_2)e^{-2\sigma^+}} \quad (3.70)$$

### 3.2.6 Comparison of the temperature solutions

**Verification** Verification of numerical results is an important part of any numerical calculation. These alternative temperature expressions represent the same unique solution, but they have different computational behaviors. They may be checked, one against the other, to verify the accuracy of the numerical results obtained.

- 1) Three temperature solutions were discussed in the previous sections. They were obtained from the time domain GFs, the ‘original’ GFs and the ‘alternative’ GFs. Equations. (3.32), (3.57) and (3.66) represent the spatial distribution of temperature solution obtained from these three approaches respectively. They should give the same temperature profile. Taking  $a_0 = 0.0001, c_0 = 0.01, l_0 = 0.003, h_{20} = h_{30} = 5, k_x = 0.5, k_y = 5, f = 0.01$  (all in SI unit, all the parameters in all the figure of this thesis are in SI unit if no specific statement).

Figure 3.2 represents the numerical temperature result from the three temperature expressions.

- 2) Equations (3.57) and (3.66) represent the average temperature solution obtained from two different GFs. They are checked, one against the other, to verify the accuracy of the numerical results.
- 3) The temperature solution obtained from GFs for geometry and boundary conditions  $X21Y21$  is also used to test the result solved from  $G_{X23Y23}$  with setting the value of heat coefficients  $h_2$  and  $h_3$  very large.

**Computing issues** Considerable programming effort is needed to obtain accurate numerical temperature solutions. Although they give the same numerical results like described above, those alternative temperature expressions have different computational behaviors. The following remarks can be made:

- 1) Days of computer time were required to compute the 40 temperature values plotted for the curve of the time-domain solution Eq. (3.32) in Figure 3.2. Computations were carried out on Windows XP with Intel Core 2 Quad CPU (Q6600@2.40 GHz). The reasons that cause low conversion speed of Eq. (3.32) is discussed in Section 3.2.2. However, it only took seconds to plot the curves for the ‘original’ solution Eq. (3.57) and the ‘alternative’ solution (3.66). Since using Eq. (3.32) is relatively much more time consuming, it won’t be employed for calculation in this work.
- 2) As for equations (3.57) and (3.66), they both converge quite fast when the value of  $c$  (half of sample length) is small, but the convergence rate of the temperature solution from the alternative GFs (Eq. (3.66)) gets slower as the value of  $c$

increases. Mathematically, the parameter  $c$  appears solely in the exponential part, which speeds the decaying rate as  $c$  gets larger. In the next part we will see the effect of boundary condition at  $y = c$  can be often neglected for our case, so we could assume the sample is infinitely long ( $c \rightarrow \infty$ ). Then simply using Eq. (3.56) and dropping the exponential part which is zero as  $c \rightarrow \infty$  would greatly save the computing time.

- 3) Although either the ‘original’ or ‘alternative’ temperature solution is affordable to use to obtain the numerical results for plotting temperature profile versus location or time, the convergence rate is still a big matter for the inverse curve fitting procedure which requires a large numbers of interminable temperature evaluations, and the corresponding computation behavior is much more complicated.

### 3.3 Phase results

As described in Section 3.2, the frequency-space steady-periodic temperature  $T(\omega)$  was stated in a complex form. Mathematically, the amplitude of the temperature  $A$ , and phase of temperature  $\phi$  are defined as follows:

$$A = \sqrt{[Imag(T)]^2 + [Real(T)]^2} \quad (3.71)$$

$$\phi = \tan^{-1}[Imag(T)/Real(T)] \quad (3.72)$$

where ‘Imag’ and ‘Real’ are the imaginary and real parts of the complex temperature, respectively.

Physically, this  $\phi$  represents the phase lag between temperature and heating. Suppose a plate having a periodic heat flux at one surface, a periodic temperature field will be

present throughout the plate after the initial transients decay away. However, depending on the frequency, the amplitude of the periodic temperature  $A$  decreases in the direction away from the heat flux source. The phase lag  $\phi$  exists because there is a time delay between temperature response and heating. A one-to-one relation exists between this phase delay and the thermal properties of the plate [105]. Generally the phase lag is independent of the exact value of the amplitude of the measured temperature. Both phase and amplitude data will be used simultaneously to estimate the thermal properties in Chapter 5.

### 3.3.1 Parameters in the analytical solution

In this section, all the parameters that the theoretical phase results depend on are discussed.

Equation (3.69) shows the temperature solution and therefore the analytical phase result for the rectangular geometry  $X23Y23$  depends on the following parameters:

$$\phi_{X23Y23}(\omega^+) = \phi_{X23Y23}(\omega^+, B_2, H, A, ao2) \quad (3.73)$$

$$\text{where } \omega^+ = \frac{\omega a^2}{\alpha} = \frac{\omega a_0^2}{k_x}, B_2 = \frac{h_2 l}{k} = \frac{h_{20} l_0}{k_y}, H = \frac{h_3}{h_2} = \frac{h_{30}}{h_{20}}, A = \frac{c}{l} = \frac{c_0}{l_0} \sqrt{\frac{k_y}{k_x}}, ao2 = \frac{a}{2c} = \frac{a_0}{2c_0}.$$

Recall: here  $a, c, l, h_2$  and  $k$  are scaled parameters in the scaled coordinates, and  $a_0, c_0, l_0, h_{20}, h_{30}$ ,  $k_x$  and  $k_y$  are the original parameters in the original anisotropic coordinates.

If the length of sample  $c$  is large enough, the sample can be taken as an infinite region. That is, the effect of parameters on the boundary of  $x=c$  can be ignored. Then the geometry becomes  $X20Y23$ , and the phase result would depend on:

$$\phi_{X20Y23}(\omega^+) = \phi_{X23Y20}(\omega^+, B_2, W) \quad (3.74)$$

$$\text{where } W = \frac{l}{a} = \frac{l_0}{a_0} \sqrt{\frac{k_x}{k_y}}$$

In the following sections, we will get the conclusion that Equation (3.74) is sufficient for our study. The effect of all the parameters to phase results will be discussed.

### 3.3.2 The influence of convection

The influence of convection at  $y=l$  is characterized by the corresponding Biot number  $B_2 = \frac{hl}{k}$ . Phase results for various values of  $B_2$  are presented in Figs 3.3-3.5. As for thermal conductivities, the estimated values of carbon fiber material are used as  $k_x=5\text{W}/(\text{mK})$  and  $k_y=0.5\text{W}/(\text{mK})$ . The values of  $c_0$  and  $a_0$  are taken as  $c_0=0.01\text{m}$ ,  $l_0=0.003\text{m}$ ,  $a_0=0.1\text{mm}$ . They are the actual size of the samples used for experimental measurement in this work. The following remarks can be made:

- 1) In Fig. 3.3, the phase results with different Biot number tend to be the same as the normalized frequency  $\omega^+$  gets larger. This makes sense physically, since the periodic temperature oscillations can only be observed for depth  $y_0$  belonging to the following interval:

$$0 < y_0 < D_p \sim 2\pi \sqrt{\frac{2\alpha}{\omega}} \quad (3.75)$$

where  $D_p$  is often called the ‘penetration depth’, which decreases as frequency increases. Therefore for higher frequency a less deep region of the sample is participating in the periodic temperature variations. That is, the influence at  $y=l$  damps out as frequency goes larger. Likewise, this explains why phase results

tend to agree for different values of  $c_0$  in larger frequency range shown in Figs 3.4 and 3.5.

- 2) Figure 3.3 also shows for the same frequency  $\omega^+$  the larger (absolute value) phase result occurs at smaller value of Biot number representing smaller convection cooling effect (close to insulated surface). As the convection effect increases the phase falls, which physically makes sense since with vigorous convection there is a smaller volume of the sample body participating in the heat transfer, and the phase lag is smaller when the thermal mass is smaller.
- 3) Figures 3.3-3.5 show phase result tends toward zero as frequency  $\omega^+$  becomes small. This is because heating at small frequency is close to steady heating, and there is no delay since temperature has enough time to respond.
- 4) Figures 3.4 and 3.5 show the phase results with various values of sample length  $c_0$  at larger Biot value  $B_2=20$  and smaller Biot  $B_2=0.03$  ( $h_{20} \approx 5 \text{ W/m}^2 \cdot \text{K}$ ), respectively. It can be seen from Fig. 3.4 that for smaller Biot, the rectangular sample cannot be taken as a slab until  $c_0 \geq 0.1 \text{ m}$ . However, for larger Biot, it can be taken as a slab at  $c=0.01 \text{ m}$ . On one hand, performing the  $3\omega$  experiment on a sample with length 100 mm is apparently not practical; on the other hand the slab geometry could simplify the theoretical solution and improve the convergence rate a lot for numerical calculation. Therefore larger Biot condition is better in this sense.

Also larger Biot number is easy to be realized physically in the lab. By simply placing the  $y=l$  side of the sample on a plate with much larger thermal conductivity and much larger size relative to the sample, like copper or aluminum

block, which could make the hypothesis of using the boundary condition of the first kind valid. This also saves the effort for measuring the value of heat coefficient  $h_{20}$  and  $h_{30}$  at  $y=l$  if using the second kind of boundary condition.

Consequently, we get the conclusion that the first kind of boundary condition is perhaps the best boundary condition at the  $y=l$  side of the sample for measurement. Under this condition the sample with rectangular geometry will be taken as a slab theoretically. We will also focus our theoretical study mainly on large Biot condition.

### 3.3.3 The effect of thickness

In the previous section, we got the conclusion that the  $X23Y23$  model could be transformed to  $X20Y21$  as the first kind of boundary condition is satisfied at  $y=l$  and  $c \geq 0.01$  m. Then Equation (3.74) could be expressed as:

$$\emptyset_{X21Y20}(\omega^+) = \emptyset_{X23Y20}(\omega^+, W_0, \frac{k_y}{k_x}) \quad (3.76)$$

$$\emptyset_{X21Y20}(\omega) = \emptyset_{X23Y20}(\omega, a_0, W_0, k_x, k_y) \quad (3.77)$$

$$\text{where } \omega^+ = \frac{\omega a^2}{\alpha} = \frac{\omega a_0^2}{k_x/\rho c_p}, \quad W_0 = \frac{l_0}{a_0}$$

A comment is needed on Eq. (3.76). It shows phase versus normalized frequency is dependent only on the ratio of  $k_y$  and  $k_x$  and the value  $W_0$  mathematically, but the phase behavior versus the actual frequency in unit Hz is still dependent on the value of  $k_y$ ,  $k_x$ ,  $a_0$ , and  $l_0$  representing by Eq. (3.77).

Figure 3.6 is the theoretical phase lag results over a wide range of normalized frequencies for various values of  $W_0$ . It shows the phase curves versus  $\omega^+$  have different

shapes with different  $W_0$ . In order to provide more straightforward insight into the behavior Eq. (3.77) represents, phase lag results versus the frequencies without normalization in unit Hertz are plotted in Figs 3.7-3.9.

Figure 3.7 shows the phase versus frequency in Hertz for different values of  $l_0$  with the ratio  $W_0$  fixed. The curves have very similar shapes, but shift along the frequency axis. Mathematically it is because frequency  $\omega^+$  is normalized by  $a_0$  in Eq. (3.77) where  $\emptyset_{x21y20}(\omega^+)$  only depends on  $W_0$  and  $\frac{k_y}{k_x}$ .

Figure 3.8 shows the phase results versus frequency in Hertz for various values of sample thickness  $l_0$  with fixed heater width  $a_0$ . It can be seen that phase starts to fall at larger frequency range for the cases with smaller  $l_0$ . This behavior physically makes sense. As the slab becomes thinner with fixed heated width, a smaller thermal mass participates in the heat transfer so temperature can ‘follow’ the oscillating of heating even at relatively larger frequencies which makes the zero phase lag at larger frequency range.

Figure 3.9 shows the phase results versus frequency in Hertz for various values of  $a_0$  with fixed  $l_0$ . Here the phase starts to fall at larger frequency range for the cases with smaller  $a_0$ . This agrees with the ‘thermal mass’ theory discussed in the previous paragraph. As the heater becomes narrower, a smaller thermal mass participates in the heat transfer so temperature can ‘follow’ the oscillating of heating even at relatively larger frequencies which makes the zero phase lag at larger frequency range.

In practice, we use a lock-in amplifier to collect the phase information for each frequency, and there is a lower frequency limit the lock-in amplifier can reach which is 0.001Hz. In this sense smaller  $l_0$  or larger  $a_0$  is preferred in the sense of avoiding the low frequency lock-in limit by our analysis above. However we want the width of platinum

heater as small as possible to obtain the largest sensitivity for temperature measurement and the narrowest we can get by depositing platinum on a mask is 0.1 mm. That is, the value of  $a_0$  is basically fixed. Therefore the thinner the sample is, the more possible the phase information can be collected by the Lock-in amplifier during measurement. The thinnest thickness of carbon-fiber material we can reach by cutting with diamond saw is about 2~3 mm. Figure 3.8 shows the phase lag starts falling at  $\omega > 0.001$  Hz for 2~3 mm wide samples, so lock-in amplifier should be able to collect some of the falling phase information.

### 3.3.4 The effect of $k_x$ and $k_y$

In the previous sections, we discussed all those controllable parameters including sample size, heater size and the boundary conditions. In this section we will study on how theoretical phase lag changes with unknown thermal conductivities  $k_x$  and  $k_y$ . This gives a basic idea what the experimental results might be like.

Figure (3.10) shows the theoretical phase lag results over dimensional frequencies for different values of  $k_x$  with fixed  $k_y$ . It can be seen at a fixed frequency point as  $k_x$  increases, phase lag becomes smaller. This is because higher thermal conductivity means higher ‘ability’ for temperature to ‘catch up’ the heating oscillation which makes the ‘lag’ smaller. The same theory also explains why as  $k_y$  increases phase lag decreases at a fixed frequency in Figure (3.11).

Figures (3.10) and (3.11) also suggest the best frequency range for estimating  $k_x$  and  $k_y$  respectively. It can be seen the small frequency range [0.001 Hz, 0.1 Hz] is perhaps the best region for estimating  $k_y$  since phase looks sensitive to the changing of  $k_y$  over there.

The intermediate and large ranges [0.1 Hz, 1000 Hz] are perhaps the best regions for  $k_x$ . We will come back to discuss this sensitivity issue regarding the optimal experimental design in Section 3.4.

### 3.4 Sensitivity analysis

The objective of this section is to perform sensitivity analysis and to demonstrate the useful range of frequencies for a specific application. This procedure for measuring thermal properties is a type of inverse problem. An important part of every multi-parameter inverse problem is the sensitivity coefficients. In the inverse model, the anisotropic thermal conductivity  $k_x$  and  $k_y$  are determined by varying the parameter until best-match between measured data and model calculated phase solution are obtained. Therefore, for successful estimation of multiple parameters, the sensitivity coefficients of all the unknown parameters must be large and linearly independent (equivalently they must have different shapes when plotted). This is also the way to find the best frequency range for seeking each unknown parameter. The sensitivity coefficients are derivatives of the measurable data with respect to the sought-after parameters. The sensitivity coefficients of phase to  $k_x$  and  $k_y$  are given by

$$S_{k_x} = k_x \frac{\partial \phi}{\partial k_x} \quad (3.78)$$

$$S_{k_y} = k_y \frac{\partial \phi}{\partial k_y} \quad (3.79)$$

Using Eq. (3.78) or (3.79), the value of  $k_x$  and  $k_y$  have to be given beforehand. One possible concern is that the sensitivity curves might not be general enough for the unknown property values due to the specified given parameter value. Figures 3.12-3.13

show the sensitivity of phase to  $k_x$  and  $k_y$  for different values of  $k_x$  and  $k_y$  in frequency range  $[10^{-4} \text{ Hz}, 10^4 \text{ Hz}]$ . The  $k_x$  value of carbon fiber is considered to be in the range of  $5\sim15 \text{ W/(mK)}$ , and the value of  $k_y$  might be in the region of  $0.3\sim0.9 \text{ W/(mK)}$ . It can be seen that the concrete value of  $k_x$  and  $k_y$  in the possible ranges for our sample material does not have much effect on sensitivity coefficients. We can still have a basic idea about the sensitivity behavior.

Figure 3.14 plots the sensitivity coefficient for  $k_x$  and  $k_y$  together. It can be seen that the sensitivity coefficients for  $k_x$  and  $k_y$  are independent since they have different shapes, which suggests the possibility for simultaneously estimating both  $k_x$  and  $k_y$ .

### **3.4.1 The effect of $l_0$ and $a_0$ on the sensitivity coefficients**

Figure 3.15 shows the sensitivity coefficients of phase to the in-plane thermal conductivity  $k_x$  for various sets of sample thickness  $l_0$  and heater width  $a_0$ . It can be seen that the best frequency range for estimating  $k_x$  mainly depends on the value of heater width  $a_0$  but not sample thickness  $l_0$ , which makes sense since  $k_x$  is in the direction of heater width. For fixed sample thickness  $l_0$ , the best sensitivity range moves to the right along the frequency axis as heater width  $a_0$  decreases. This makes sense physically since while the heater gets narrower, there is a smaller mass participating in the heat transfer so the phase is more sensitive to thermal conductivity variation at larger frequencies. This also agrees with the conclusion we drawn from Figure 3.8.

Figure 3.16 shows the sensitivity coefficients of phase to the through-thickness thermal conductivity  $k_y$  for various sets of sample thickness  $l_0$  and heater width  $a_0$ . It can be seen that the best frequency range for estimating  $k_y$  mainly depends on the value of sample thickness  $l_0$  but not heater width  $a_0$ , which makes sense since  $k_y$  is in the direction

of sample thickness. For fixed heater width  $a_0$ , the sensitivity gets larger and the best sensitivity range shifts to the right along the frequency axis as sample length  $l_0$  decreases. This can also be explained by ‘thermal mass’ theory discussed in the last paragraph. This agrees with the conclusion drawn from Figure 3.9. The actual heater width in the experiment is between 0.1-0.2mm. For heater width in this range, Figure 3.16 shows significant sensitivity of phase to  $k_y$ .

The smallest sample thickness we can fabricate is 3mm. Figure 3.15 shows large values of the sensitivity of phase to  $k_x$  as  $a_0=0.1\sim0.3$ mm for the frequency range [0.01Hz, 0.1Hz]. Figure 3.16 shows large values of the sensitivity of phase to  $k_y$  at  $l_0=3$ mm in frequency range of [10Hz,  $10^3$ Hz]. Later, in Chapter 4, we show that nice experimental results are possible over the frequency range [0.01Hz, 1000Hz]. These two facts provide the premise for successful estimation of the unknown thermal conductivities  $k_x$  and  $k_y$  based on sample thickness 3 mm and based on experimental measurements over that frequency range encompassing both low frequencies important for  $k_x$  and the higher frequencies important for  $k_y$ .

### **3.4.2 The best frequency range for estimating $k_x$ and $k_y$**

Figures 3.12-3.16 also suggest that the best frequency range for estimating  $k_x$  roughly falls in the region [10Hz, 1000Hz], if the value of heater width is between 0.1 mm and 0.2 mm; while the best frequency range for estimating  $k_y$  roughly falls in the region [0.001Hz, 1Hz], if the value of sample length is between 1 mm and 3 mm. This enhances our confidence for obtaining the reasonable result through the  $3\omega$  measurement system since all these frequency ranges are within the working range of a Lock-in amplifier. At

$a_0=0.1$  mm, the best frequency range for  $k_x$  is in [100Hz, 1000Hz], which even avoids the region around 60 Hz, where the most white noise exists. That the sensitivity of phase to  $k_x$  and  $k_y$  are smaller at larger and smaller frequencies respectively makes sense physically since larger thermal conductivity responds faster: on one hand, at small frequencies temperature tends to be able to follow heating oscillation easier, thereby presenting smaller phase delay; on the other hand, heat propagates faster along  $x$  direction than  $y$  direction ( $k_x \gg k_y$ ). Thus, measurements over a large frequency range must be performed and data included into the inverse problem solution to obtain sensitivity to both parameters. These best frequency results also agree with the conclusion we obtained from Figure 3.10 and 3.11.

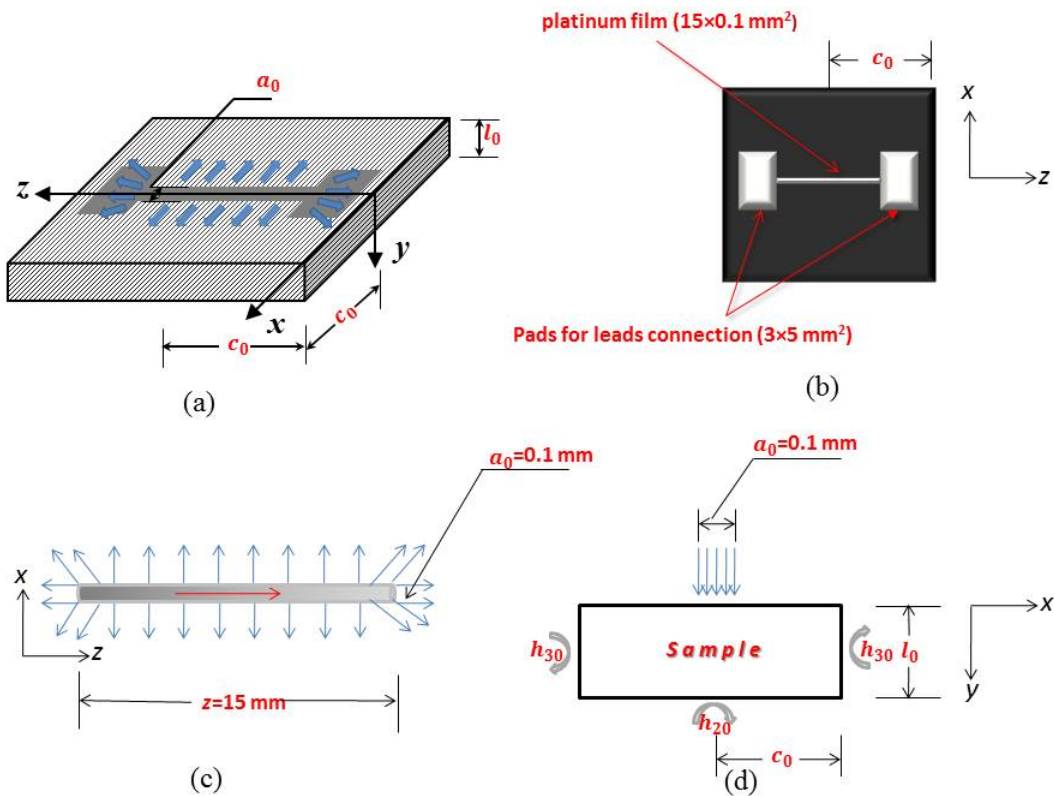
### 3.5 Summary

This chapter is devoted to the analysis of theoretical temperature solutions. It is divided into four parts. Section 3.1 is about building the anisotropic heat transfer model. A two dimensional model is built based on the discussed assumptions.

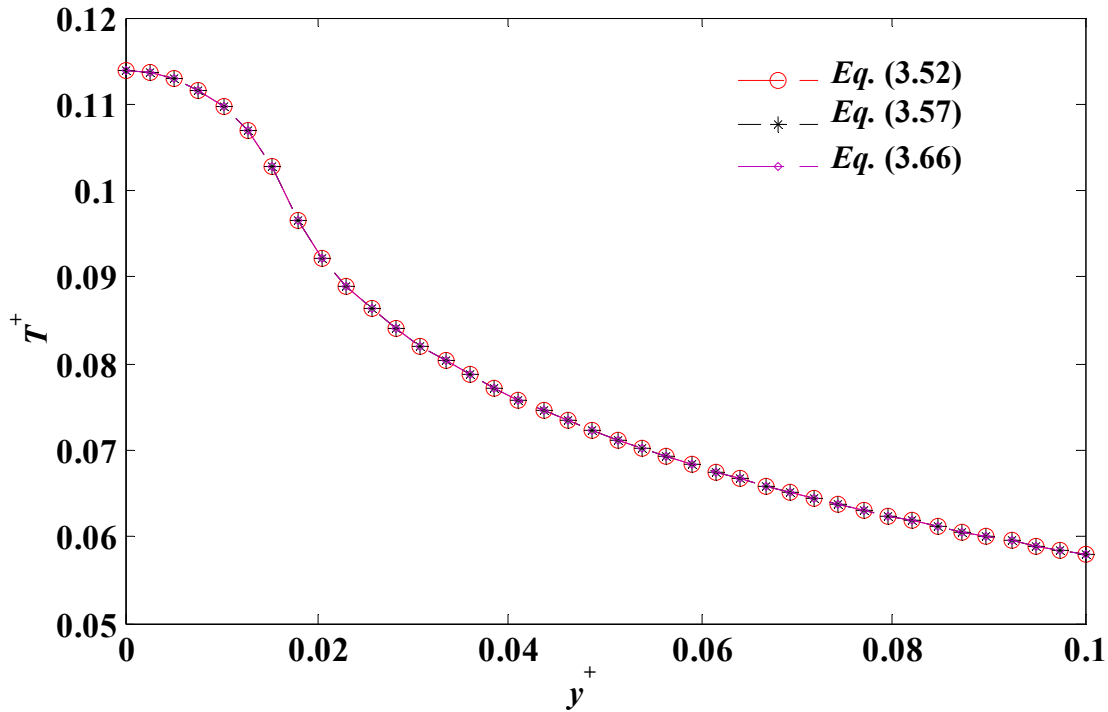
Section 3.2 is about solving the model and obtaining a temperature solution with affordable convergence rate. The temperature solutions obtained from three independent ways are used to verify each other. By comparison, the temperature solution Eq. (3.57) with improved convergence rate is picked for calculation. It saves days of computing time compared to the fundamental temperature solution Eq. (3.32) obtained in time domain.

Section 3.3 presents numerical phase results and the influence of several parameters is discussed. Sensitivity analysis is carried out in Sec. 3.4, where it is concluded that the best frequency range for property estimation could be in the range of [0.01Hz, 1000Hz].

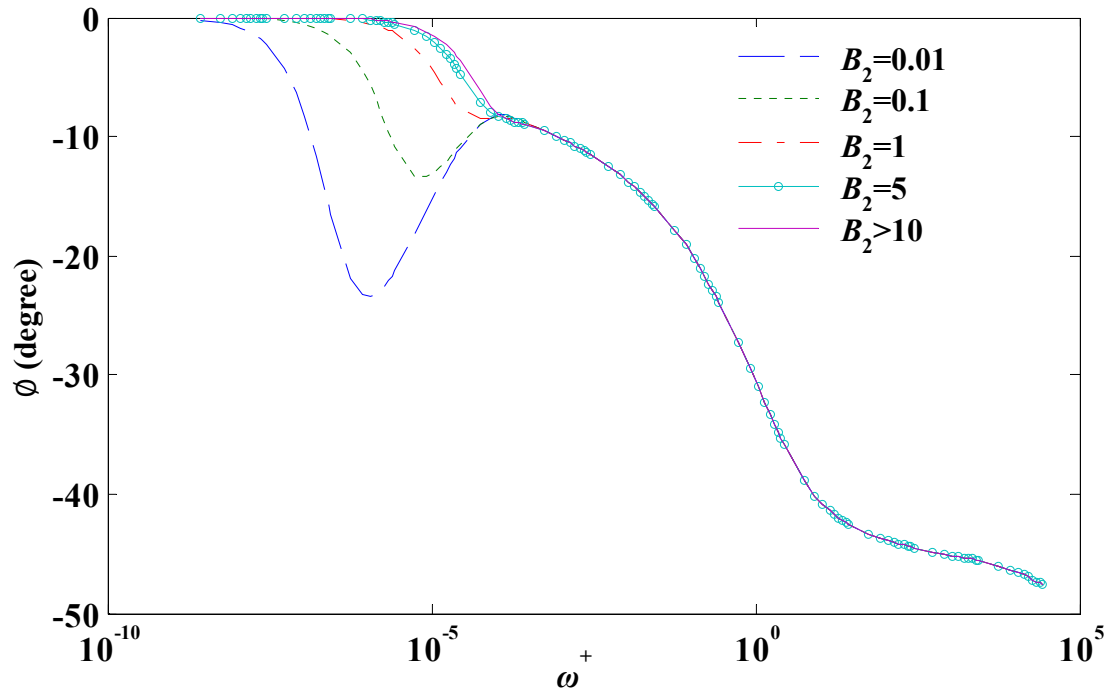
Sensitivity analysis in Sec 3.4 discusses the possibility for successful parameter estimation.



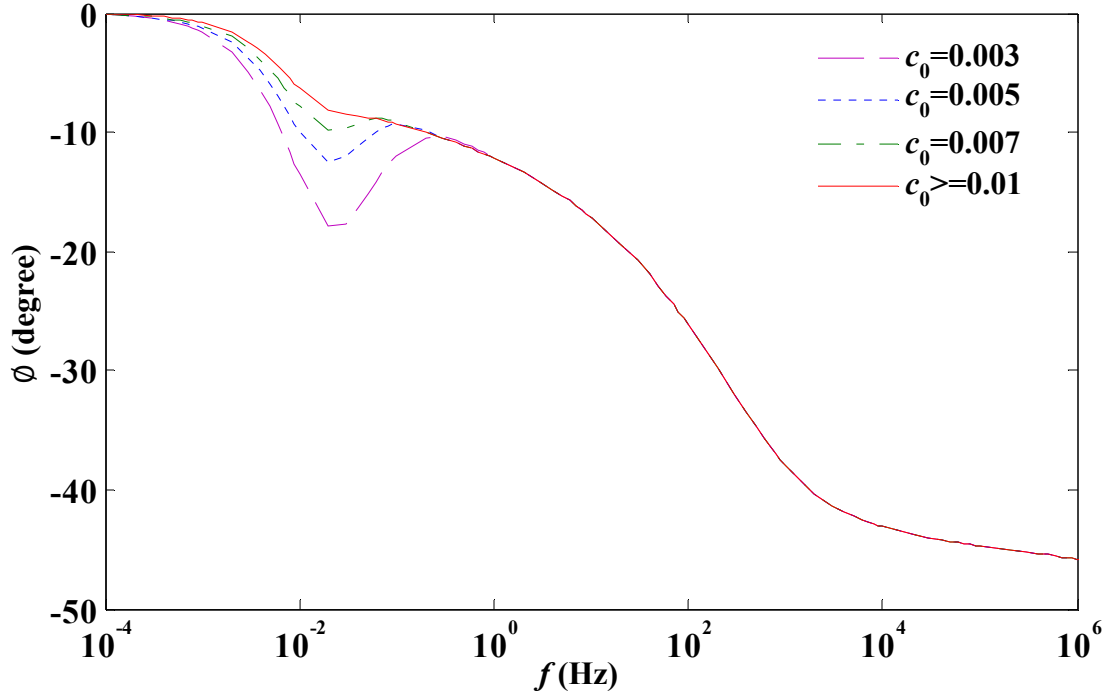
**Figure 3.1 Heat transfer geometry** a) 3-D geometry; b) the heating side of the sample with a platinum film on it; c) top view of heater width with the directions of heating flows around the platinum film; d) side view of sample and boundary conditions



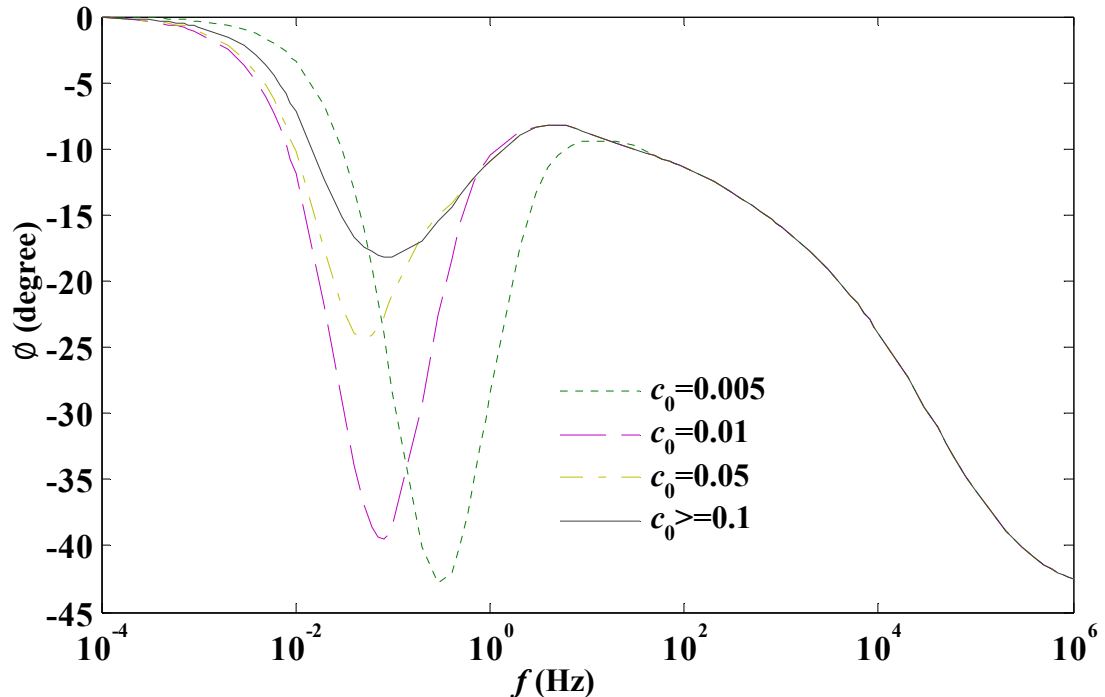
**Figure 3.2 Verification of the two analytical temperature solutions numerically**  
 $a_0 = 0.0001, c_0 = 0.01, l_0 = 0.003, h_{20} = h_{30} = 5, k_x = 5, k_y = 0.5, f = 0.01$



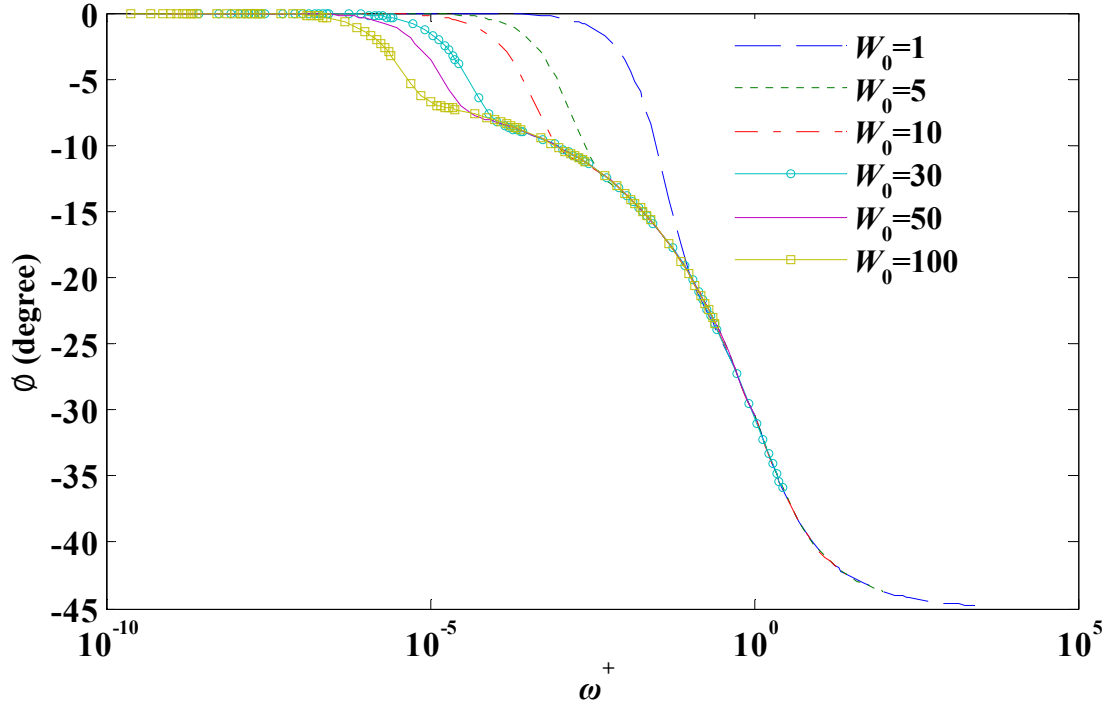
**Figure 3.3 Phase (in Degree) versus frequency for various Biot number**  
 $c_0 = 0.01, l_0 = 0.003, a_0 = 0.0001, k_x = 5, k_y = 0.5$



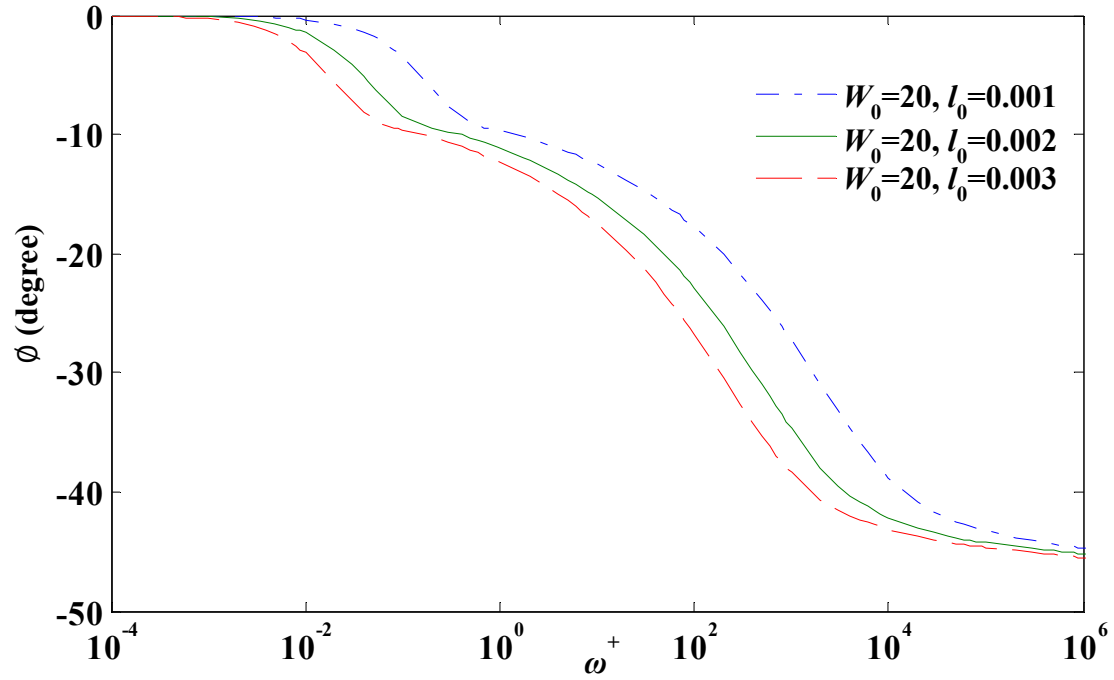
**Figure 3.4 Phase (in Degree) at large Biot for various values of  $c_0$**   
 $l_0 = 0.003, a_0 = 0.0001, k_x = 5, k_y = 0.5, B_2=20$



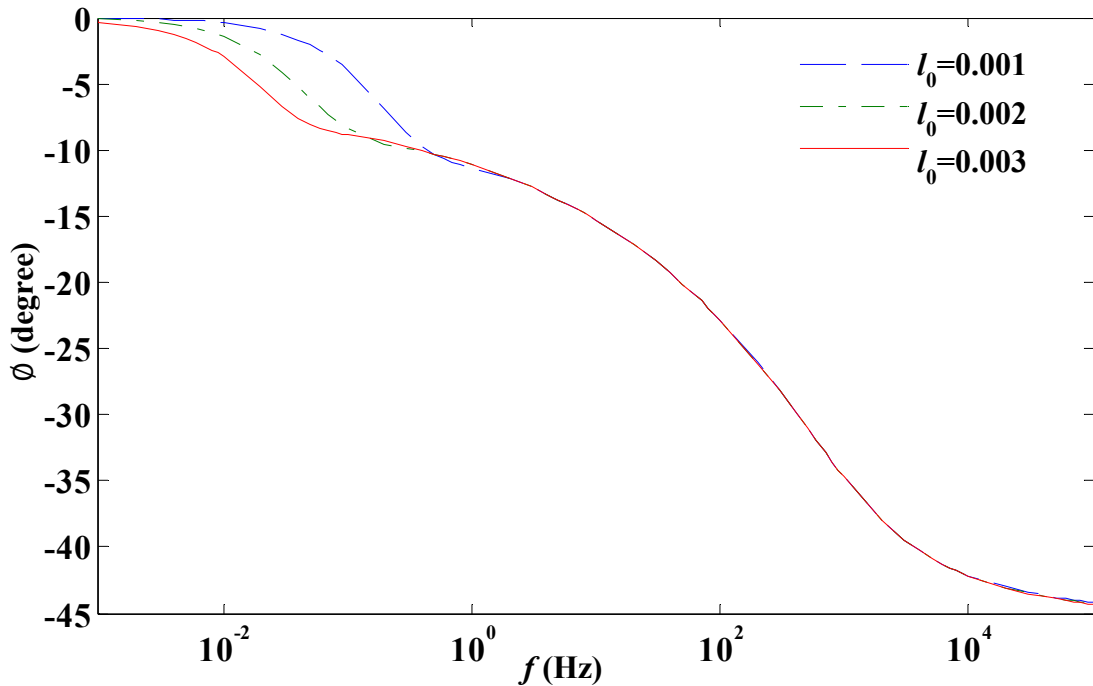
**Figure 3.5 Phase (in Degree) at small Biot for various values of  $c_0$**   
 $l_0 = 0.003, a_0 = 0.0001, k_x = 5, k_y = 0.5, B_2=0.03$



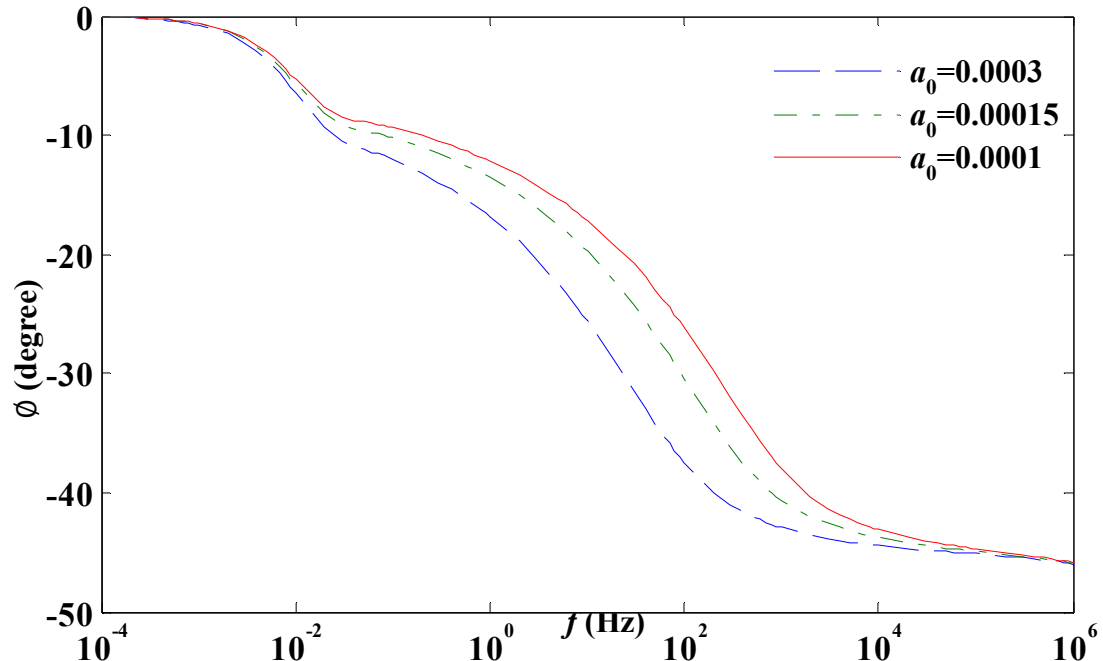
**Figure 3.6 Phase versus frequency for various values of  $W_0$**   
 $k_x = 5, k_y = 0.5, B_2=20$



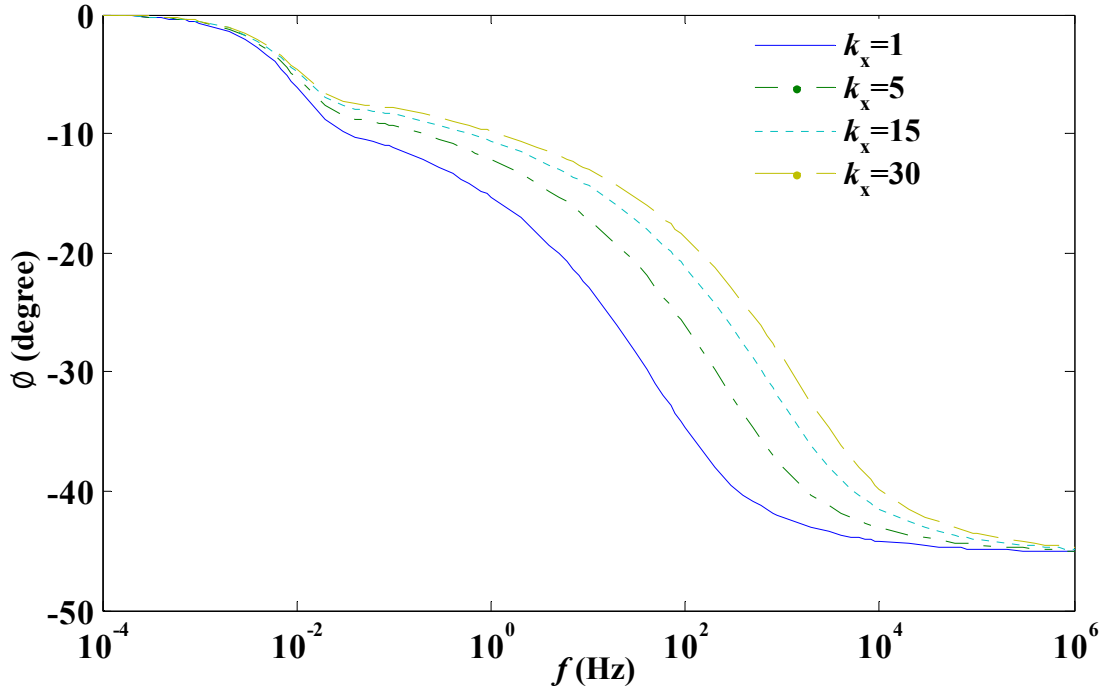
**Figure 3.7 Phase versus frequency for various values of  $l_0$  with fixed  $W_0$**   
 $W_0 = 20, k_x = 5, k_y = 0.5, B_2=20$



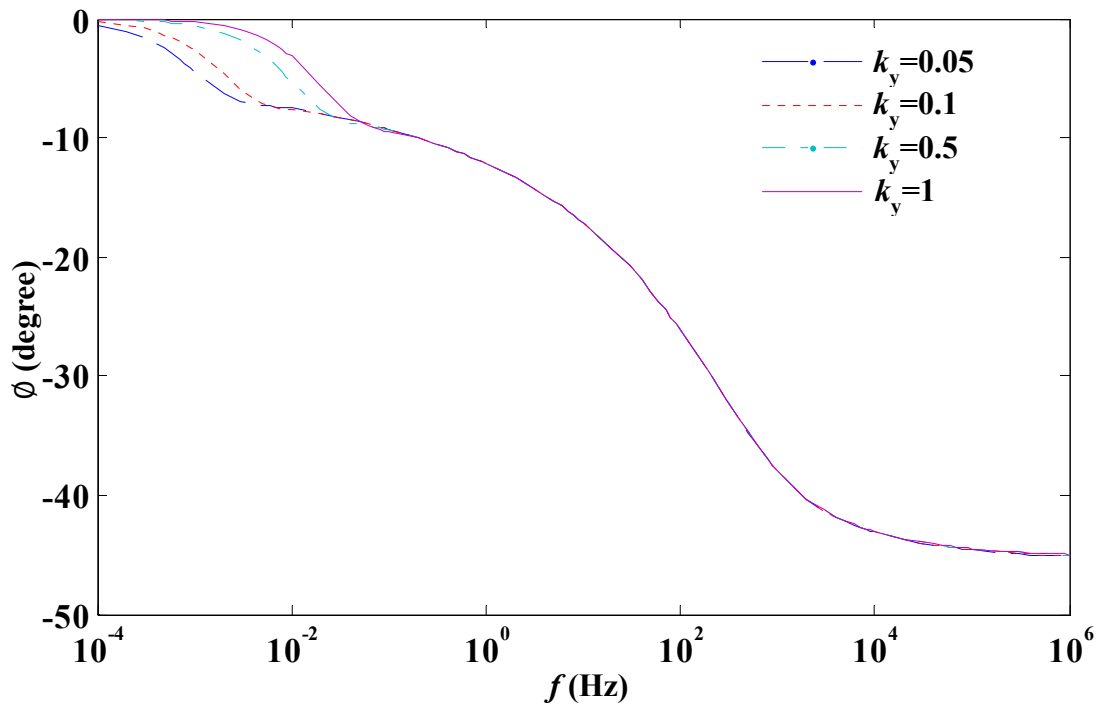
**Figure 3.8 Phase versus frequency for various values of  $l_0$  with fixed  $a_0$**   
 $a_0 = 0.0001, k_x = 5, k_y = 0.5, B_2=20$



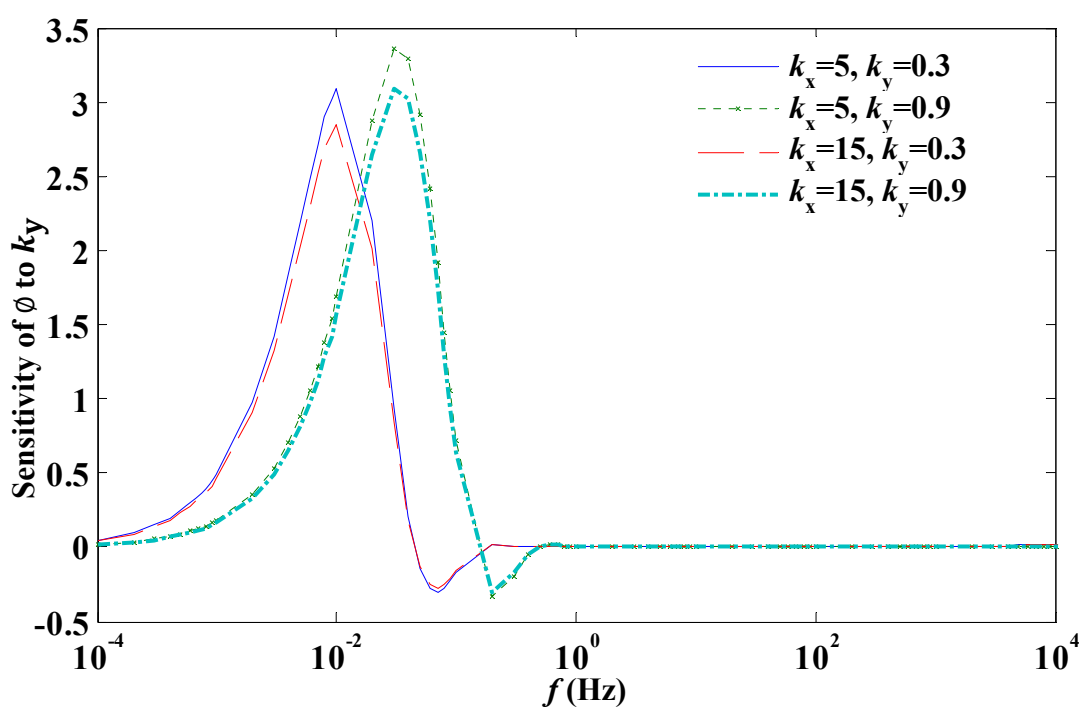
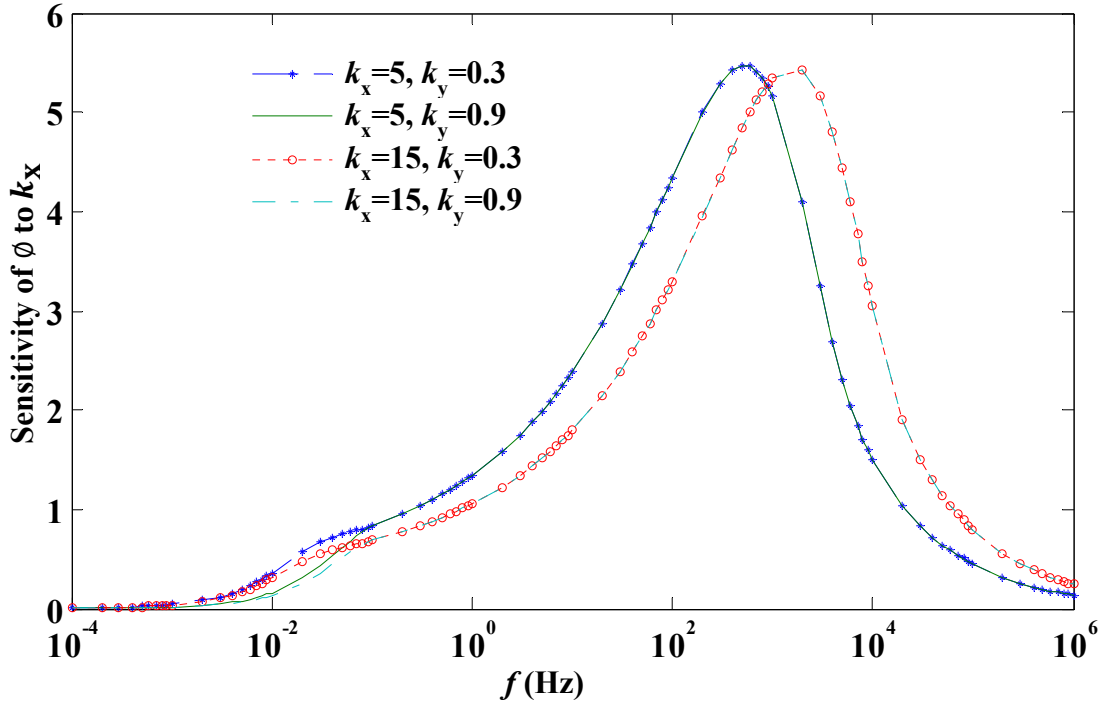
**Figure 3.9 Phase versus frequency for various values of  $a_0$  with fixed  $l_0$**   
 $l_0 = 0.003, k_x = 5, k_y = 0.5, B_2=20$



**Figure 3. 10 Phase versus frequency for various values of  $k_x$  with fixed  $k_y$ ,  
 $a_0 = 0.0001, l_0 = 0.0025, k_y = 0.5, B_2=20$**



**Figure 3. 11 Phase versus frequency for various values of  $k_y$  with fixed  $k_x$   
 $a_0 = 0.0001, l_0 = 0.0025, k_x = 5, B_2=20$**



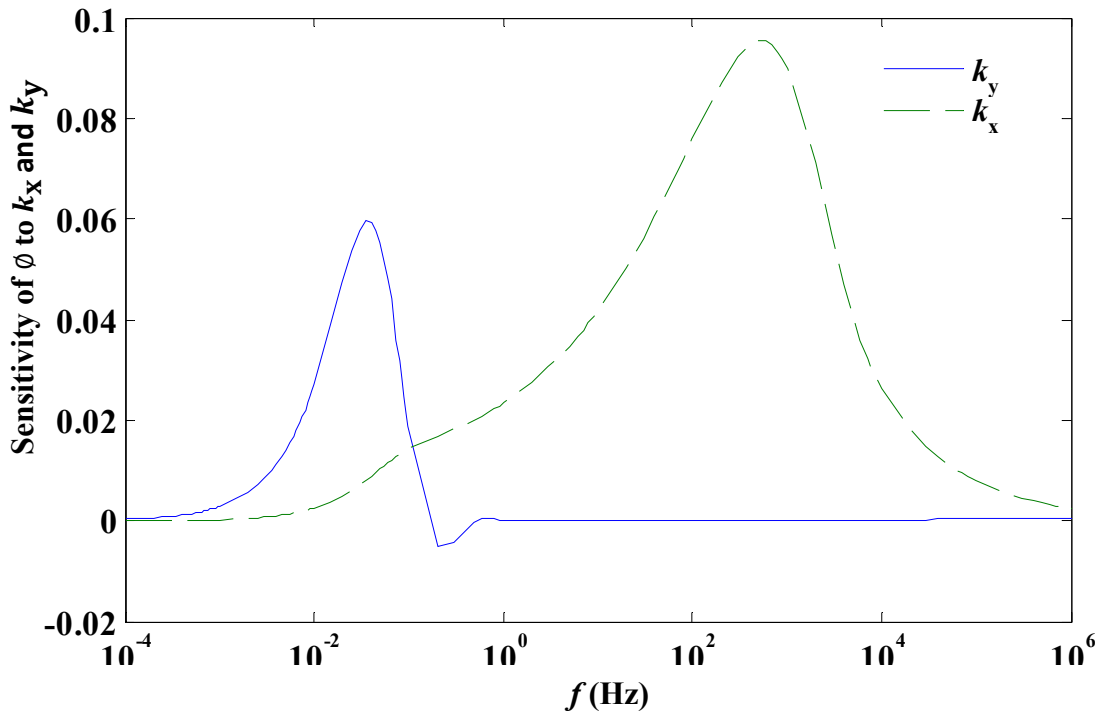


**Figure 3. 14 Sensitivity of phase to  $k_x$  and  $k_y$**   
 $l_0 = 0.003, a_0 = 0.0001, k_x = 5, k_y = 0.5, B_2=20$

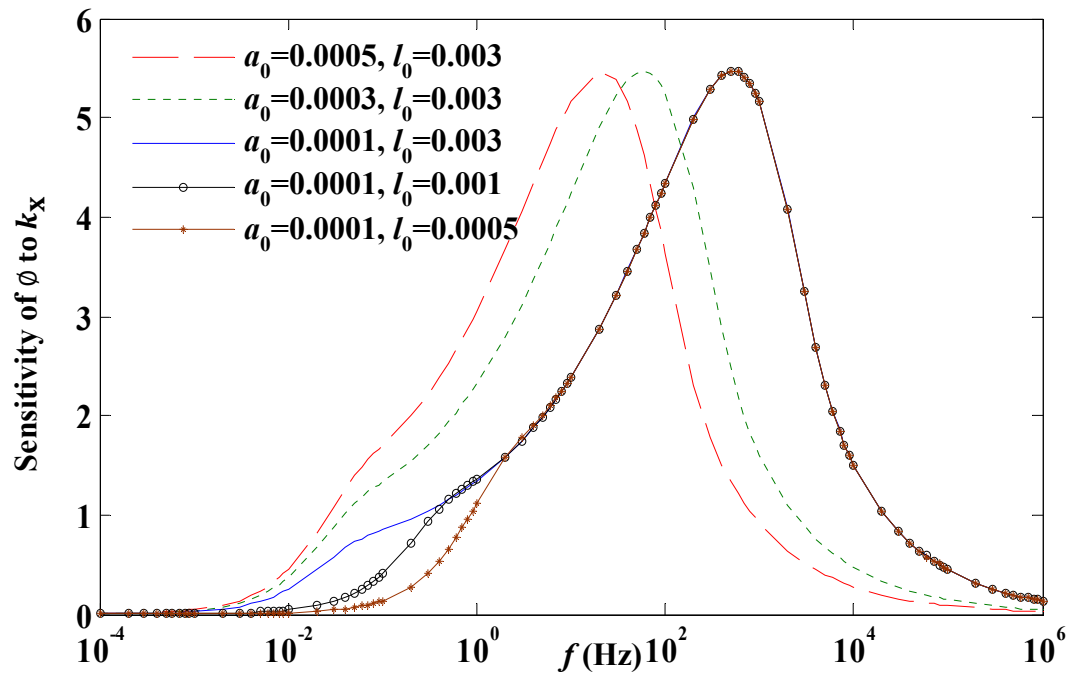


**Figure 3. 15 Sensitivity of phase to  $k_x$  for various values of  $a_0$  and  $l_0$**   
 $a_0 = 0.0001, l_0 = 0.003, k_x = 5, k_y = 0.5, B_2=20$

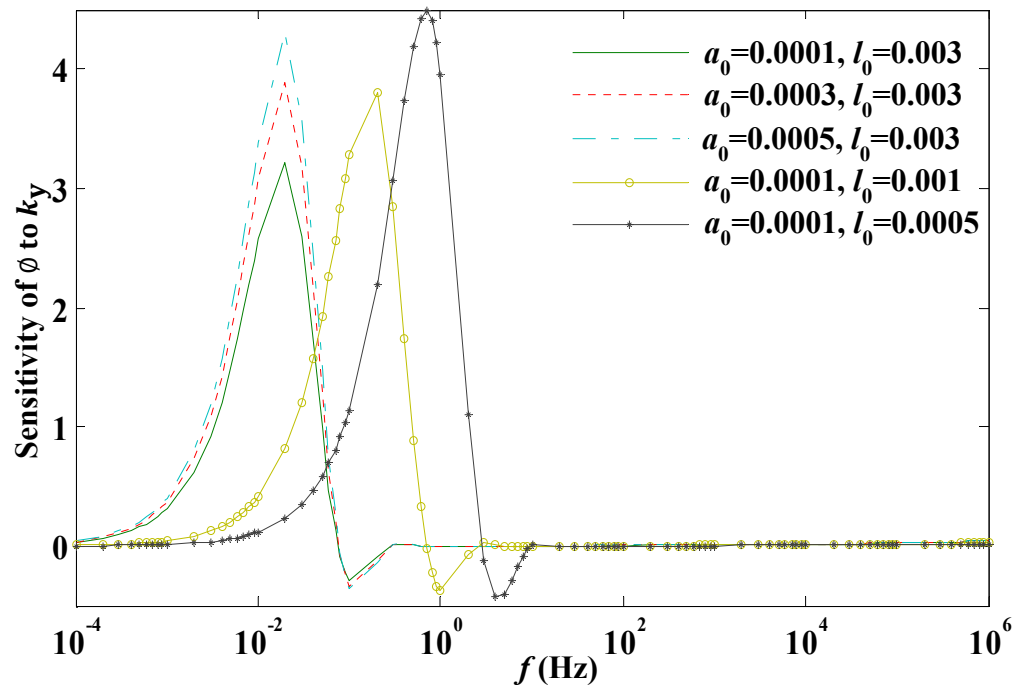


**Figure 3. 16 Sensitivity of phase to  $k_y$  for various values of  $a_0$  and  $l_0$**   
 $k_x = 5, k_y = 0.5, B_2=20$

# Chapter 4 Experiment

This chapter presents the experimental details of this work. A measurement system was designed and implemented based on the steady-periodic heating, specifically the  $3\omega$  experimental technique. Details about sample preparation, experimental equipment and system calibration are described. Experimental results are presented.

## 4.1 Experimental principle

In the  $3\omega$  measurement, a thin and narrow metal film is deposited on the surface of the sample with good thermal contact to the sample, serving as both heater and thermometer simultaneously. An alternating current (ac) at frequency  $\omega$ ,  $I(\omega)$ , passes through the metal film generating a heat flux oscillation at frequency  $2\omega$  due to Joule heating. Because of the thermoresistance effect, the electrical resistance of the wire oscillates with the surface temperature of the sample at the same frequency  $2\omega$ . Thus, the resulting voltage drop across the heating at wire at frequency  $3\omega$  contains the thermal properties information of the sample. Therefore, the direct objective of the measurement is to detect the rather weak  $3\omega$  signal.

## 4.2 Sample preparation

### 4.2.1 Sample source

Our carbon-fiber/epoxy composite samples were obtained from a local composite manufacture where carbon-fiber composite is used as the material to make natural-gas

tanks. Samples are typically plates with  $1\text{cm}^2$  area and a few millimeters thickness [1]. Our samples were cut to dimension 1inch×1inch×3mm.

#### **4.2.2 Polishing**

In order to realize good thermal contact between a sample and a continuous, thin film of metal, the  $3\omega$  measurement has a high requirement for the smoothness and flatness of the sample. The surface of carbon-fiber/epoxy samples is normally not flat or smooth enough due to the related manufacture nature of the composite material. There may even be visible pores or cracks on it. To improve the surface condition, the carbon fiber samples are individually polished on a polishing wheel with 3/1/0.3/0.05 micron alumina power. According to Carhil [56], a deposited metal film which is 5- $\mu\text{m}$ -wide requires a near mirror finish, but much wider lines of 35  $\mu\text{m}$  work fine even if the surface has a matte finish. A mirror finish is not possible with carbon-fiber/epoxy samples based on the available polishing technique in our lab. However, a close-to-matte finish is reachable, and it can be offset by depositing a rather wider metal film on the sample surface. In this work, the deposited metal line is about 100  $\mu\text{m}$ .

#### **4.2.3 Insulating layer**

Since the carbon fiber part of the sample is electrically conductive, a thin insulating layer of epoxy is brushed on the surface of the sample to electrically isolate it from the deposited metal film. Considering that epoxy is a part of the sample and the viscosity of the chosen epoxy (Embed-ItTM Low Viscosity Epoxy Kit) is as low as 65 cps, this is an economical way to insulate the deposited metal line with the sample without significantly distorting the sample properties.

In order to satisfy the smoothness requirement of the sample and minimize the effect of the new epoxy layer on sample properties, the sample has to be polished again on polishing wheels. Another layer of epoxy may need to be applied if the previous polishing work breaks the fragile epoxy layer. This procedure is repeated until a smooth boundary of epoxy is presented. Note that ultrasonic cleaning of the sample is needed before adding each epoxy layer.

#### **4.2.4 Deposition**

Platinum is chosen as the metal line because it is not easily oxidized. Shown in Fig. 4.1, a narrow, electrically conducting platinum film with dimension  $15\text{ mm} \times 0.1\text{ mm}$  is deposited directly on the surface of the sample with a mask under a sputtering target. The deposition was performed with an AJA Sputtering system (See Fig. 4.2) available at the Central Facility of Nebraska center for materials and nanoscience (NCMN) for Materials Preparation. The vacuum system can reach a base pressure about  $4 \times 10^{-8}\text{ Torr}$ . Two pads are also deposited for connecting current leads. Silver paste is used to attach the leads. An X-ray reflectivity measurement was conducted to measure the thickness of the deposited platinum film layer on one PMMA sample. Shown from Fig. 4.3, the measured platinum thickness on that particular PMMA sample is 52.2 nm.

### **4.3 Experimental setup**

Figure 4.4 shows a schematic diagram of the measurement system used in this work. In the diagram,  $R_s$  is the resistance of the platinum film deposited on the sample and  $R_1$ ,  $R_2$ ,  $R_3$  are fixed resistors, whereas  $R_2$  and  $R_3$  are large-resistance resistors. Since  $R_2$  and  $R_3$  are

large compared to  $R_s$  and  $R_1$ , most of the current flows through  $R_s$  and  $R_1$ . The SR 830 digital signal processing (DSP) lock-in amplifier (see Fig. 4.5) is the essential equipment in the experiment. An internal oscillator built in the lock-in amplifier generates a sinusoidal input current at frequency  $\omega$  passing through the platinum heater/thermometer  $R_s$ , denoted as  $U_{CD}^\omega$  in Fig. 4.4, and heating the sample up, which creates a temperature fluctuation  $\Delta T$  at frequency  $2\omega$  due to Joule heating. Suppose the current passing through one branch (shown by points DAC in Fig. 4.4) of the bridge circuit is  $I_1$ , considering the thermoresistance effect of platinum film, the voltage change across the sample  $U_s$  will be the summation of two components at frequency  $\omega$  and  $3\omega$ , respectively:

$$U_s = I_1 R_{s0}(1 + \alpha \Delta T) = U_{s0}(\omega) + \alpha U_{s0}(\omega) \Delta T(2\omega) = U_{s0}(\omega) + \Delta U_s(3\omega)$$

where  $R_{s0}$  is the resistance of platinum film at room temperature without extra heat transferred into it,  $\alpha=0.003729/(\text{unit degree of temperature})$  is platinum's temperature coefficient of resistance. The  $3\omega$  signal is significantly smaller than the  $\omega$  signal considering the magnitude of temperature coefficient value. Typically the  $\omega$  component of the signal is thousands times larger than the  $3\omega$  component. The  $3\omega$  signal embodies the information of the thermal properties of the material.

In the experiment, accurate measurement of the weak  $3\omega$  signal is the main challenge, which requires high accuracy from the electronic setup. The SR 830 digital signal processing (DSP) lock-in amplifier can be used to selectively pick up very weak signals that are varying at a specific frequency, thus removing all uncorrelated and random electrical signals that were also present. The SR 830 lock-in amplifier can be controlled and read out via electronic protocol GPIB, allowing for control via software LabVIEW. However, due to the finite dynamic reserve of the lock-in amplifier (the maximum input

voltage signal the lock-in can take is 1V), the subtraction of the  $1\omega$  voltage from the  $3\omega$  signal is necessary. Before conducting the experiment, the resistance values of resistors  $R_1$ ,  $R_2$  and  $R_3$  are adjusted to make the  $\omega$  voltage difference between points  $A$  and  $B$  minimal, where an oscilloscope can be used to aid the adjustment of the  $\omega$  voltage difference till there is no visible  $\omega$  voltage difference. This ensures that the bridge is nearly in balance, and the measured  $3\omega$  signal between points  $A$  and  $B$  has negligible effect from the small  $3\omega$  distortion of the heating current. Then the signal from points  $A$  and  $B$  are fed into the differential input of the lock-in amplifier. In addition, the lock-in amplifier takes the third harmonic of the input signal as a reference signal. The lock-in amplifier gives the phase shift and amplitude of the  $3\omega$  voltage variation compared to the reference signal which is also fluctuating at frequency  $3\omega$ .

There are two types of experimental setups for  $3\omega$  measurement in literature. One is the setup we discussed above which contains a Wheatston bridge (shorted for “BriC” in below); another type of setup includes two operational amplifiers and a multiplying data to analog converter (shorted for “AmpC” in below). In this work, significant effort has been given to the comparison of these two kinds of setups by “normal resistor measurement” (NRM will be discussed in detailed in Section 4.4). It was concluded that the cumbersome nature of the AmpC circuit distorts the phase and amplitude of the observed signals. All the results shown in this work are collected by the BriC method.

Figure 4.6 shows a schematic diagram of the AmpC setup. In the AmpC setup, the subtraction of the  $1\omega$  voltage from the  $3\omega$  single is also necessary. The output voltage across the regular resistor at frequency  $\omega$  can be adjusted to be close to the voltage across the sample at frequency  $\omega$  with a 12 bit multiplying digital to analog converter (AD

7541AKNZ) whose gain can be varied from 0 to 1 by computer control of 12 TTL levels. Then the  $1\omega$  component within the  $3\omega$  signal is reduced by the differential input of the lock-in amplifier to an acceptable level. The phase lag between the  $3\omega$  component of the signal across the sample and the reference signal at  $3\omega$  is then monitored by the lock-in amplifier. Again, the AmpC method was built, studied but rejected in favor of the BriC method.

## 4.4 System Calibration

In the  $3\omega$  experiment, the phase shift of the voltage variation over the sensor due to the temperature response in the sample is the desired measured data used for curve fitting. However, the measurement result will inevitably include some phase shift induced by all the wiring including resistors and capacitors in the system. The system phase shift is calibrated by normal resistor measurements (shorted for “NRM” in below), where the sample is replaced by a normal resistor before proceeding to the  $3\omega$  measurement.

Considering the effect of the cables in the electrical circuit, the schematic diagram is plotted in Fig. 4.7. Figures 4.8 and 4.9 show the amplitude and phase data from the NRM measurement. It can be seen that the phase results differ much from zero, which reveals that the effects of capacitances and resistance from the cables between points A and B in the circuit have to be considered.

The voltage  $U_{AB}^\omega$  (the subscript  $\omega$  is a reminder that voltage  $U_{AB}$  is at frequency  $\omega$ , since this is NRM measurement) between points A and B can be expressed as

$$\frac{U_{AB}^\omega}{U_{CD}^\omega} = \frac{X_A}{X_A + R_a} - \frac{X_B}{X_B + R_b} \quad (4.1)$$

where  $X_{A,B}$  are the combined impedances of  $R_{a,b}$ , and  $X_{a,b}, X_{a,b}$  are the impedances of the cables,  $U_{CD}^\omega$  is the voltage applied between points C and D. That is

$$X_{A,B} = \frac{R_{s,b} X_{a,b}}{R_{s,b} + X_{a,b}}, \quad X_{a,b} = \frac{1}{i\omega C_{a,b}}, \quad (4.2)$$

where  $i = \sqrt{-1}$ .

Substituting Eq. (4.2) into Eq. (4.1), we have

$$\frac{U_{AB}^\omega}{U_{CD}^\omega} = \frac{R + iI}{DE} \quad (4.3)$$

with

$$R = \left( \frac{\frac{R_a}{R_A} \frac{R_b}{R_B} \frac{\omega C_a R_a}{R_A} \frac{\omega C_b R_b}{R_B}}{\frac{R_a}{R_A} \frac{R_b}{R_B}} + \frac{\frac{R_a}{R_A}}{1 + \frac{R_a}{R_A}} - \frac{\frac{R_b}{R_B}}{1 + \frac{R_b}{R_B}} \right) \left( 1 - \frac{\omega C_a R_a}{R_A} \frac{\omega C_b R_b}{R_B} \right) \\ + \left( \frac{\frac{R_a}{R_A} \frac{\omega C_b R_b}{R_B} - \frac{\omega C_b R_b}{R_B} \frac{\omega C_a R_a}{R_A}}{1 + \frac{R_a}{R_A} \frac{R_b}{R_B}} \right) \left( \frac{\omega C_a R_a}{R_A} + \frac{\omega C_b R_b}{R_B} \right) \quad (4.4)$$

$$I = \left( \frac{\frac{R_a}{R_A} \frac{\omega C_b R_b}{R_B} - \frac{\omega C_b R_b}{R_B} \frac{\omega C_a R_a}{R_A}}{1 + \frac{R_a}{R_A} \frac{R_b}{R_B}} \right) \left( 1 - \frac{\omega C_a R_a}{R_A} \frac{\omega C_b R_b}{R_B} \right) \\ - \left( \frac{\frac{R_a}{R_A} \frac{R_b}{R_B} \frac{\omega C_a R_a}{R_A} \frac{\omega C_b R_b}{R_B}}{\frac{R_a}{R_A} \frac{R_b}{R_B}} + \frac{\frac{R_a}{R_A}}{1 + \frac{R_a}{R_A}} - \frac{\frac{R_b}{R_B}}{1 + \frac{R_b}{R_B}} \right) \left( \frac{\omega C_a R_a}{R_A} + \frac{\omega C_b R_b}{R_B} \right) \quad (4.5)$$

$$DE = \left(1 - \frac{\omega C_a R_a}{R_A} \frac{\omega C_b R_b}{R_B}\right)^2 + \left(\frac{\omega C_a R_a}{R_A} + \frac{\omega C_b R_b}{R_B}\right)^2 \quad (4.6)$$

Thus the phase and amplitude of  $U_{AB}$  is

$$\phi_{U_{AB}} = \text{atan} \frac{I}{R} \quad (4.7)$$

$$A_{U_{AB}} = \frac{U_{CD}^{\omega} \sqrt{R^2 + I^2}}{DE} \quad (4.8)$$

Figure 4.10 shows the result of using Eq. (4.7) and (4.8) to curve fit the phase and amplitude data collected from experiments, where the maximum percent difference between measured and model calculated data is 4.50% among all the used data points. The total capacitance of each cable used in the measurement is obtained as 71.41pF. The fact that the model fits with experimental results well also improves our confidence of the suitability of the model we used.

## 4.5 Impedance analysis model

From the theoretical model, the amplitude and phase solution of temperature are obtained. From the measurement, the lock-in amplifier gives the amplitude and phase data of the voltage  $U_{AB}^{3\omega}$ . For parameter estimation, the unknown thermal parameters were determined by fitting the model calculated solution to a set of experimental data. Therefore, the voltage data need to be converted to temperature data so that the model

calculated temperature solution and measured temperature data can be compared. An impedance analysis model is built to convert the voltage data  $U_{AB}^{3\omega}$  to temperature data.

As shown in Fig. 4.7, a signal at frequency  $\omega$  with voltage  $U_{CD}^\omega$  supplied by the lock-in amplifier is used as the power source to drive the circuit. Because of the thermal resistance effect, the voltage across the platinum is

$$U_S = I_1(\omega) R_a (1 + \alpha \Delta T(2\omega))$$

where  $\alpha$  is the temperature coefficient of platinum,  $I_1(\omega)$  is the current flowing through the sample at frequency  $\omega$  induced by the power source  $U_{CD}^\omega$ ,  $R_a$  is the resistance of the platinum film at room temperature without extra heating. It can be seen  $U_s$  is the combination of two components, which are at frequency  $\omega$  and  $3\omega$ , respectively:

$$U_S^\omega = I_1(\omega) R_a$$

$$U_S^{3\omega} = \alpha I_1(\omega) R_a \Delta T(2\omega)$$

That is, there is another current at frequency  $3\omega$ ,  $I(3\omega)$ , flowing around the circuit.

Referring to Fig. 4.7, based on the circuit structure, the following equations can be written:

$$I_1(\omega)(R_A + X_A(\omega)) = I_2(\omega)(R_B + X_B(\omega)) = U_{CD}^\omega$$

$$U_{AB}^{3\omega} = I(3\omega)R_A + I(3\omega)R_B$$

$$U_{AB}^{3\omega} = -I(3\omega)X_B(3\omega) + U_S^{3\omega}$$

where  $I_2(\omega)$  is the current flowing through another branch of the circuit at frequency  $\omega$  induced by the power source  $U_{CD}^\omega$ ,

$$X_B(3\omega) = \frac{R_b X_b(3\omega)}{R_b + X_b}$$

$$X_b(3\omega) = \frac{1}{i3\omega C_b}$$

Therefore,

$$U_S^{3\omega} = U_{AB}^{3\omega} \left(1 + \frac{X_B(3\omega)}{R_A + R_B}\right) \quad (4.9)$$

Also we have:

$$U_S^{3\omega} = \alpha \Delta T(2\omega) U_{CD}^\omega \frac{X_A(\omega)}{R_A + X_A(\omega)} \quad (4.10)$$

Combine Eq. (4.9) and (4.10),

$$\Delta T(2\omega) = \frac{1}{\alpha} \frac{U_{AB}^{3\omega}}{U_{CD}^\omega} \left(1 + \frac{X_B(3\omega)}{R_A + R_B}\right) \frac{R_A + X_A(\omega)}{X_A(\omega)} \quad (4.11)$$

The amplitude and phase of  $U_{AB}^{3\omega}$  can be obtained from measurement noted as  $A_{U_{AB}^{3\omega}}$  and

and  $\phi_{U_{AB}^{3\omega}}$ . That is,

$$U_{AB}^{3\omega} = A_{U_{AB}^{3\omega}} \exp(i\phi_{U_{AB}^{3\omega}}) \quad (4.12)$$

Substitute  $X_a = \frac{1}{i\omega C_a}$  and  $X_A = \frac{R_a X_a}{R_a + X_a}$  into Eq. (4.11) and (4.12),  $\Delta T(2\omega)$  can be expressed by

$$\Delta T(2\omega) = \frac{1}{\alpha} \frac{A_{U_{AB}^{3\omega}}}{U_{CD}^\omega} \frac{(R_1 R_2 - I_1 I_2) + i(I_1 R_2 + I_2 R_1)}{a(1 + 9q^2)} \quad (4.13)$$

where  $I_1 = \sin(\phi_{U_{AB}^{3\omega}})$ ,  $R_1 = \cos(\phi_{U_{AB}^{3\omega}})$ ,  $I_2 = p(1 + m + 9q^2) - 3qm(1 + a)$ ,

$$R_2 = (1 + a)(1 + m + 9q^2) + 3qm, a = \frac{R_a}{R_A}, m = \frac{R_b}{R_A + R_B}, p, q = \omega C_{a,b} R_{a,b}$$

Then the phase  $\phi_{\Delta T}^{2\omega}$  and amplitude  $A_{\Delta T}^{2\omega}$  of  $\Delta T(2\omega)$  are:

$$\emptyset_{\Delta T}^{2\omega} = \arctan \frac{I_1 R_2 + I_2 R_1}{R_1 R_2 - I_1 I_2} \quad (4.14)$$

$$A_{\Delta T}^{2\omega} = \frac{1}{\alpha} \frac{A_{U_{AB}^{3\omega}}}{U^\omega} \frac{\sqrt{(I_1 R_2 + I_2 R_1)^2 + (R_1 R_2 - I_1 I_2)^2}}{a(1 + 9q^2)} \quad (4.15)$$

Thus, equations (4.14) and (4.15) will be used to convert the data directly collected from experiments related to voltage  $U_{AB}^{3\omega}$  to those related to temperature  $\Delta T(2\omega)$ .

## 4.6 Experimental results

This section presents the obtained experimental results including:

- 1) the amplitude and phase data of  $U_{AB}^{3\omega}$  collected directly from the experiment,
- 2) the converted amplitude and phase data of temperature  $\Delta T(2\omega)$  using the impedance analysis model discussed in the last section.

Before proceeding to our target sample carbon-fiber/epoxy composite, experiments were first carried out with PMMA samples to verify the measurement system since the thermal properties of PMMA material are known. Note data only is given in this chapter. Data analysis and thermal property estimation results will be presented in Chapter 5.

### 4.6.1 Result for PMMA samples

Experiments were conducted on twenty-one PMMA samples in total, out of which the results from five samples are considered to be typical. Their sample IDs are P#6, P#8,

P#9, P#10 and P#14. Results from the first two samples are presented and discussed in this section. See Appendix A for details on Sample P#9, P#10 and P#14. Results from sixteen samples were considered not acceptable and discarded. The failure for the sixteen samples can be attributed to a few reasons briefly: 1) Platinum film that grows on a sample is not continuous enough thus the film is not sensitive enough to the weak  $3\omega$  out of the sample; 2) Temperature increase in a sample is so high that deformation of PMMA samples occur; 3) Temperature increase in a sample is too low for the sensor to detect the weak  $3\omega$  signal. The previous reasons will be discussed below as well.

**Sample P#6** Figures 4.11-4.14 show the amplitude and phase data of  $U_{AB}^{3\omega}$  collected from Exp. #1 and #2 where different resistor-combinations of  $R_A$ ,  $R_B$  and  $R_b$  (See Fig. BCw/c for detail of experimental setup) are applied of PMMA sample P#6 whose electrical resistance is  $315 \Omega$  at room temperature. For each case with fixed resistor combination, three experiments were carried out where supplying signal  $U_{CD}^\omega$  with different magnitude of voltage ( $U_{CD} = 5$  V, 3.5 V and 2 V) were input. In each experiment, amplitude and phase data are collected in frequency range [0.001 Hz-10000 Hz] at 54 discrete frequency points while all the other parameters are fixed. It takes about 30 hours to run through each experiment. Altogether experimental results from six experiments for sample P#6 are presented.

Regarding the three experiments conducted under fixed resistor combination (Exp. #1 or #2), it can be seen from Fig. 4.11 that the amplitude data of  $U_{AB}^{3\omega}$  are larger from those experiments which have input signal with relatively larger voltage magnitude. This physically makes sense. As for every two experiments conducted under input signals with the same magnitude of voltage, Figure A1 shows that the amplitude result of  $U_{AB}^{3\omega}$

collected from Exp. #2 are larger than those from Exp. #1. This is because the resistance value  $R_A$  in Exp. #2 is smaller, which makes the voltage acrossed the platinum  $R_a$  larger since the two resistors are in series in the circuit.

To have a better observation of the phase data obtained under different voltage magnitude of input signal, Figure 4.13 plots the phase data of  $U_{AB}^{3\omega}$  at  $U_{CD}=5$  V and 3.5 V, and Figure 4.14 solely plots the phase data at  $U_{CD}=5$  V. It can be seen that the curves of the data are smoother under experiments with larger magnitude of input signals. Both the amplitude and phase data for  $U_{CD}=2$  V are the least smoothest, and the phase data are considerably noisy. This is not surprising since the weak  $3\omega$  signal due to the weak temperature response caused by the small input signal could be not strong enough for the lock-in amplifier to be able to detect. Based on this fact, it was decided that experiment on  $U_{CD}=2$  V would not be conducted with other samples.

Shown from Figs. 4.11-4.14, both the amplitude and phase data curves are less smooth as frequencies are extremely small or big, while the data present the best smoothness in medium frequency range [0.01 Hz-30 Hz] containing 37 frequency points. This is not surprising since detecting extremely small and big frequency signals are generally challenging. It takes longer time period for a lock-in amplifier to collect data at low frequencies. Typically the time needed is ten times the period of the supplying signal. For example, at frequency 0.001Hz, about three hours will be needed. In such a long period a lot of noisy signal existing in the environment may be randomly picked up. At high frequency, two reasons can be stated regarding the poor-quality data: 1) it is harder for the lock-in amplifier itself to detect phase shift of high frequency signals; 2) temperature rise in the sample at high frequency becomes smaller which makes the  $3\omega$  signal weaker

for the lock-in amplifier to catch. Fortunately, by the sensitivity analysis carried out in Chapter 3, experimental data in the medium frequency range [0.01 Hz-1000 Hz] should be sufficient for thermal parameter estimation.

Figures 4.15-4.16 plot the amplitude and phase data of temperature  $\Delta T(2\omega)$  converted from  $U_{AB}^{3\omega}$  using the impedance analysis model in frequency range [0.001 Hz-30 Hz] under  $U_{CD}=5V$  from Exp. #1 and #2. The data in frequency range [0.01 Hz-30 Hz] will be used for estimating the thermal parameters of sample P#6 in Chapter 5 since they are considered to be the best data obtained from this sample.

Comparing to the data obtained from sample P#8, #10 and #14, the data from sample P#6 are less smooth. It can be seen from Fig. A3 that the temperature at the first frequency point 0.001 Hz where the measurement starts is close to be 9 K. Under such a high temperature, deformation of PMMA sample may occur. Thus the sensitivity of platinum film as a thermometer to the temperature response in the sample may reduce along with that to the related  $3\omega$  signal.

Based on the two facts discussed above: 1) the data obtained at lower frequency range [0.001 Hz, 0.01 Hz] are rather noisy; 2) the temperature rise at lower frequency is relatively higher, which may cause PMMA sample deformation, it was decided that data at frequency range [0.001 Hz, 0.01 Hz] would not be collected with other samples.

**Sample P#8** Figures 4.17-4.20 show the samplitude and phase data of  $U_{AB}^{3\omega}$  collected from Exp. #1, #2 and #3 of PMMA sample P#8 whose electrical resistance is  $225 \Omega$  at room temperature. It can be seen the results from Exp. #1 and #2 under  $U_{CD}=5V$  present fairly good smoothness and the phase result from the two experiments agree very well. In comparison, the result from Exp. #1 and #2 at  $U_{CD}=3.5 V$  are relatively noisy, which

should be due to the weak supplying voltage across the platinum film. For the similar reason, the data from Exp. #3 at  $U_{CD}=5$  V do not seem as good either since due to the rather big resistance of  $R_A$  ( $R_A=175\ \Omega$ ).

Comparing the amplitude and phase data from sample P#8 and those from sample P#6, the data from P#8 present better smoothness, which justifies the reasonings related to PMMA sample deformation. The proper resistance value of  $R_A$  ( $R_A=30\ \Omega/50\ \Omega$  for Exp. #1/#2) makes the platinum film occupy the right amount of voltage which is big enough for lock-in amplifier to detect the  $3\omega$  signal and also not too big to cause deformation of the PMMA sample in which case the sensitivity of platinum film as sensor would be reduced.

Figures 4.21-4.22 plot the amplitude and phase data of temperature  $\Delta T(2\omega)$  converted from  $U_{AB}^{3\omega}$  using the impedance analysis model in frequency range [0.01 Hz-30 Hz] under  $U_{CD}=5$  V from Exp. #1 and #2. These data will be used for estimating the thermal properties of sample P#8 in Chapter 5 and it turns out the obtained thermal property values from curvefitting these data and theoretical model calculated solution agree with handbook value very well.

**Conclusion** The result from three samples P#8, P#10 and P#14 show great smoothness and consistency. They will be used for parameter estimation in Chapter 5. It is observed that the magnitude of the voltage drop across the platinum film significantly affects the quality of the experimental data. If the voltage is too large, the large temperature rise may cause PMMA sample deformation and reduce the sensitivity of the film on  $3\omega$  signal; if the voltage is too small, the  $3\omega$  signal is too weak for lock-in amplifier to detect. The voltage magnitude across the platinum film can be manipulated by adjusting the

magnitude of the input supplying signal  $U_{CD}$  and the resistance value of  $R_A$  in the circuit. Based on the amplitude data of temperature  $\Delta T(2\omega)$  converted from  $U_{AB}^{3\omega}$  using the impedance analysis model, it is concluded that a temperature rise between 1.5 K and 3 K is good for the measurement with PMMA samples.

#### 4.6.2 Result for carbon fiber samples

Experiments were conducted on twenty-five carbon-fiber/epoxy composite samples in total, out of which the results from four samples are considered to be acceptable. Their sample IDs are C#7, C#8, C#13 and C#16 whose electrical resistances are 342 Ω, 385 Ω, 381 Ω and 424 Ω at room temperature, respectively. The poor contact between platinum film and the samples due to the roughness of the carbon-fiber surface may be the main reason that causes the failure of many samples. Results from sample C#7 are presented and discussed in this section. See Appendix B for details on Sample C#8, #13 and #16.

For each two sets of experiments Exp. #1 and #2 where different resistance-combinations of  $R_A$ ,  $R_B$  and  $R_b$  are applied. In each experiment, amplitude and phase data are collected in frequency sample, range [0.01 Hz-1000 Hz] at 46 discrete frequency points while all the other parameters are fixed. For each case with fixed resistance-combination, two measurements were carried out where supplying signal  $U_{CD}^{\omega}$  with different magnitude of voltage ( $U_{CD}=5$  V, 3.5 V) were input. Altogether experimental results from four experiments for each sample are presented. Figures 4.23-4.24 show the samplitude and phase data of  $U_{AB}^{3\omega}$  collected from the measurements with carbon fiber sample C#7. Looking at the data from each sample, the results from Exp. #1 and #2 under  $U_{CD}=5$  V are fairly smooth, compared to the data from  $U_{CD}=3.5$  V, and the phase result from all the four experiments basically agree very well.

Figure 4.25-4.26 present the amplitude and phase data of temperature  $\Delta T(2\omega)$  converted from  $U_{AB}^{3\omega}$  from Exp. #1 and #2 at  $U_{CD}=5$  V of the sample C#7. It can be seen the maximum magnitude of temperature rise is larger than 4 K and the data still look good, and thereby it is reasoned that there is no need to worry about the deformation of carbon-fiber samples due to high temperature. This makes sense since the carbon-fiber/epoxy composite is less prone to thermal expansion than the PMMA material. That may also explain the fact that smooth data in a relatively wider frequency range [0.01 Hz, 1000 Hz] can be obtained from carbon-fiber samples, compared the narrower frequency range with PMMA samples. In chapter 5, the amplitude and phase data of temperature  $\Delta T(2\omega)$  will be used for paramater estimation to determine thermal properties.

## 4.7 Chapter Summary

In this chapter, the carbon-fiber/epoxy composite sample preparation procedure is described. The key point is to polish the sample well and apply a thin layer of epoxy for electrical isolation before depositing the platinum film. The thickness of deposited platinum is about 52 nanometers based on X-ray reflectively measurement.

The main challenge of the experiment is to detect the weak  $3\omega$  signal deeply buried in a  $\omega$  signal, which is overcome by employing a Wheatstone bridge circuit. It is observed that all the wirings in the circuit including resistance and capacitance introduce an extra and undesired phase shift, so a series of “normal resistor measurements” are carried out to calibrate the capacitance and resistance. The cable capacitance values are used in an

impedance analysis model to convert the measured amplitude and phase of voltage  $U_{AB}^{3\omega}$  to the amplitude and phase of temperature  $\Delta T(2\omega)$ .

Experiments were conducted on twenty-one PMMA samples, out of which the results from sixteen samples were considered not acceptable and discarded. The failure for the sixteen samples can be attributed to a few reasons: 1) Platinum film that grows on a sample is not continuous enough thus the film is not sensitive enough to the weak  $3\omega$  signal; 2) Temperature increase in a sample is so high that deformation of PMMA samples occurs. 3) Temperature increase in a sample is too low for the sensor to detect the weak  $3\omega$  signal. It was observed that a temperature rise between 1.5 K and 3 K is good for the measurement with PMMA samples. Experiments were conducted on twenty-five carbon-fiber composite samples, out of which the results from four samples are considered to be acceptable. The poor contact between platinum film and the samples due to the roughness of the carbon-fiber surface may be the main reason that causes the failure of many samples.

The experimental amplitude and phase data of  $U_{AB}^{3\omega}$  and the corresponding converted amplitude and phase data of temperature  $\Delta T(2\omega)$  based on the impedance analysis model from five PMMA samples and four carbon-fiber epoxy samples are presented and discussed.

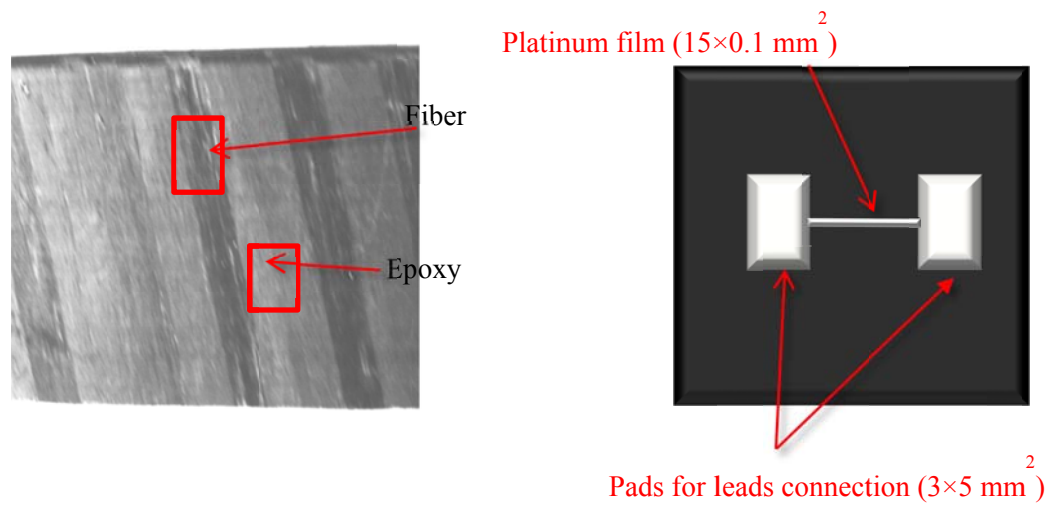


**Figure 4. 1** A photographic picture of the carbon-fiber composite sample and a schematic picture of a platinum film



**Figure 4. 2** The AJA sputter system used for deposition

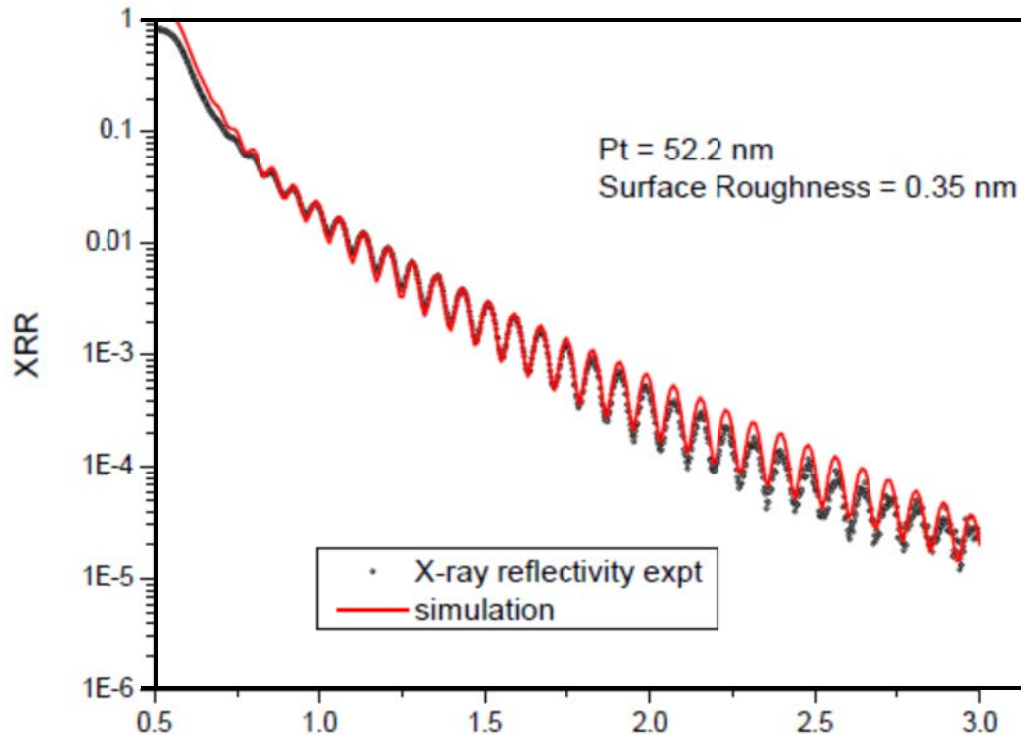


**Figure 4. 3 Result from X-ray reflectively measurement of platinum film on one PMMA sample. Thickness is estimated from curvefit of data shown.**

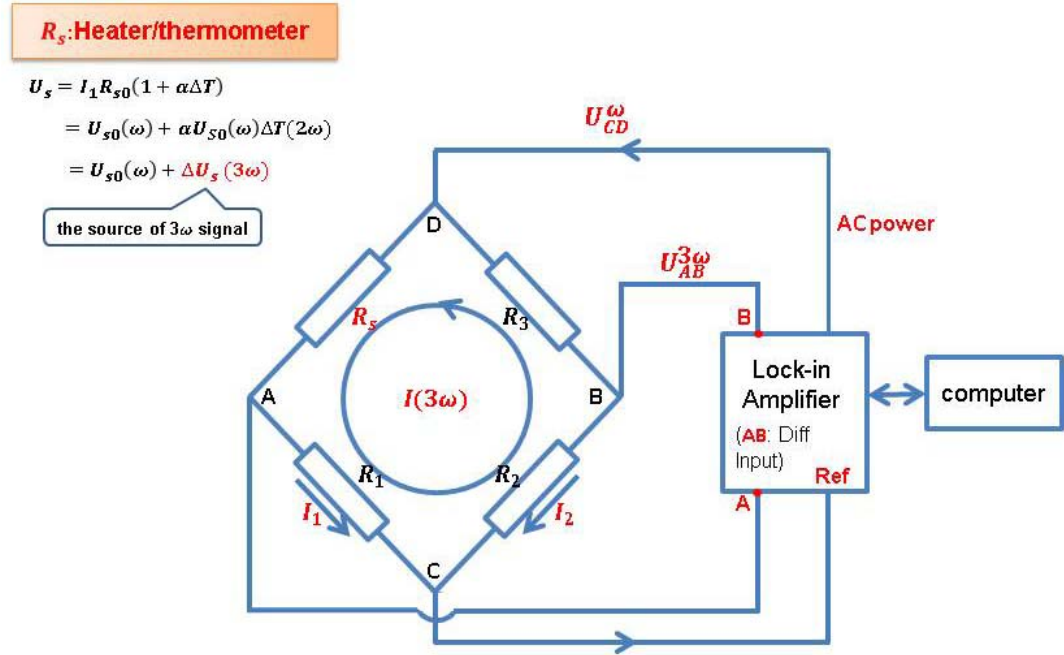


Figure 4. 4 Schematic of the  $3\omega$  experimental setup with the Wheatston bridge using a lock-in amplifier as the ac power source



Figure 4. 5 Photographic picture of SR 830 Lock-in amplifier

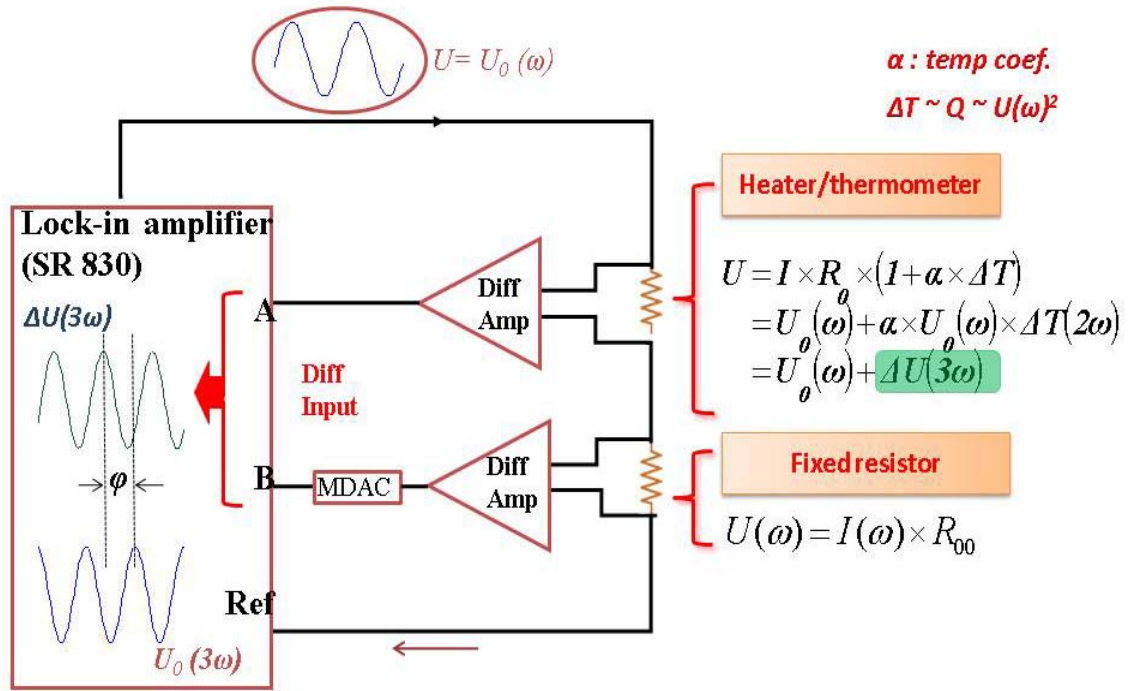
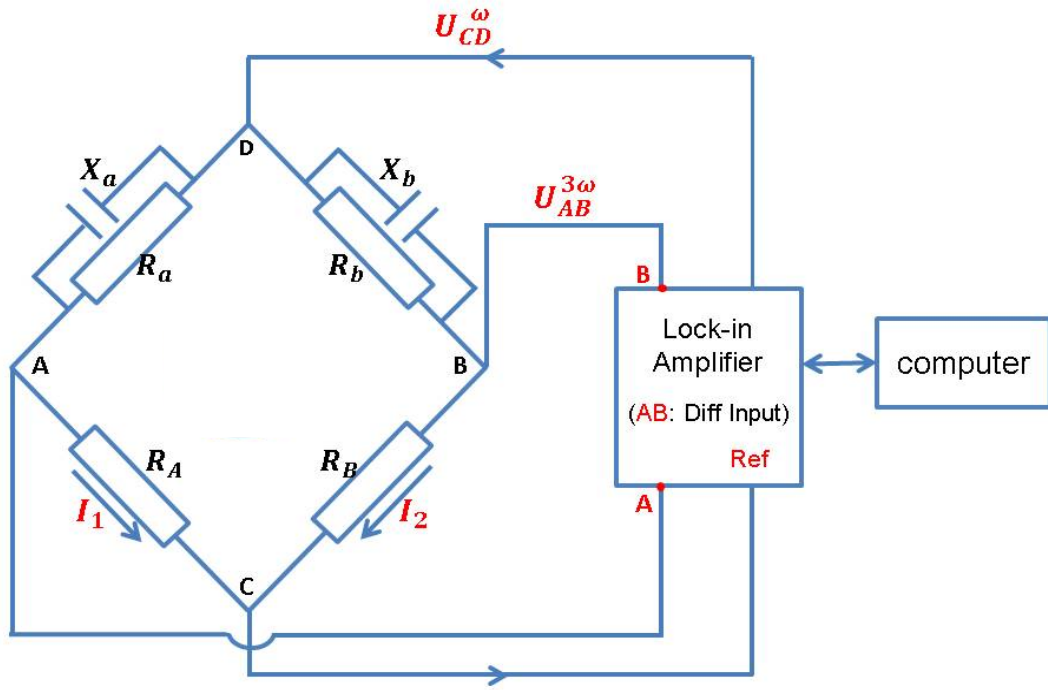
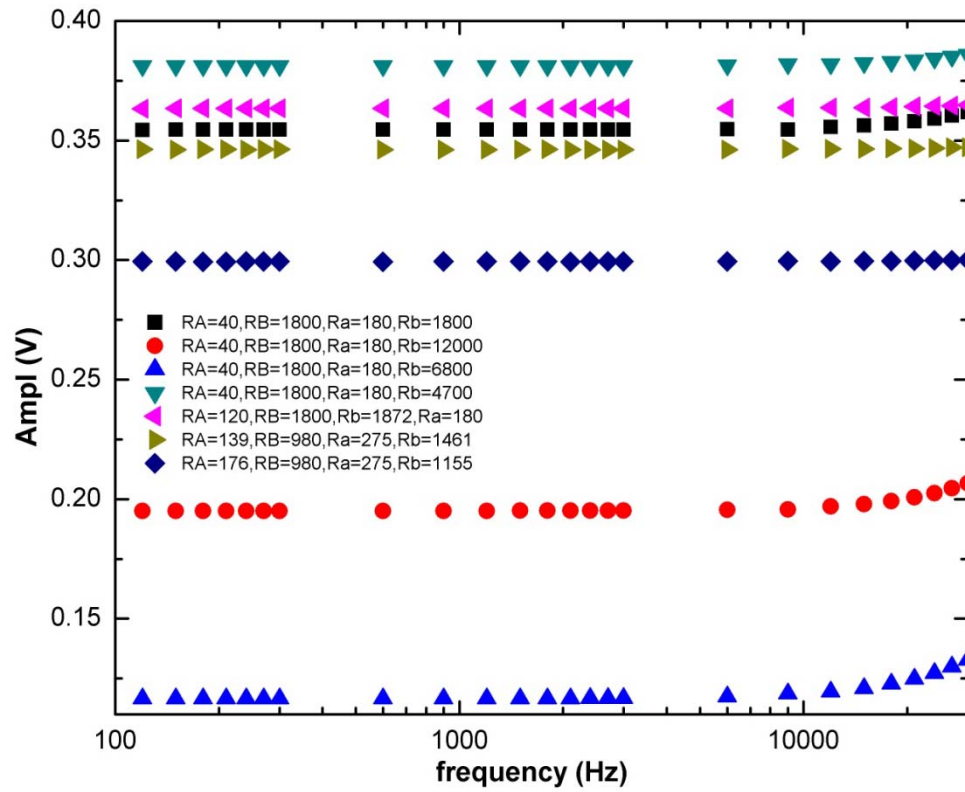


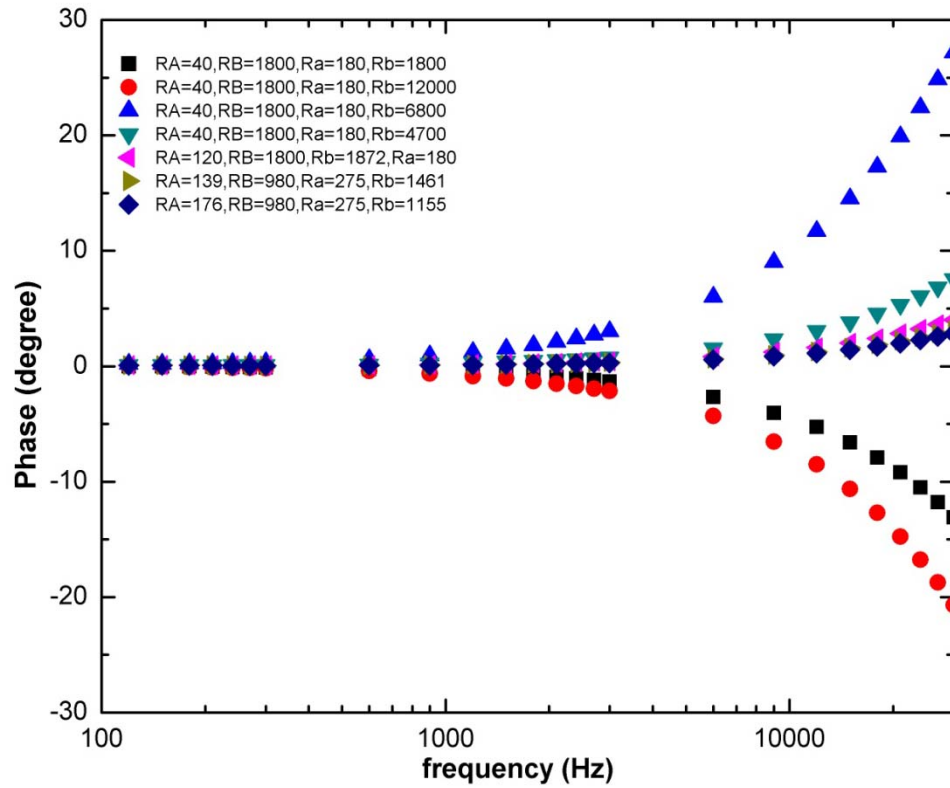
Figure 4. 6 Schematic diagram of the amplifier circuit. This method was studies but not utilized for reporting results.



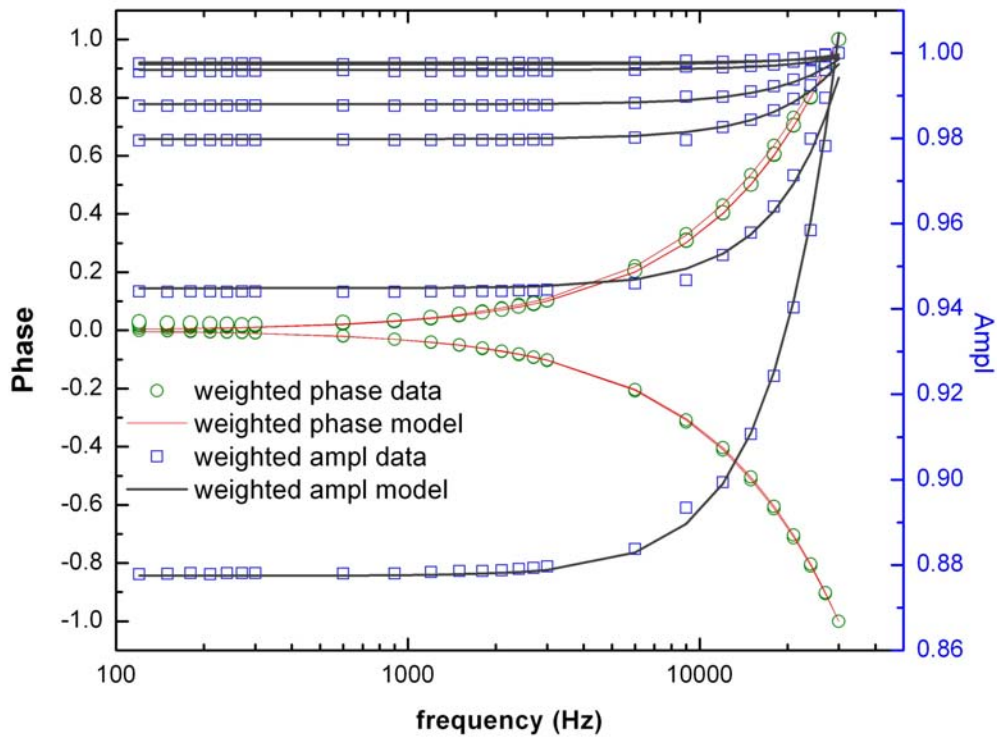
**Figure 4. 7 Schematic experimental setup considering the effect of cable capacitance in the circuit**



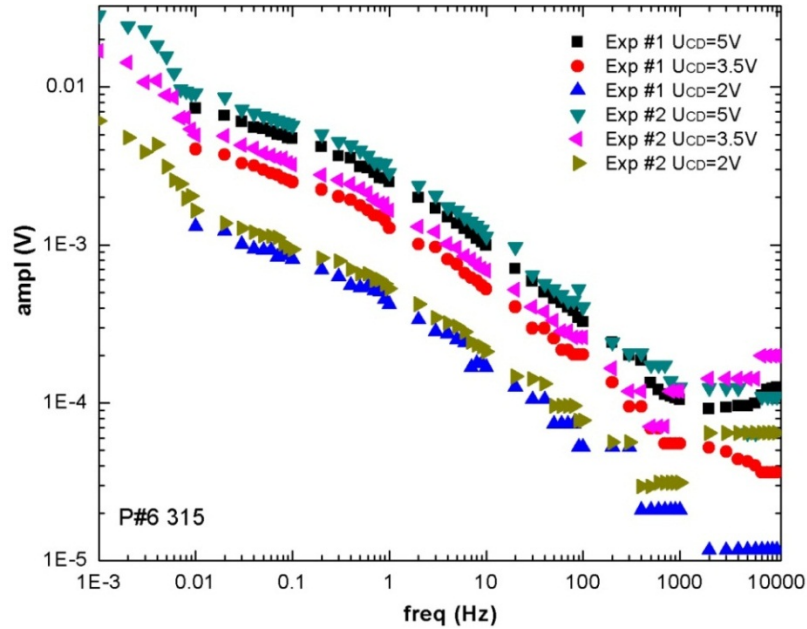
**Figure 4.8 Amplitude results from NRM measurement with varied resistance combination**



**Figure 4. 9 Phase results from NRM measurement with varied resistance combination**



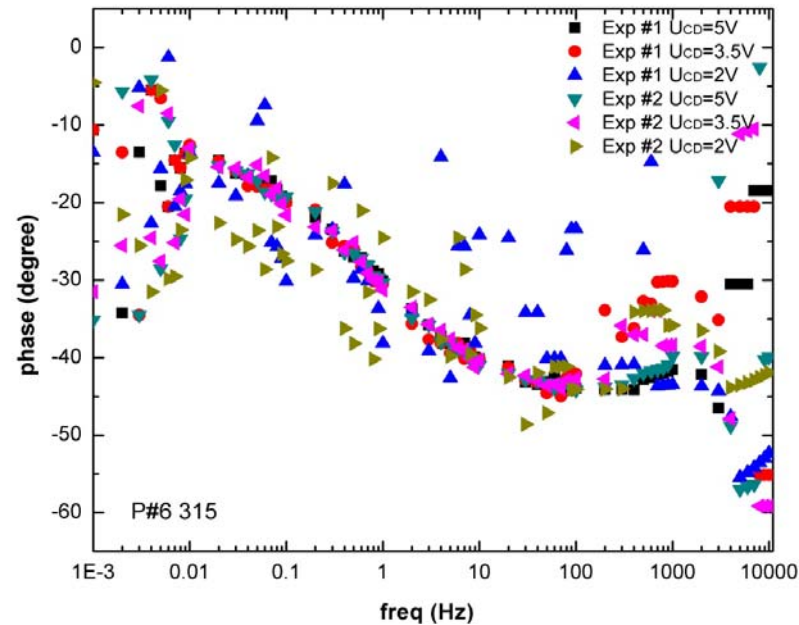
**Figure 4. 10 Curve fit of experimental amplitude and phase data from NRM experiments and Eq. (4.7)-(4.8) to estimate the capacitance of cables**



**Figure 4. 11 Amplitude of  $U_{AB}^{3\omega}$  collected from measurement**

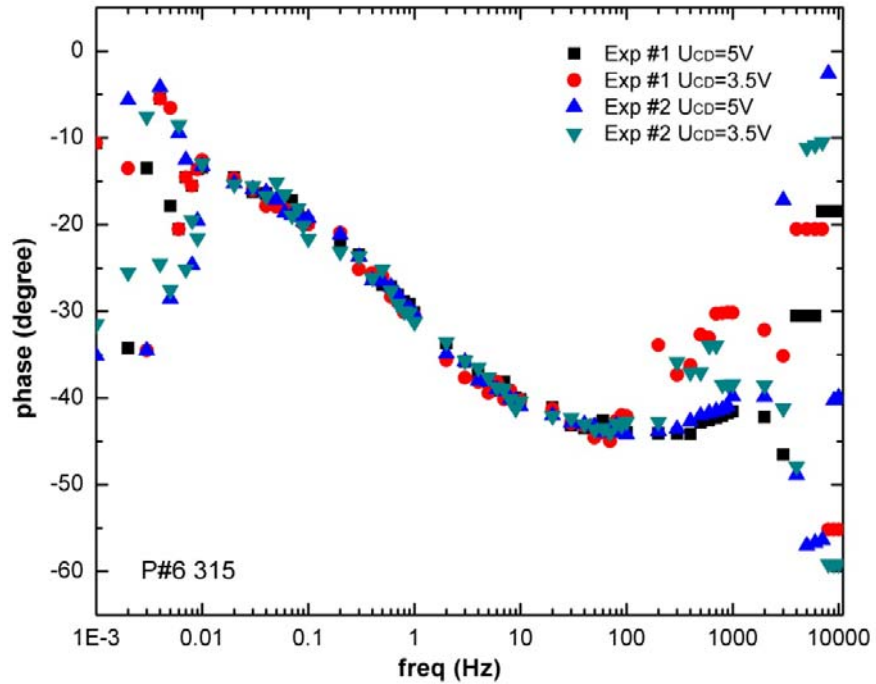
Sample P#6 (Ra=315) Exp. #1: RA=5, RB=1173, Rb=5210  
Exp. #2: RA =10, RB=1173, Rb=9300

(P#6E1 315 marked in the figure means that the studied data were obtained from Exp. #1 with sample P#6 whose resistance is 315 Ω, similar for all figures thereafter)



**Figure 4. 12 Phase of  $U_{AB}^{3\omega}$  collected from measurement**

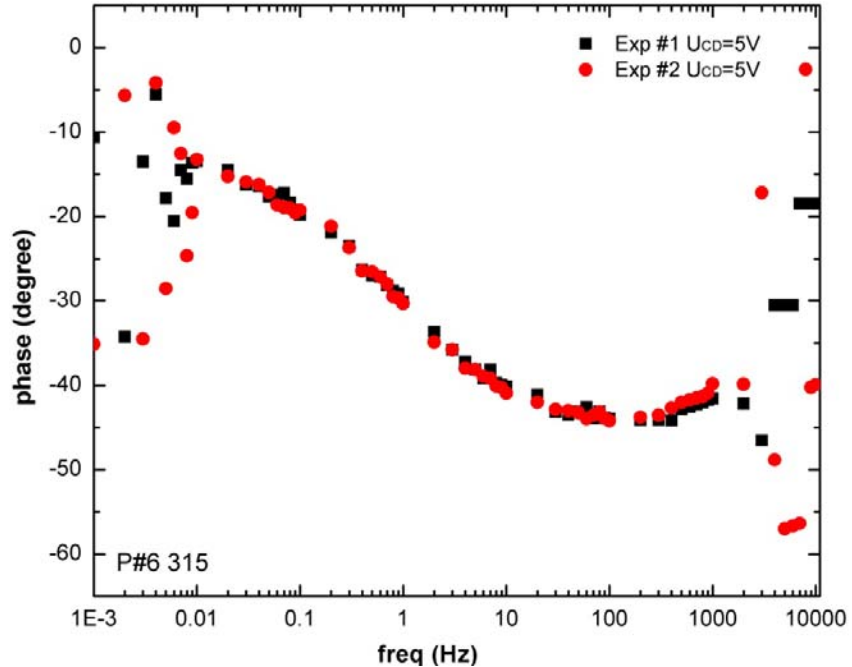
Sample P#6 (Ra=315) Exp. #1: RA=5, RB=1173, Rb=521  
Exp. #2: RA=10, RB=1173, Rb=9300



**Figure 4. 13 Phase of  $U_{AB}^{3\omega}$  collected from measurement**

Sample P#6 ( $R_a=315$ ) Exp. #1:  $R_A=5, R_B=1173, R_b=5210$

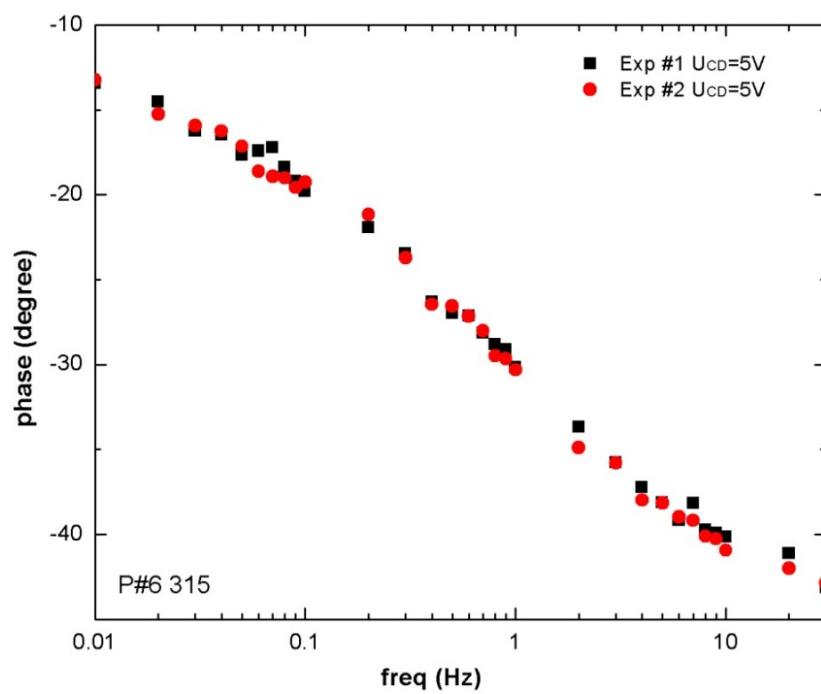
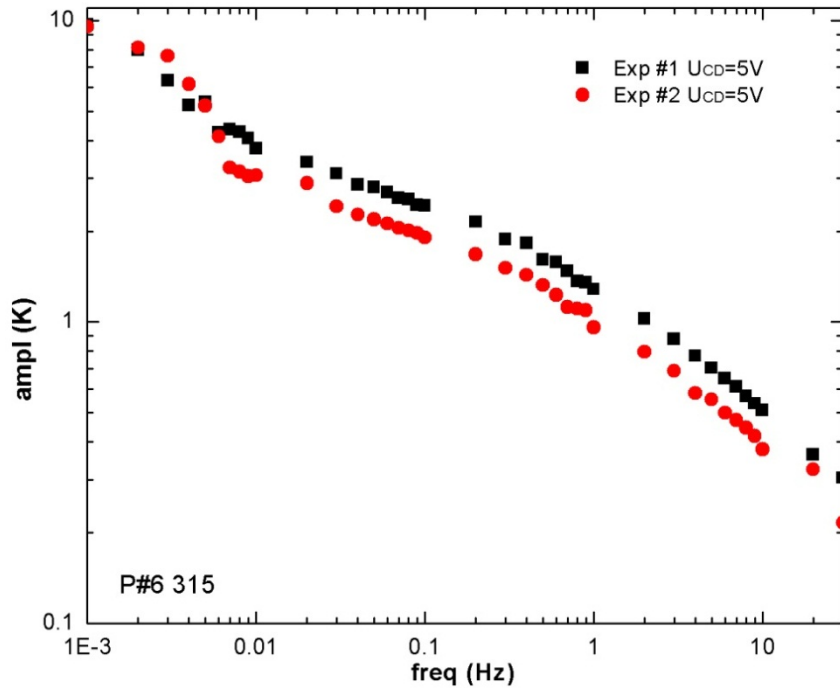
Exp. #2:  $R_A=10, R_B=1173, R_b=9300$



**Figure 4. 14 Phase of  $U_{AB}^{3\omega}$  collected from measurement**

Sample P#6 ( $R_a=315$ ) Exp. #1:  $R_A=5, R_B=1173, R_b=5210$

Exp. #2:  $R_A=10, R_B=1173, R_b=9300$



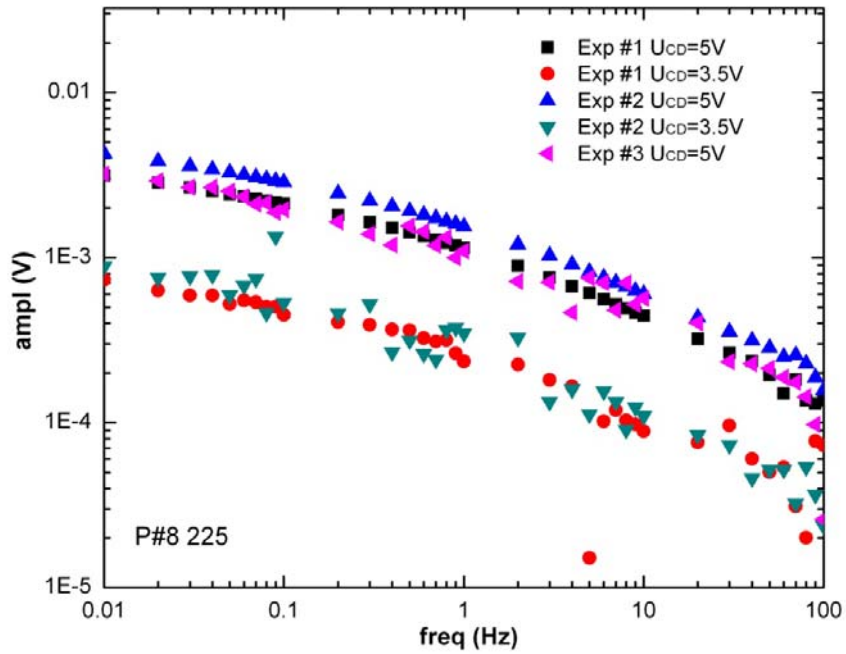


**Figure 4. 17 Amplitude of  $U_{AB}^{3\omega}$  collected from measurement**

Sample P#8 ( $R_a=225$ ) Exp. #1:  $R_A=30, R_B=2200, R_b=16000$

Exp. #2:  $R_A=50, R_B=2200, R_b=16000$

Exp. #3:  $R_A=175, R_B=2200, R_b=16000$

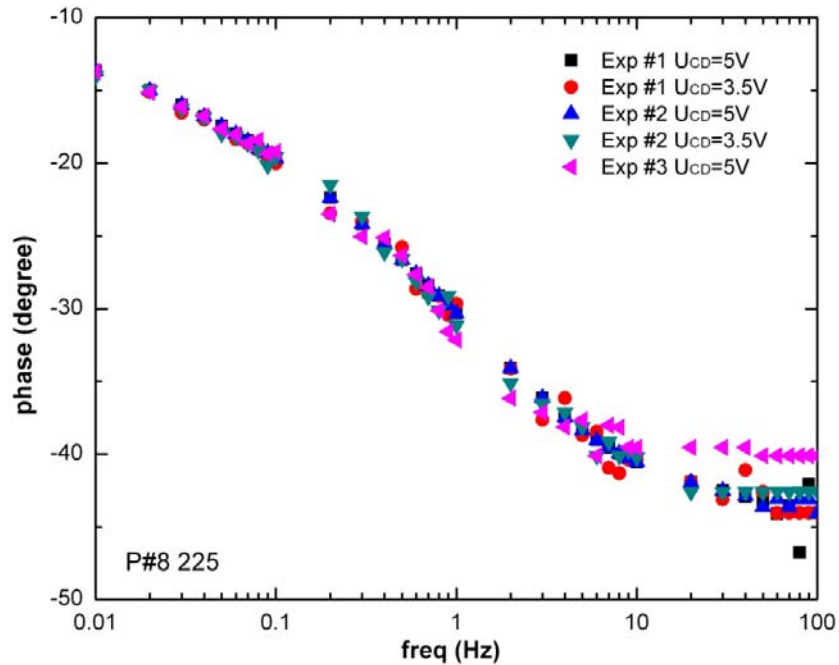


**Figure 4. 18 phase of  $U_{AB}^{3\omega}$  collected from measurement**

Sample P#8 ( $R_a = 225$ ) Exp. #1:  $R_A=30, R_B=2200, R_b=16000$

Exp. #2:  $R_A=50, R_B=2200, R_b=16000$

Exp. #3:  $R_A=175, R_B=2200, R_b=16000$

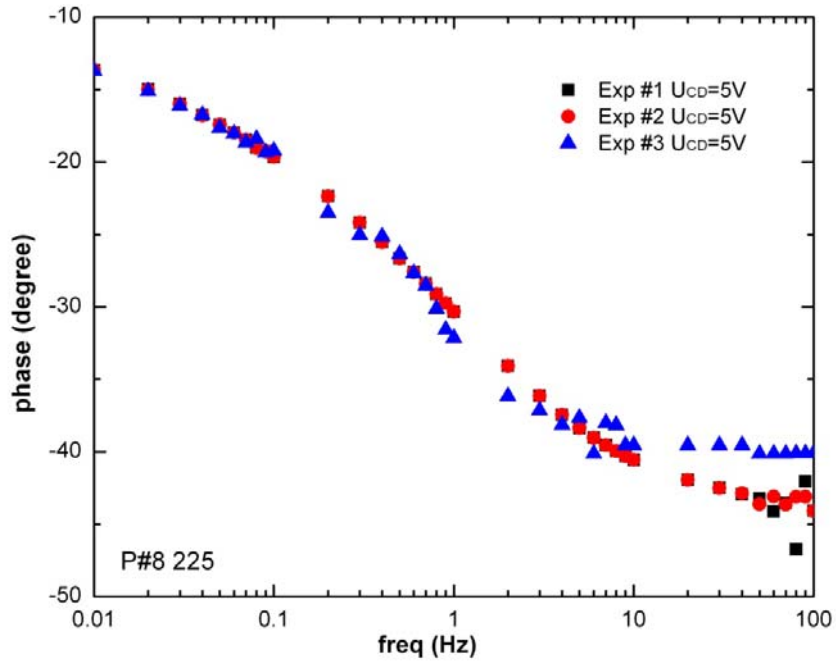
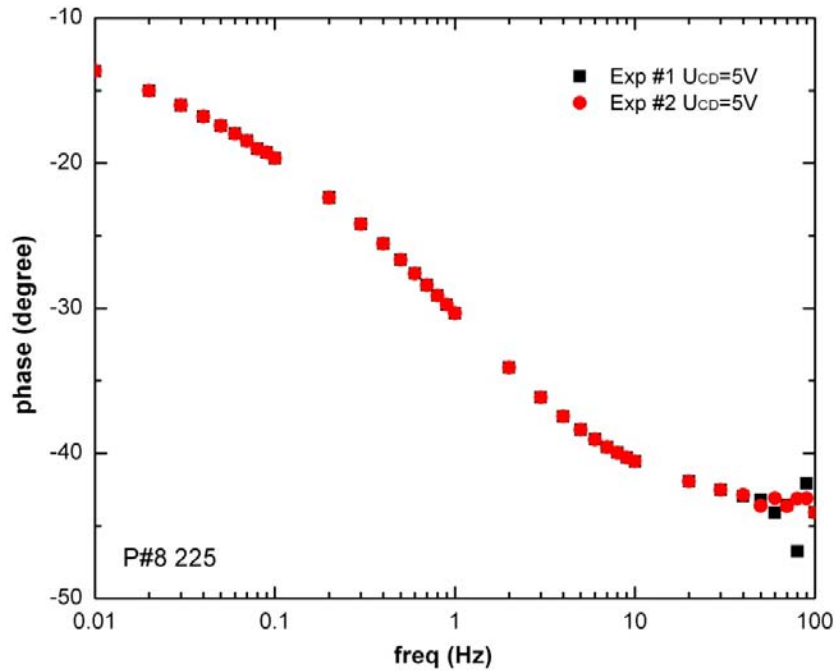


**Figure 4. 19 phase of  $U_{AB}^{3\omega}$  collected from measurement**

Sample P#8 ( $R_a = 225$ ) Exp. #1:  $R_A = 30, R_B = 2200, R_b = 16000$

Exp. #2:  $R_A = 50, R_B = 2200, R_b = 910$

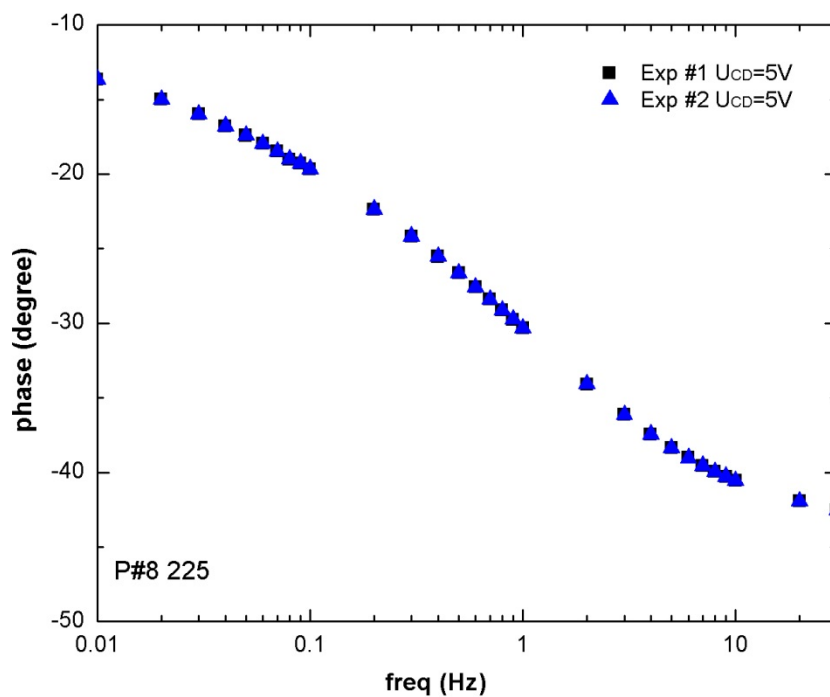
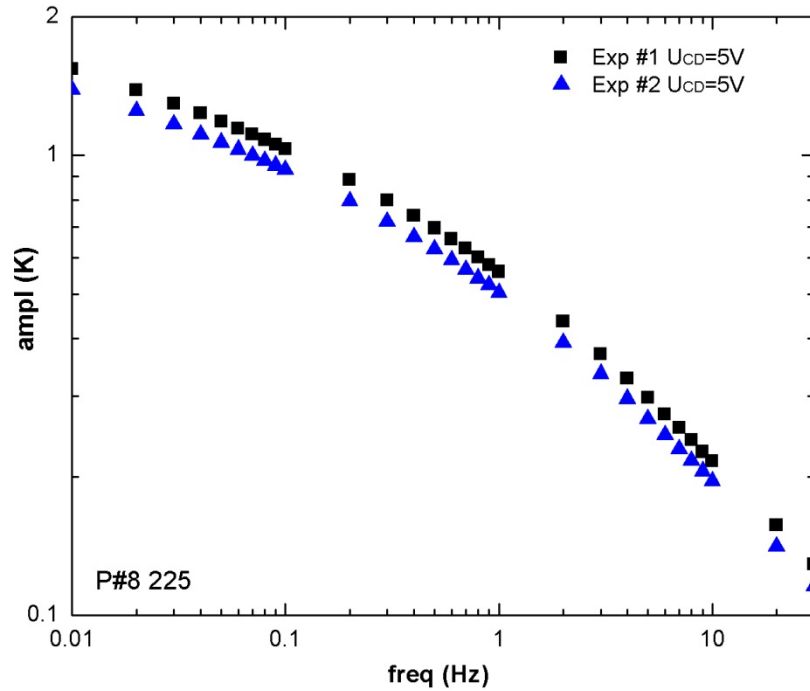
Exp. #3:  $R_A = 175, R_B = 2200, R_b = 3100$



**Figure 4. 20 phase of  $U_{AB}^{3\omega}$  collected from measurement**

Sample P#8 ( $R_a = 225$ ) Exp. #1:  $R_A = 30, R_B = 2200, R_b = 16000$

Exp. #2:  $R_A = 50, R_B = 2200, R_b = 9100$



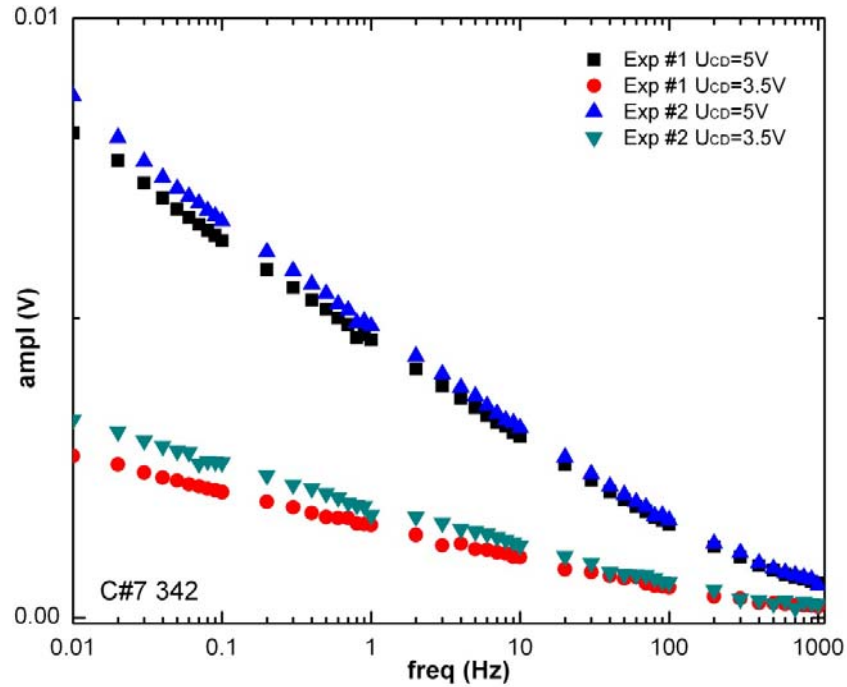


**Figure 4. 23 Amplitude of  $U_{AB}^{3\omega}$  collected from measurement**

Sample P#7 ( $R_a = 342$ ) Exp. #1:  $R_A=48.3, R_B=1773, R_b=12495$

Exp. #2:  $R_A=48.3, R_B=1773, R_b=13100$

(C#7E1 342 marked in the figure means the studied data relate to sample C#7 with resistance 342  $\Omega$  and Exp. #1, similar for all figures in this work)

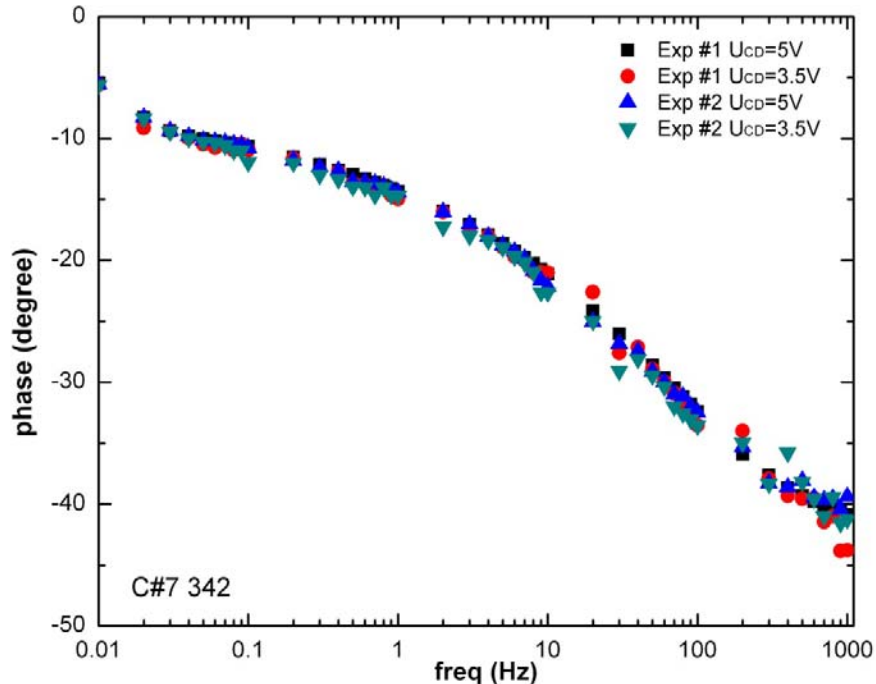
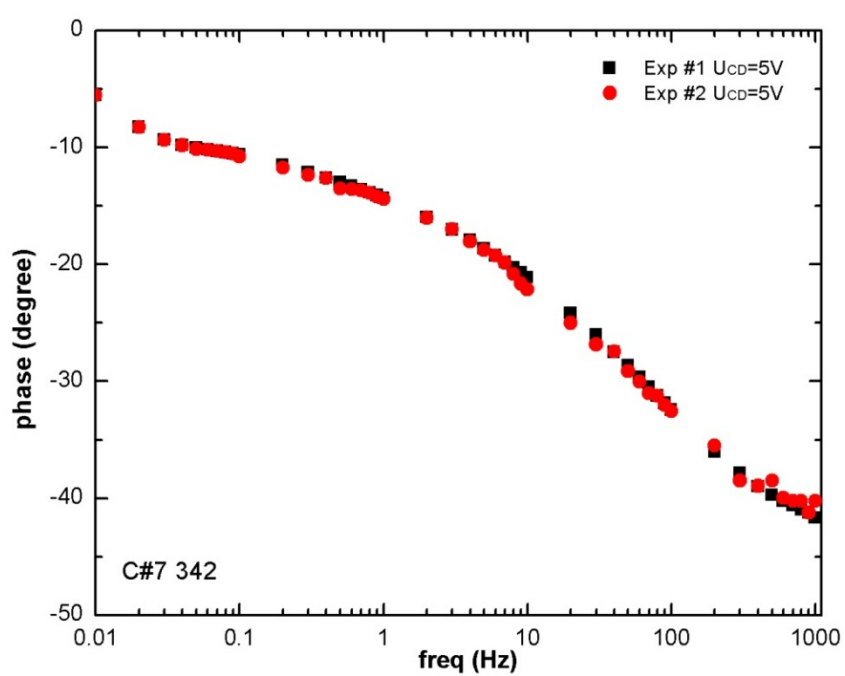
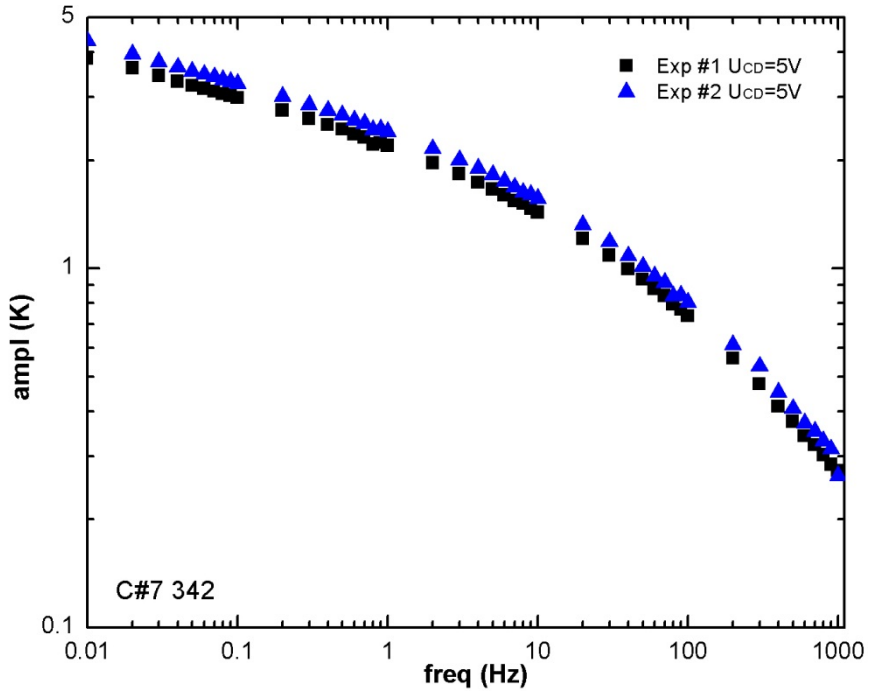


**Figure 4. 24 Phase of  $U_{AB}^{3\omega}$  collected from measurement**

Sample P#7 ( $R_a = 342$ ) Exp. #1:  $R_A=48.3, R_B=1773, R_b=12495$

Exp. #2:  $R_A=48.3, R_B=1773, R_b=13100$



# Chapter 5

## Parameter estimation: Results and discussion

After having obtained the experimental result and derived the theoretical solution for amplitude and phase lag as discussed in Chapter 3 and 4, respectively, parameter estimation for thermal properties is ready to be carried out. This chapter starts with an overview of the parameter estimation method, and then proceeds with a report and discussion of the IPE results for four PMMA and four carbon fiber composite samples.

### 5.1 Overview

Extraction of information from data is one of the fundamental tasks of engineering and science. “Parameter estimation is a discipline that provides tools for the efficient use of data in the estimation of constants appearing in mathematical models and for aiding in modeling of phenomena.” [106, page 1]

Parameter estimation can also be visualized as a study of inverse problems. Regarding this work, the heat transfer model and theoretical temperature results discussed in Chapter 3 are cause and effect, where the fact that all properties are known make it possible to calculate temperature results. This is called a forward problem, where given input values (thermal properties, heat flux etc.), the task is to calculate the output

(temperature). This process must be inverted to solve the parameter estimation problem. That is, given the experimental temperature results, the task is to seek the parameter values. This is an inverse problem in heat transfer.

The scope of this work is to seek the thermal properties of composite material, which are referred to as “constants” by Beck & Arnold [106, page 1]. The mathematical model built and solved in Chapter 3 and discrete measurements of phase and amplitude data collected at different frequency points reported in Chapter 4 will be used to estimate values for these parameters. The least square method will be used to estimate the numerical values of the parameters by fitting the theoretical model to a set of experimental data. Section 5.1.2 gives a brief description of the numerical implementation. Section 5.2 and 5.3 present the results of PMMA and carbon fiber samples.

**Basic idea** The parameter estimation in this work is accomplished by the least square optimization method. That is, the unknown thermal properties will be deduced from a systematic comparison between experimental data and theoretical model. Fig. 5.1 shows the basic idea of the program for parameter estimation. The objective is to find the sought-after parameter set  $x$  that solves the problem

$$S = \min_x \sum_i (F(x, f_i) - ydata_i)^2 \quad (5.1)$$

where  $F(x, f_i)$  represents the theoretical solution derived from the mathematical model discussed in Chapter 3, which is a function of the unknown parameter set  $x$  and

frequency  $f_i$ ;  $ydata$  denotes the corresponding experimental data reported in Chapter 4, which are collected at discrete frequency points.

**Curve fitting** The objective is to fit the theoretical model  $F(x, f_i)$  to a set of experimental data  $ydata$  to estimate the unknown parameter set  $x$ . The unknown parameters are determined by varying the parameters until the best match between measured data and model calculated solution is obtained.

**Weighting** To improve the accuracy of curve-fit, both amplitude and phase data are used for the least squares fitting simultaneously. Weighted least squares are applied to overcome the fact that the values of amplitude and phase data differ greatly in magnitude. That is, to assign different weights to rescale the magnitude of phase and amplitude data so that the weighted/scaled amplitude and phase value are on a level with each other. Thus, the following equation is solved:

$$\begin{aligned} \min S = \min_x & \left[ \sum_i (w1' \times ampl(x, f_i) - w1 \times ampldata_i)^2 \right. \\ & \left. + \sum_i (w2' \times phase(x, f_i) - w2 \times phasedata_i)^2 \right] \end{aligned}$$

where the values of  $w1$ ,  $w1'$ ,  $w2$  and  $w2'$  are taken to make both the weighted amplitude and phase data to have a maximum value 1:

$$w1 = 1 / \max_x(ampldata_i)$$

$$w1' = 1 / \max_x(A(x, f_i))$$

$$w2' = 1 / \max_x(-phase(x, f_i))$$

$$w2 = 1 / \max_x (-phasedata_i).$$

**Algorithm** The nonlinear search procedure starts with a set of estimated values of all the parameters. Let the initial estimate be  $x^{(0)}$ , calculate the corresponding value of

$$S = \sum_i (F(x, f_i) - ydata_i)^2$$

Then adjust the values of  $x^{(0)}$  to a new one  $x^{(1)}$ , and keep carrying out the iterations until a certain criteria regarding  $S$  is approached and satisfied. Matlab optimization toolbox™ is utilized to implement the numerical calculation. The trust-region-reflective algorithm is applied, which is a subspace trust-region method and is based on the interior-reflective Newton method. Each iteration involves the approximate solution of a large linear system using the method of preconditioned conjugate gradients.

**Termination criteria** Termination tolerance of the iteration is controlled by manipulating the following parameters to get the satisfying curve-fit results between theoretical model and experimental data.

- Termination tolerance on  $x$  (TolX). TolX is a lower bound on the size of a step, meaning the norm of  $(x_i - x_{i+1})$ . If the solver attempts to take a step that is smaller than TolX, the iterations end. In this work, the value of TolX is typically set to be 1e-200.
- Termination tolerance on the function value of  $S$  (TolFun). TolFun is a lower bound on the change in the value of the objective function during a step. If  $|S(x_i) - S(x_{i+1})| <$ TolFun, the iterations end. In this work, the value of TolFun is typically set to be 1e-20.

- Maximum number of function evaluations allowed (MaxFunEvals). MaxFunEvals is the maximum number of iteration, when the number of iteration exceeds this value, the iterations end. In this work, the value of MaxFunEvals is typically set to be 5000.

## 5.2 Results for PMMA samples

### 5.2.1 Introduction

**Validation** Validation of the parameter estimation method was performed using PMMA (Poly(methyl methacrylate)) material, since its thermal properties are known and relatively close to carbon-fiber/epoxy composite material. The thermal diffusivity value of PMMA ( $\alpha_h=1.28 \times 10^{-7}$  m<sup>2</sup>/s) provided by the handbook “*Thermophysical properties of matter*” [107] is adopted as the reference value to be compared with the parameter estimation results in this work.

**Sought-after parameters** One of the sought-after parameters for PMMA samples is thermal diffusivity defined as  $\alpha = \frac{k}{\rho c_p}$ . Theoretically, amplitude data should be sensitive to thermal conductivity  $k$ , while phase only depends on thermal diffusivity  $\alpha$ . However, thermal conductivity  $k$  always appears together with the total amount of heat transferred into the sample  $q$  in the form of  $q/k$  in the analytical solution of temperature. The amount of heat  $q$  gained by the sample is hard to quantify, thus unfortunately we are not able to obtain the value of thermal conductivity  $k$  distinct from the combination of  $q$  and  $k$ . Nonetheless, since the density  $\rho$  and capacity  $c_p$  of PMMA material are easily determined,

the thermal conductivity  $k$  could be readily calculated based on the gained value of thermal diffusivity  $\alpha$ . Parameter  $A$  representing the ratio of heat amount  $q$  between the model-calculated value and actual heat amount gained by samples occurred in the experiment is curve fitted as an unknown parameter, which is a function of  $q/k$ . Therefore, the actual sought parameters for PMMA samples are thermal diffusivity  $\alpha$  and the parameter  $A$ .

**Data selected for parameter estimation** Chapter 4 discussed the impedance analysis model (IAM), which converts the raw experimental data related to voltage  $U_{AB}^{3\omega}$  to the corresponding temperature data  $\Delta T_{IA}$ . The amplitude and phase data of  $\Delta T_{IA}$  are simultaneously used for parameter estimation. As discussed in Chapter 4, there are 4 PMMA samples (noted as sample P#6, P#8, P#10 and P#14) giving relatively smooth data under certain resistor-combinations. Those data sets are selected for curve fitting the sought-after parameters.

## 5.2.2 Results

**Sample P#6** Figures 5.2 and 5.3 present the amplitude and phase data in frequency range [0.01 Hz, 100 Hz] from Exp.#1 and #2 of PMMA sample #6 (denoted as P#6) respectively. Noting values of phase and amplitude differ greatly in magnitude, they are plotted in double y-axis graphs. To better convey the essential information, frequency is presented in logarithmic scale considering that the experimental data was collected equivalently in sets of ten in the following frequency ranges [0.01 Hz, 0.1 Hz], [0.1 Hz, 1 Hz] etc. Amplitude is also plotted in logarithmic scale since amplitude value spans in a wide range roughly between 0.01 K and 5 K.

Figure 5.4 shows the curve-fitting result calculated from the IPE model in which experimental data from Exp. #1 of sample P#6 (consisting of 58 data points) is utilized. The data in frequency range [30 Hz, 100 Hz] are discarded because they are considered not as smooth as data in the selected range [0.01 Hz, 20 Hz]. Similarly, Fig. 5.5 shows the curve-fitting result using the data from Exp. #2 of sample P#6 (consisting of 58 data points). Among all the used data points, the maximum percent difference between measured and model calculated data is 0.56%.

The thermal diffusivity values deduced using the two sets of experimental data are  $\alpha_1=1.235\times10^{-7}$  m<sup>2</sup>/s and  $\alpha_2=1.242\times10^{-7}$  m<sup>2</sup>/s, respectively. The percent error of the two results compared to the handbook value of PMMA ( $\alpha_h=1.276 \times 10^{-7}$  m<sup>2</sup>/s) are calculated as below

$$\% \text{ Error } \alpha_1 = \frac{|\alpha_1 - \alpha_h|}{\alpha_h} \times 100 = 3.2\%$$

$$\% \text{ Error } \alpha_2 = \frac{|\alpha_2 - \alpha_h|}{\alpha_h} \times 100 = 2.6\%$$

The error is considered to be large. Comparing the experimental data measured from P#6 (shown in Figs. 5.2 and 5.3) and other samples (for example sample P#8, shown in Figs. 5.6 and 5.7), it could be seen that the data from #6 is less smooth. This may contribute to the fact that the obtained thermal diffusivity estimation result for P#6 is not as accurate as desired.

As discussed in Chapter 3, one side of the sample sits on an aluminum block. The Biot number on that side is also curve-fitted. The obtained Biot number for both cases (Exp #1

and #2) is very close to a very large number 5, which indicates that the side of the aluminum side is close to an isothermal boundary condition-the first kind of boundary condition.

**Sample P#8** Figures 5.6 and 5.7 present the amplitude and phase from Exp. #1 and #2 of PMMA sample #8 (denoted as P#8), respectively. Figs. 5.8 and 5.9 show the curve-fitting result calculated from the IPE model in which experimental data from Exp. #1 and #2 (60 data points for each) of sample P#8 are used, respectively.

The thermal diffusivity values deduced from the IPE model using the two sets of experimental data are  $\alpha_1=1.2843\times10^{-7}$  m<sup>2</sup>/s and  $\alpha_2=1.2840\times10^{-7}$  m<sup>2</sup>/s, respectively. This greatly improves our confidence with the parameter estimation method together with the experiment system. Since the percent error is much closed compared to the handbook value, of greater use is the percent difference between the two results:

$$\% \text{ diff } \alpha = \left| \frac{\alpha_1 - \alpha_2}{(\alpha_1 + \alpha_2)/2} \right| \times 100 = 0.011\%$$

The strong consistency between the two results well validates the reliability of the measurement system. In addition, the fitted Biot number on the aluminum side is also curve-fitted which is also very close to 5.

**Sample P#10** Figures 5.10 and 5.11 present the amplitude and phase data from Exp. #1 and #2 for PMMA sample #10 (denoted as P#10), respectively. Figs. 5.12 and 5.13 show Exp. #1 and #2 (60 data points for each) of sample P#10 are used, respectively.

The thermal diffusivity values deduced using the two sets of experimental data are  $\alpha_1=1.2842\times10^{-7}$  m<sup>2</sup>/s and  $\alpha_2=1.2846\times10^{-7}$  m<sup>2</sup>/s, respectively. The percent difference between the two results is

$$\% \text{ diff } \alpha = \left| \frac{\alpha_1 - \alpha_2}{(\alpha_1 + \alpha_2)/2} \right| \times 100 = 0.007\%$$

In addition, the fitted Biot number on the aluminum side is also curve-fitted. It is also very close to 5.

**Sample P#14** Figures 5.14, 5.15 and 5.16 present the amplitude and phase data from Exp. #1, #2 and #3 of PMMA sample #14 (denoted as P#14), respectively. The sample was placed on an aluminum block, a wood table and in air in the three experiments, respectively.

Figs. 5.17, 5.18 and 5.19 show the curve-fitting result calculated from parameter estimation in which experimental data from Exp. #1, #2 and #3 (60 data points for each) of sample P#14 are used, respectively.

The thermal diffusivity value deduced using the three sets of experimental data is  $\alpha_1=1.2843\times10^{-7}$  m<sup>2</sup>/s,  $\alpha_2=1.2844\times10^{-7}$  m<sup>2</sup>/s and  $\alpha_3=1.2849\times10^{-7}$  m<sup>2</sup>/s, respectively. The largest percent difference among the three results is

$$\% \text{ diff } \alpha = \left| \frac{\alpha_1 - \alpha_3}{(\alpha_1 + \alpha_3)/2} \right| \times 100 = 0.023\%$$

The fitted Biots number for the three experiments are 5.62, 0.024 and 1.593, which are reasonable values for aluminum, wood and air surface, respectively. This also validates the method.

### 5.2.3 Summary of PMMA results

The thermal diffusivity results deduced from the parameter estimation method using experimental data from 4 different PMMA samples are summarized in Table 5.1.

**Table 5. 1 Summary of the IPE results of PMMA samples**

Sample ID	Experiment ID	$\alpha$ (m <sup>2</sup> /s)	% Error	Biot Number
P#6	E#1	$1.235 \times 10^{-7}$	3.2%	$\approx 5$ (aluminum surface)
	E#2	$1.242 \times 10^{-7}$	2.6%	$\approx 5$ (aluminum surface)
P#8	E#1	$1.2843 \times 10^{-7}$	0.65%	$\approx 5$ (aluminum surface)
	E#2	$1.2840 \times 10^{-7}$	0.62%	$\approx 5$ (aluminum surface)
P#10	E#1	$1.2842 \times 10^{-7}$	0.64%	$\approx 5$ (aluminum surface)
	E#2	$1.2846 \times 10^{-7}$	0.67%	$\approx 5$ (aluminum surface)
P#14	E#1	$1.2843 \times 10^{-7}$	0.65%	$\approx 5$ (aluminum surface)
	E#2	$1.2843 \times 10^{-7}$	0.65%	$\approx 0.02$ (wood surface)
	E#3	$1.2849 \times 10^{-7}$	0.70%	$\approx 1.6$ (in air)

The following facts verify the reliability of the parameter estimation method and the experimental system:

- Comparing with the handbook thermal diffusivity value of PMMA ( $\alpha_h=1.28 \times 10^{-7}$  m<sup>2</sup>/s), the %error of the obtained results for samples P#8, #10 and #14 and the handbook value  $\alpha_h$  is lower than 0.7%.

- All the results from samples P#8, #10 and #14 under varied experimental conditions (different resistor-combination) are strongly consistent.
- Reasonable Biot numbers are fitted for the corresponding surface condition of samples in experiments.
- Observing that all the thermal diffusivity values from sample P#8, #10 and #14 agree to the thousandths place, which reasons that the IPE calculated results are trustworthy at least till the third digit after the decimal point.

The estimated thermal diffusivity values of sample P#6 differs from the handbook value with a percent error larger than 2.9%, which may due to the non-sufficient smoothness of the data. This suggests that well smooth data sets should be selected for parameter estimation.

## 5.3 Results for carbon fiber sample

### 5.3.1 Introduction

**Sought-after parameters** The sought-after parameters for carbon fiber samples are in-plane thermal conductivity  $k_x$ , through-thickness thermal conductivity  $k_y$  and thermal diffusivity defined as  $\alpha = \frac{(k_x k_y)^{0.5}}{\rho c_p}$ . The anisotropic model is sensitive to both  $k_x$  and  $k_y$ .

Similar to the isotropic model for PMMA samples, a constant value  $A$  representing the ratio of heat amount  $q$  between the model-calculated value and actual heat amount gained by samples occurred in the experiment is curve fitted as an unknown parameter.

**Data selected for parameter estimation** Chapter 4 discussed the impedance analysis model (IAM), which converts the raw experimental data related to voltage  $U_{AB}^{3\omega}$  to the corresponding temperature data  $\Delta T_{IA}$ . The amplitude and phase data of  $\Delta T_{IA}$  are simultaneously used for parameter estimation. As discussed in Chapter 4, there are 4 carbon fiber samples (noted as sample C#7, P#8, P#13 and P#16) for which smooth data were obtained. For each sample, the smoothest data set is selected for curve fitting the sought-after parameters.

### 5.3.2 Results

As discussed in Chapter 4, data from Exp. #1 is the best among those results from carbon fiber sample C#7. Figure 5.20 plots the phase and amplitude together in a double y-axis graph since the values of phase and amplitude differ greatly in magnitude. Figure 5.21 shows the curve-fitting result calculated from the parameter estimation method in which experimental data points taken at ninety-two discrete frequency points from Exp. #1 are used where the maximum percent difference between measured and model calculated data is 2.24% among all the used data points. The estimated thermal property values of sample C #7 from the parameter estimation are  $k_x=6.322 \text{ Wm}^{-1}\text{K}^{-1}$ ,  $k_y=0.509 \text{ Wm}^{-1}\text{K}^{-1}$ , and  $\alpha=2.586\times10^{-6} \text{ m}^2/\text{s}$ .

Figure 5.22 presents the amplitude and phase from Exp. #2 from carbon fiber sample C#8. Fig. 5.23 shows the curve-fitting result calculated from the parameter estimation procedure in which ninety-two experimental data points from Exp. #2 are used. Figures 5.24 and 5.25 present the corresponding results for sample C#13. Figures 5.26 and 5.27 are for sample C#16. In all these cases, experimental data collected at ninety-two

frequency points are used. The obtained thermal property values of all these samples are listed in Table 5.2.

### 5.3.3 Discussion

The estimated thermal property results deduced from parameter estimation using experimental data from 4 different carbon fiber samples are reported. Table 5.2 summarizes the results:

**Table 5. 2 Summary of the parameter estimation results of carbon fiber samples**

Sample ID	$k_x$ (W/m K)	$k_y$ (W/m K)	$\alpha \times 10^6$ (m <sup>2</sup> /s)	$\theta$ (degree)
C#7	6.322	0.507	2.586	90°, platinum along/on epoxy
C#8	5.219	0.617	2.436	0°, platinum along/on fiber
C#13	6.942	0.702	3.072	90°, platinum cross fiber
C#16	6.782	0.616	2.787	70°, platinum cross fiber

It is not surprising that the estimated thermal properties of different samples differ. Although all the samples were cut from the same piece of carbon fiber block, the properties of different samples can still vary greatly, depending on fiber orientation, fiber/epoxy volume fraction, uneven air and/or water percentage etc.

Furthermore, the position and orientation of the deposited platinum film strongly affects the result. The angle between surface fibers and platinum line  $\theta$  of each sample is included in Table 5.2. It is observed from this work that the thermal conductivity along the fiber direction is the largest. Next is along the epoxy length direction. Thermal

conductivity perpendicular to the fiber direction is the smallest. Figure 5.28 b) shows photographs of the surfaces of samples C#7, #8, #13 and #16. It can be seen from Fig. 5.28 c) and d), the platinum film length direction is almost perpendicular to the fiber direction. Therefore most of the heat actually propagates along the fiber direction. Since carbon fiber has larger thermal conductivity than epoxy, this may explain the fact that sample C#13 and #16 give the largest  $k_x$ . Shown by Fig. 5.28 b), the platinum film was deposited along the fiber direction, which means heating is on the perpendicular-to-fiber direction, which may explain that sample C#8 gives the smallest  $k_x$ . Shown by Fig. 5.28 a), the platinum film was deposited on the epoxy part, which may explain that sample C#7 gives the next-smallest  $k_x$ .

As discussed in the previous paragraph, the micro structure of the composite affects the in-plane thermal conductivity result. In a similar manner, it also affects the through-thickness thermal conductivity results since the micro structure such as winding direction and fiber thickness under the deposited metal film is not exactly uniform and uncontrollable. This explains the variation in results obtained as well.

Unfortunately, available data from literature pertaining to the in-plane and through-thickness thermal conductivities of carbon-fiber composite are limited. The issue is further complicated by the wide scatter and uncertainty in the constituent material properties generally listed in the literature. Therefore, the results from literature can only be taken as rough reference. The average in-plane and through-thickness thermal conductivities of the four samples used in this work are 6.316 W/m K and 0.611 W/m K, respectively. The ratio of these two values is 10.3. Table 5.3 lists the available data on fiber composite materials obtained by other researchers including the calculated thermal

conductivity ratio between in-plane and through-thickness direction based on the corresponding average values. It can be seen the ratio from the other two literatures is between 9.8 and 11.5, which is rather close to the value obtained in this work (10.3). Furthermore, the through-thickness thermal conductivity acquired in this work generally agrees with the results from literature.

**Table 5. 3 Thermal conductivity of carbon-fiber/epoxy composite from literature**

Fiber/Matrix	In-plane thermal conductivity $k_x$ (W/m K)	Transverse thermal conductivity $k_y$ (W/m K)	$k_x/k_y$ (both are average values)
Graphite/epoxy plain-weave Fabric composite [8]	5.36	0.43~0.50	11.5
Hexcel F593 carbon/epoxy plain-weave pre-preg laminate[29]	2~3.5	0.5~0.8	4.2
Graphite/epoxy matrix lamina [108]	3.8~8.0	0.4~0.8	9.8
Carbon-fiber/epoxy used in this work [109]	-	0.3~0.8	-
Results from this work	5~7	0.5~0.8	10.4

## 5.4 Conclusion

The parameter estimation method is established to seek the thermal properties of PMMA and carbon-fiber/epoxy composite samples. The anisotropic model applied for carbon fiber samples is sensitive to in-plane thermal conductivity, through-thickness thermal conductivity and thermal diffusivity, while the simplified isotropic model used for

PMMA sample is only sensitive to thermal diffusivity. Both phase and amplitude data are utilized simultaneously for curve-fitting. Because they differ significantly in magnitude, weighted least-square curve-fitting is applied.

Validation of the parameter estimation method including the experimental system was performed using PMMA (Poly(methyl methacrylate)) samples for which the thermal properties are given by handbook. Thermal diffusivity results obtained from four PMMA samples are reported. The percent error between the thermal diffusivity values from sample P#8, #10 and #14 compared to the handbook value is 0.62%.

The anisotropic thermal properties of four carbon-fiber/epoxy samples are presented. A comparison of the obtained thermal property result from this work and those from other available literature is given. The obtained results generally agree with the results from literature.

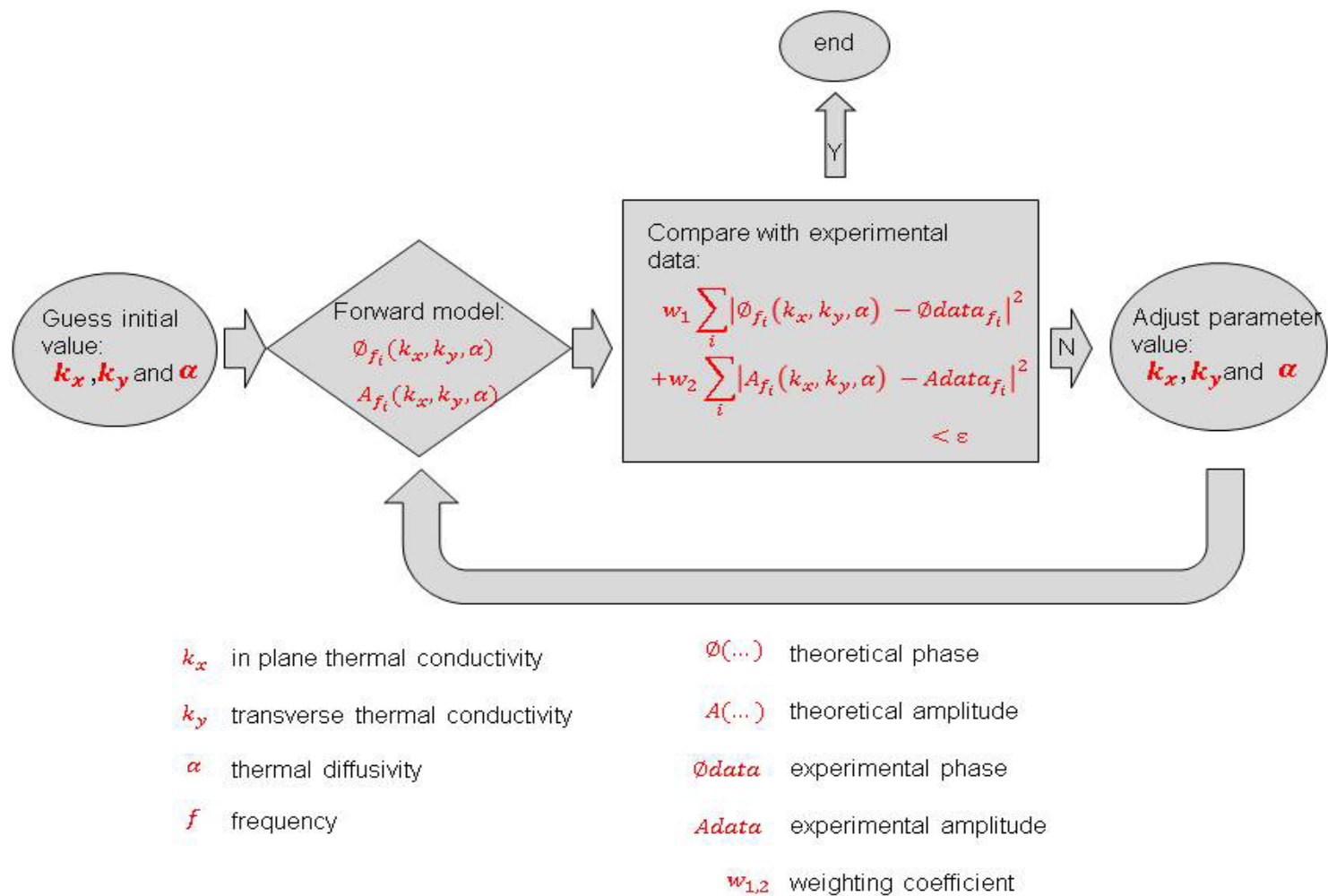
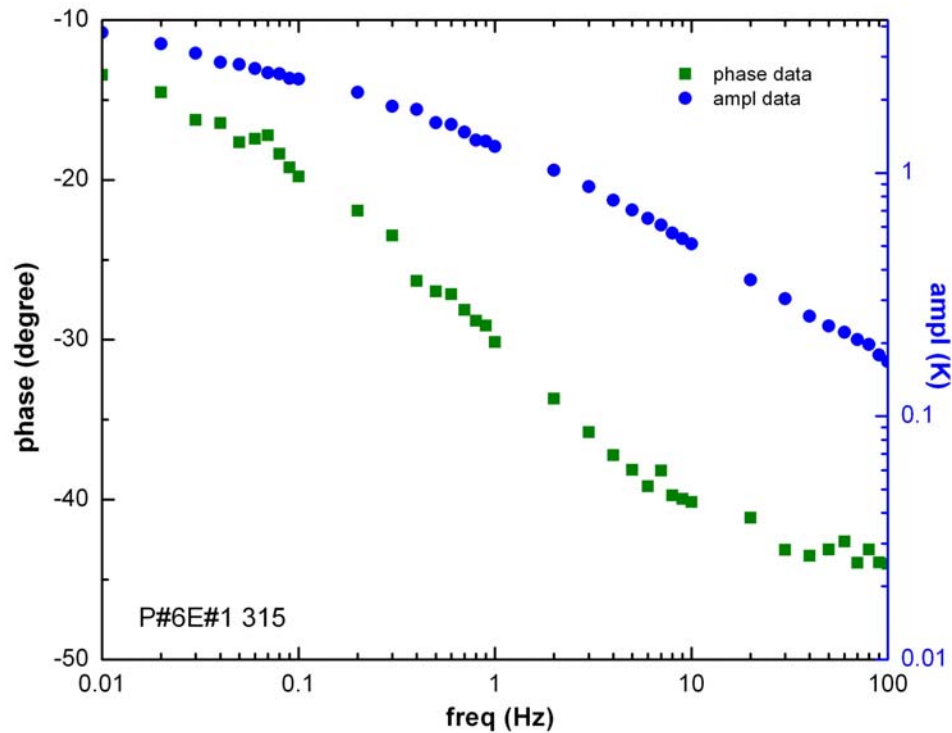
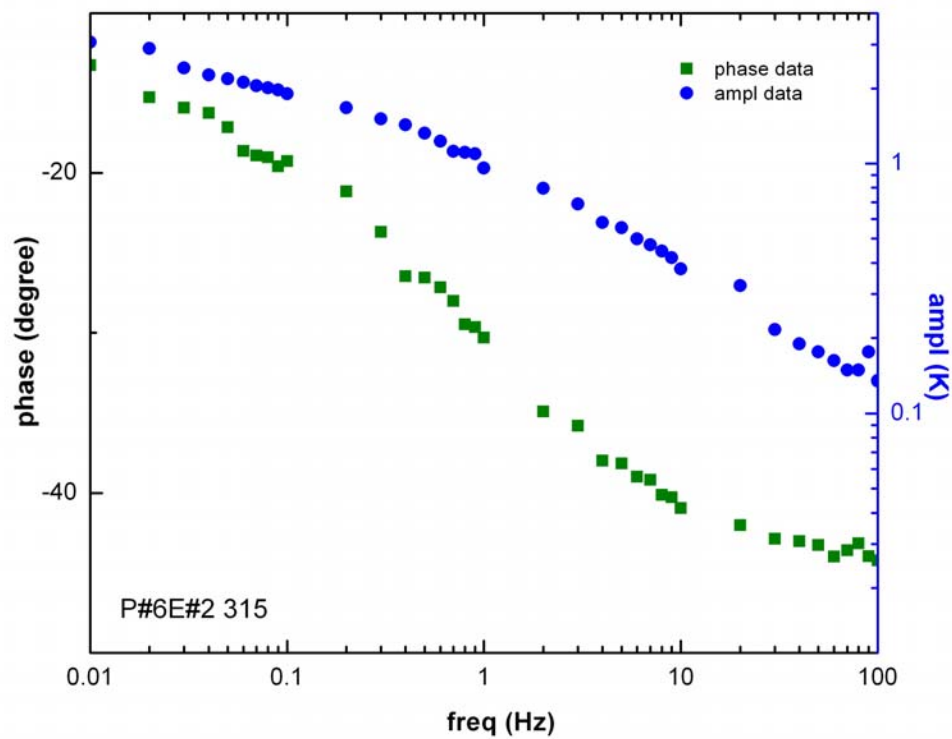


Figure 5.1 The basic idea of inverse parameter estimation



**Figure 5.2 Amplitude and phase used for curve fitting**

(P#6E1 315 marked in the figure means the studied data relate to sample P#6 with resistance 315  $\Omega$ , Exp. #1, similar for all figures in this work)



**Figure 5.3 Amplitude and phase used for curve fitting**

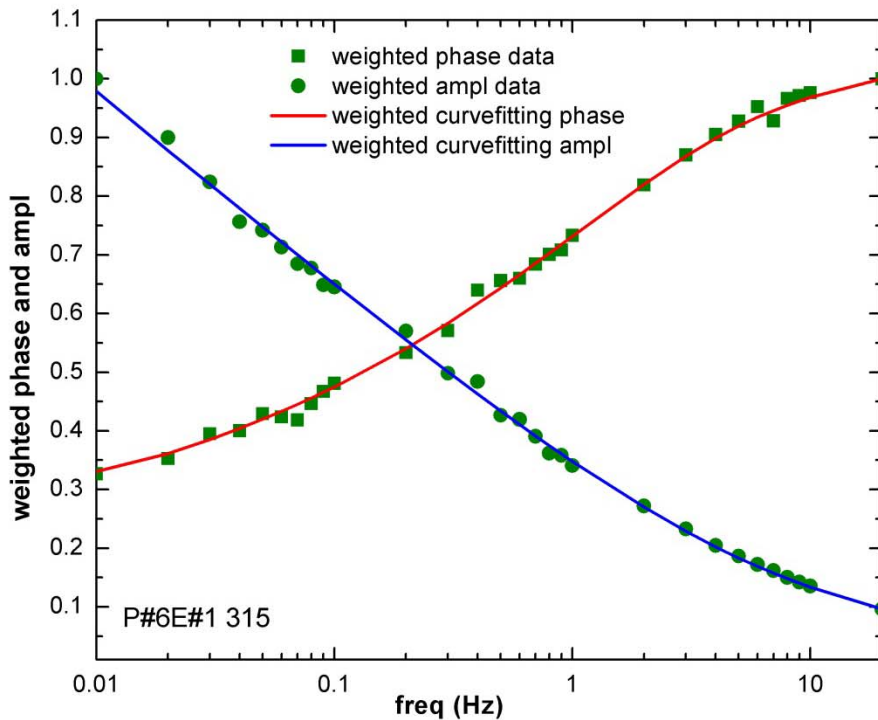


**Figure 5.4 Curve-fitting the amplitude and phase data**

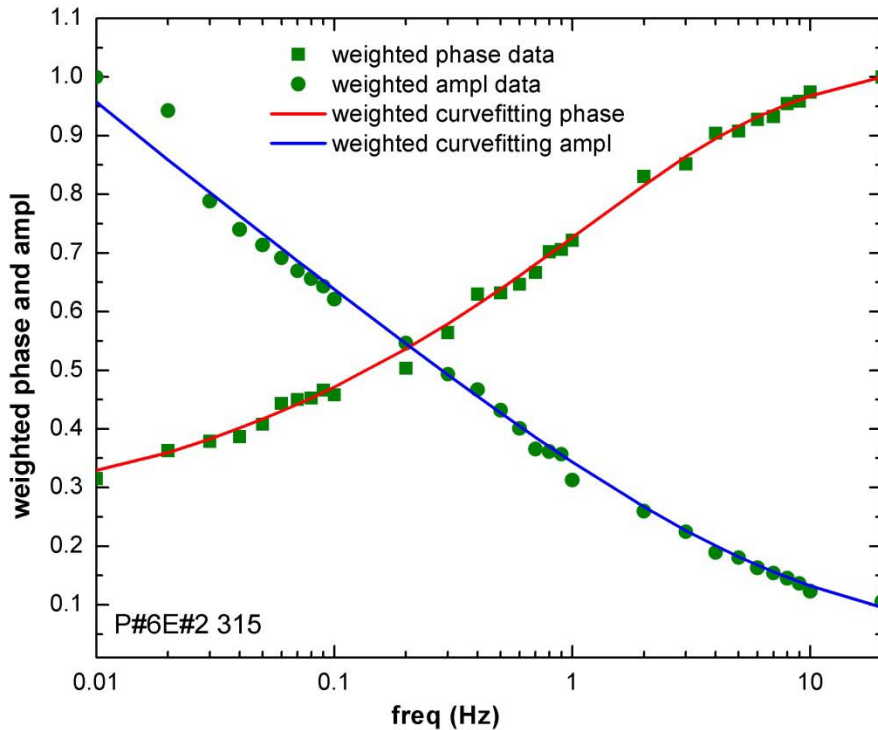


**Figure 5.5 Curve-fitting the amplitude and phase data**

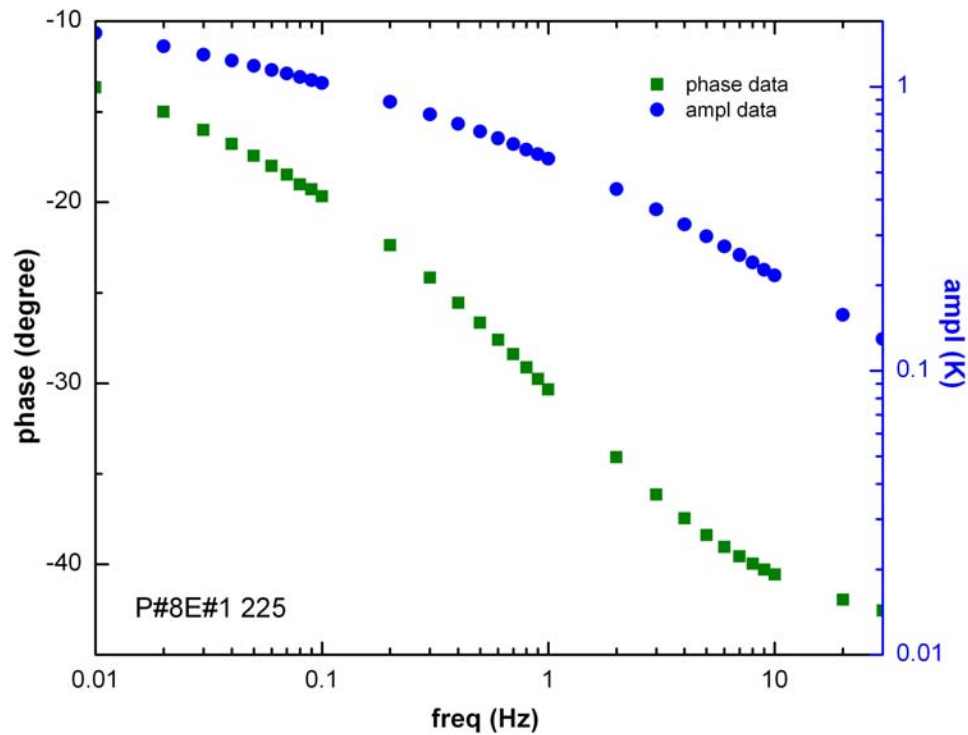


Figure 5. 6 Amplitude and phase used for curve fitting

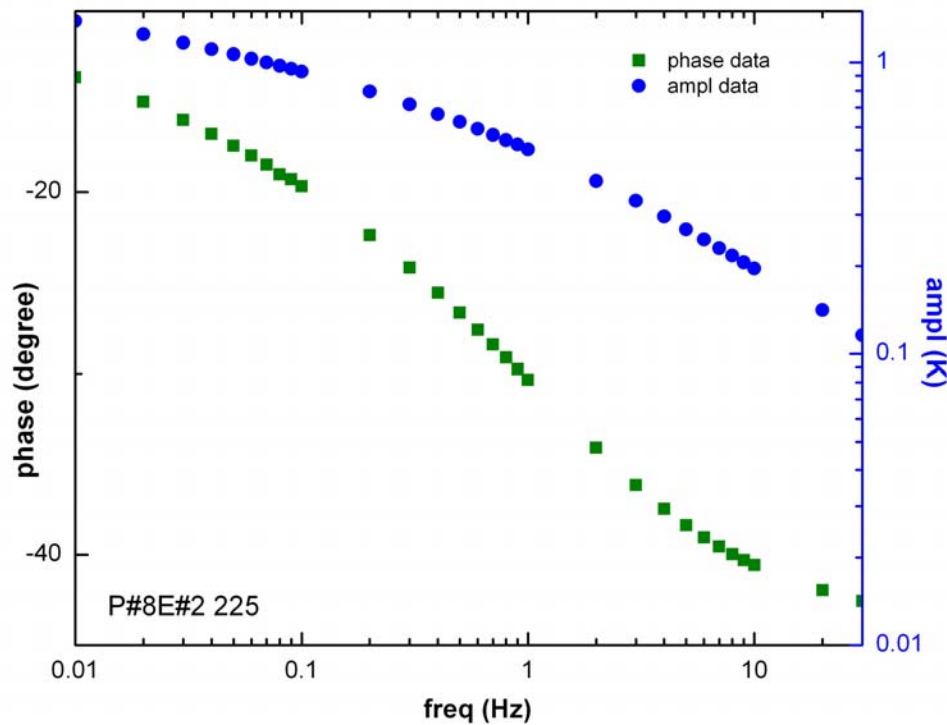
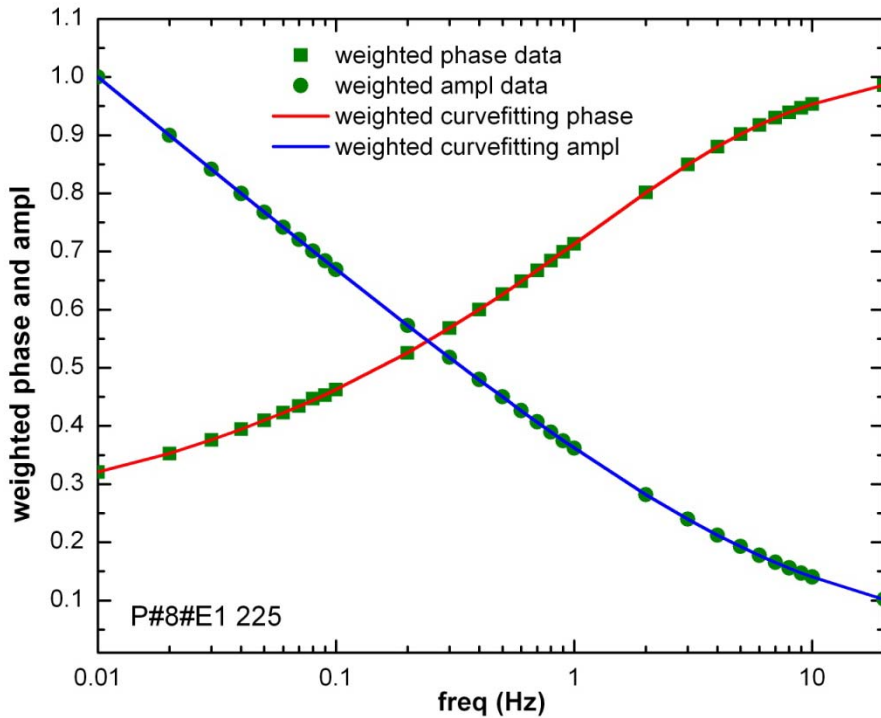
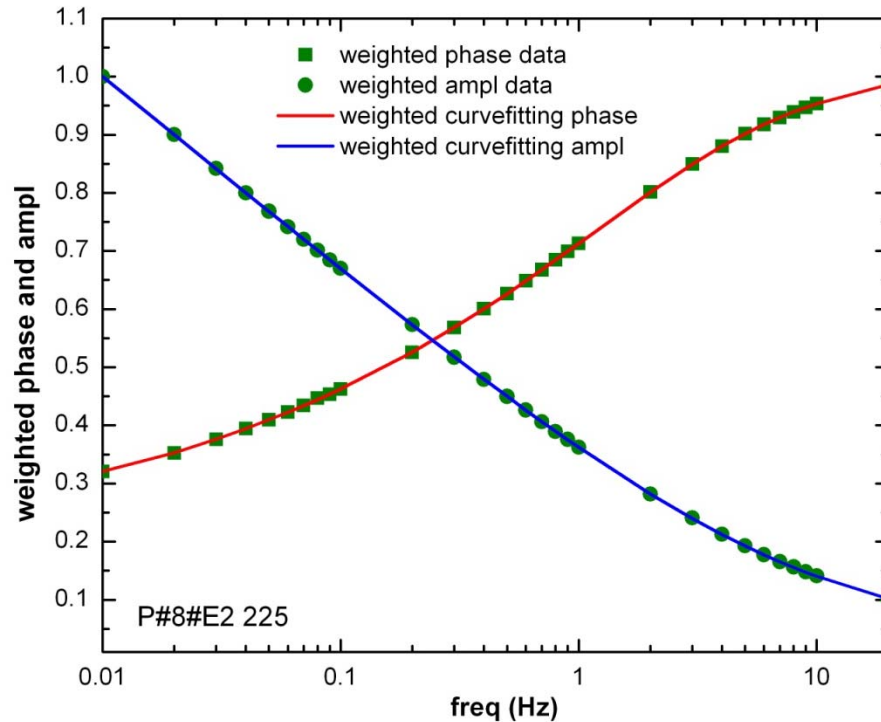


Figure 5. 7 Amplitude and phase used for curve fitting



**Figure 5.8 Curve-fitting the amplitude and phase data**



**Figure 5.9 Curve-fitting the amplitude and phase data**

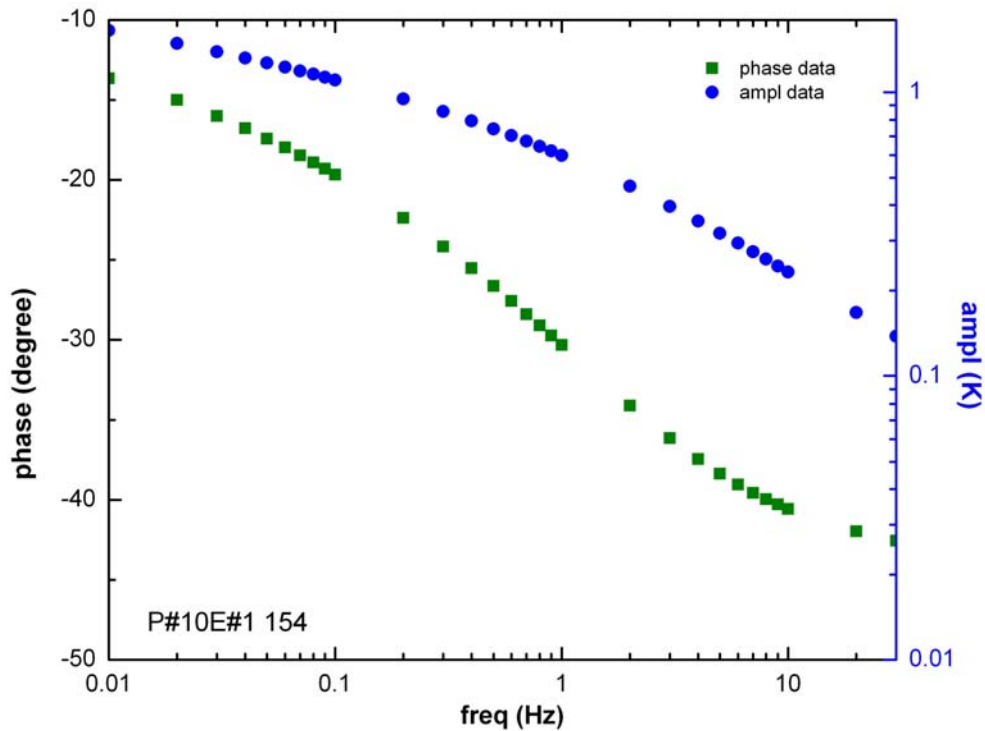


Figure 5. 10 Amplitude and phase used for curve fitting

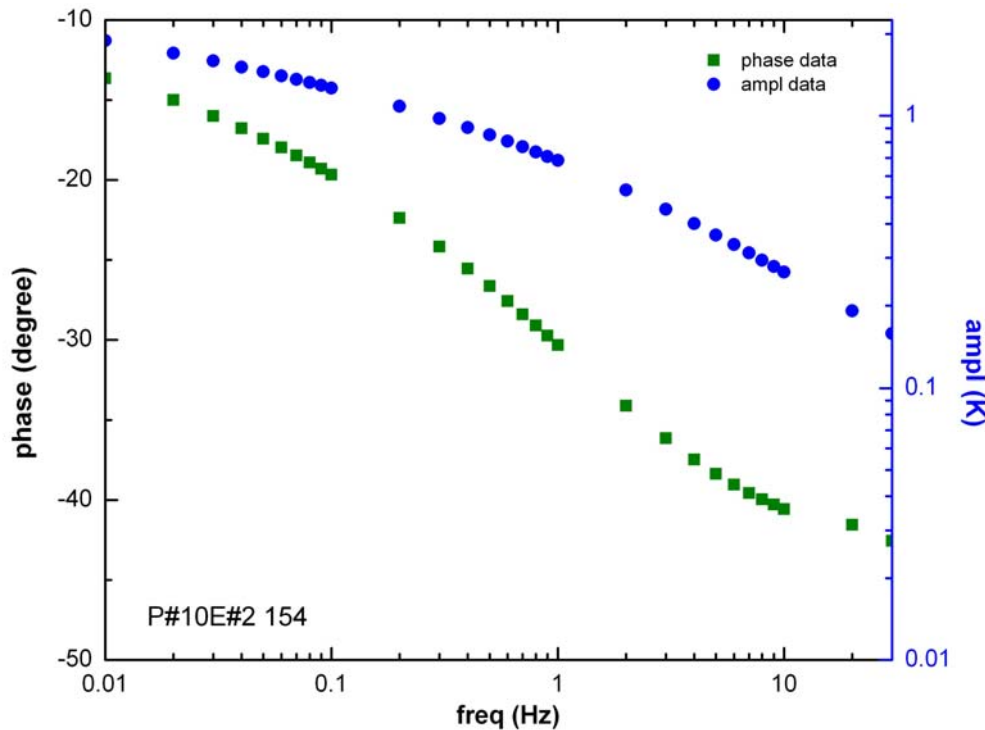
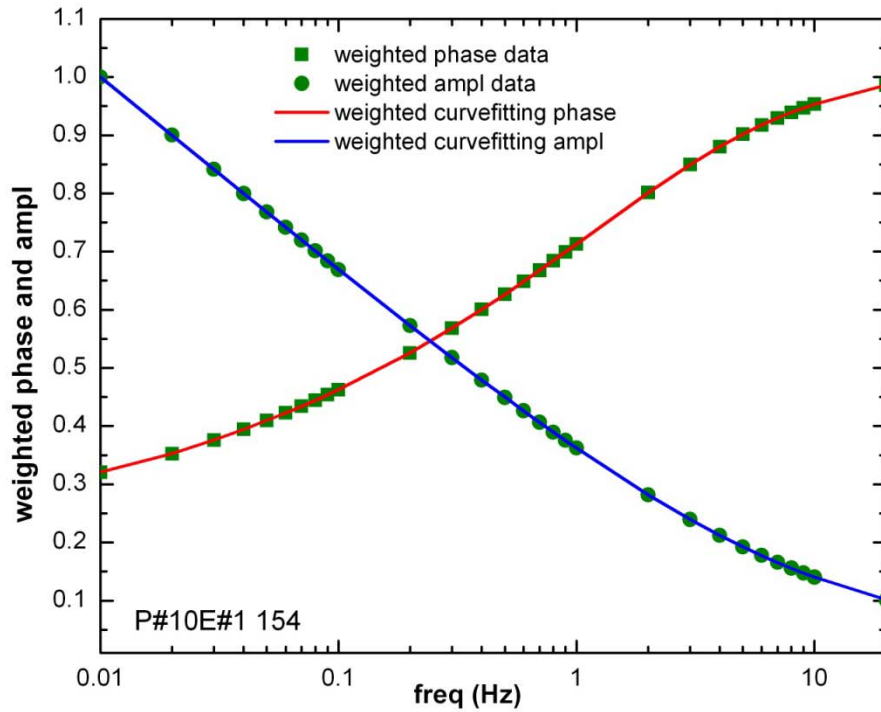
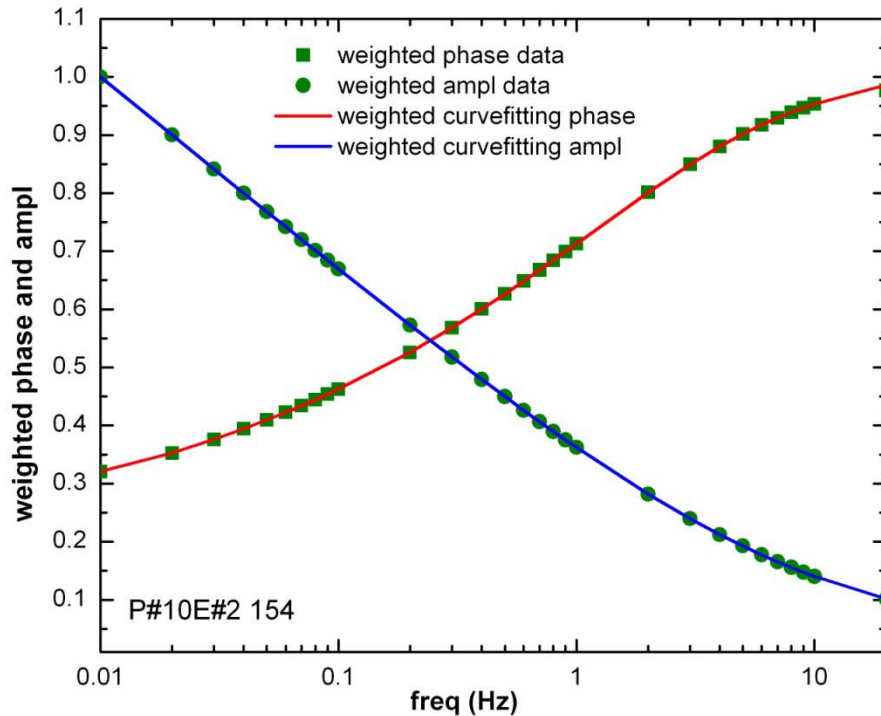


Figure 5. 11 Amplitude and phase used for curve fitting



**Figure 5. 12 Curve-fitting the amplitude and phase data**



**Figure 5. 13 Curve-fitting the amplitude and phase data**

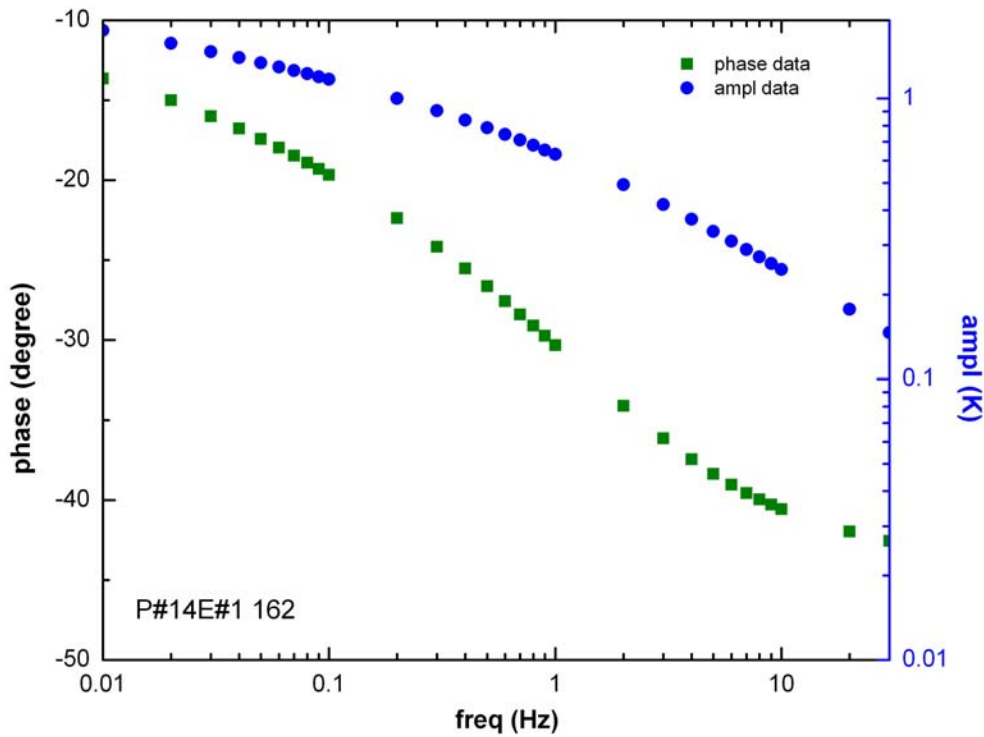


Figure 5. 14 Amplitude and phase used for curve fitting

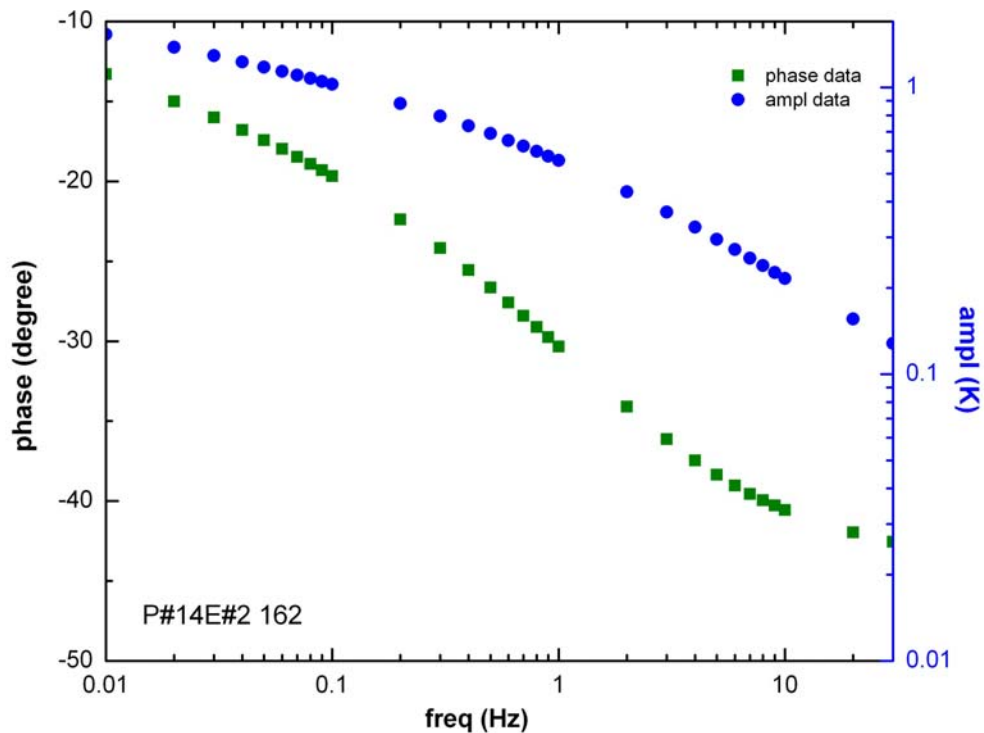
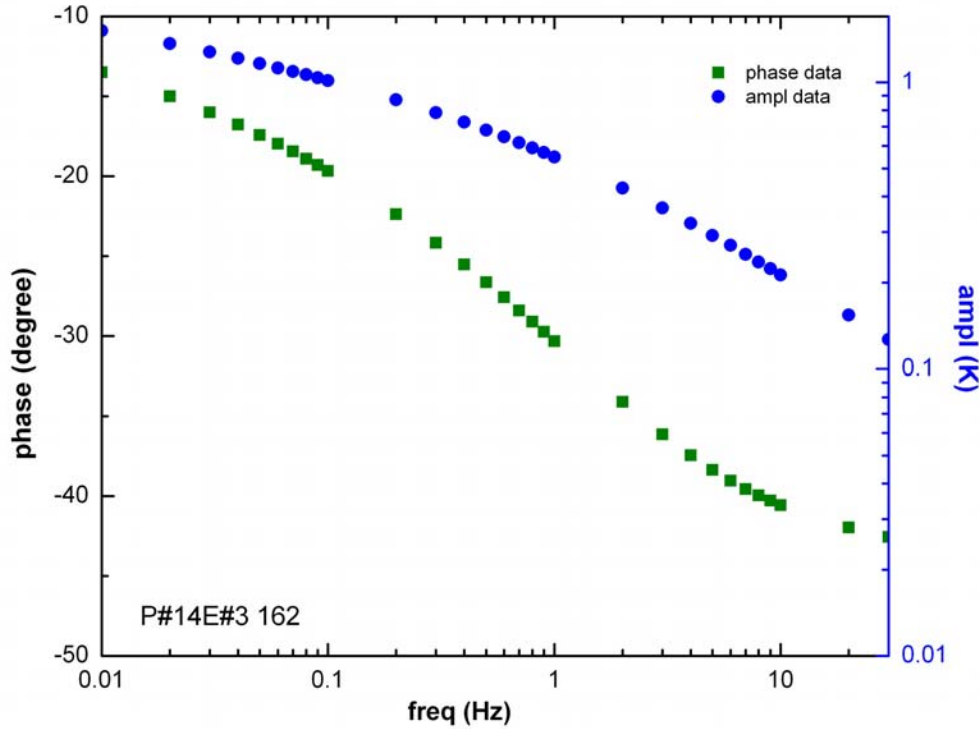
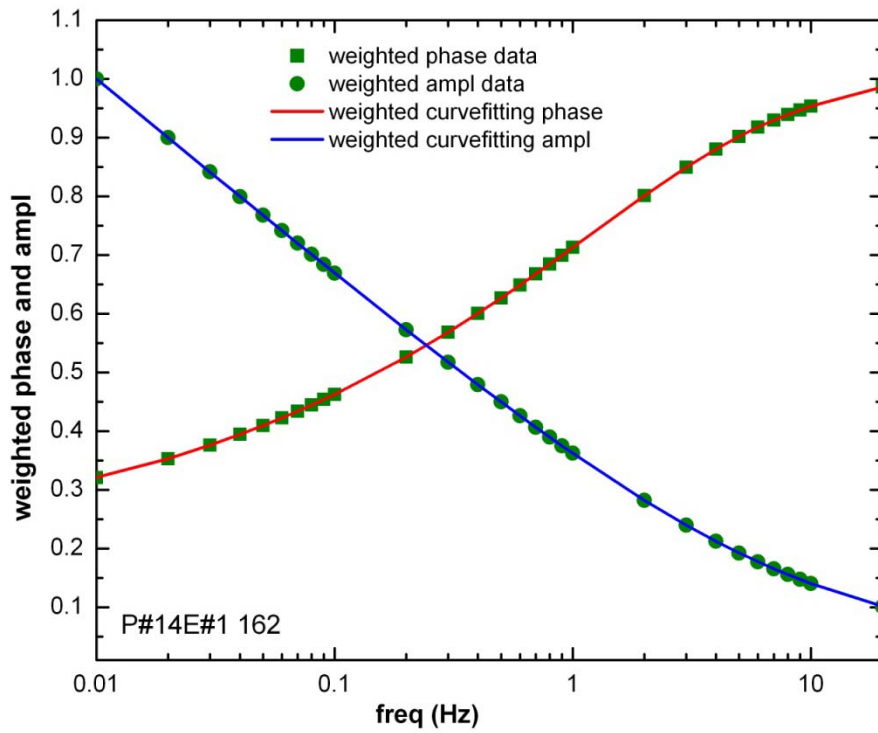


Figure 5. 15 Amplitude and phase used for curve fitting



**Figure 5. 16 Amplitude and phase used for curve fitting**



**Figure 5. 17 Curve-fitting the amplitude and phase data**

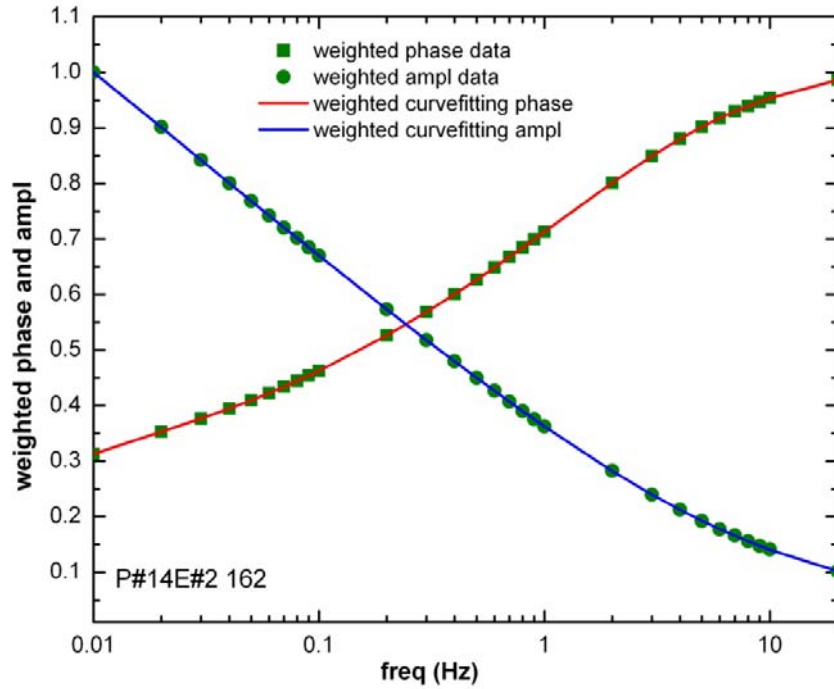


**Figure 5.18 Curve-fitting the amplitude and phase data**

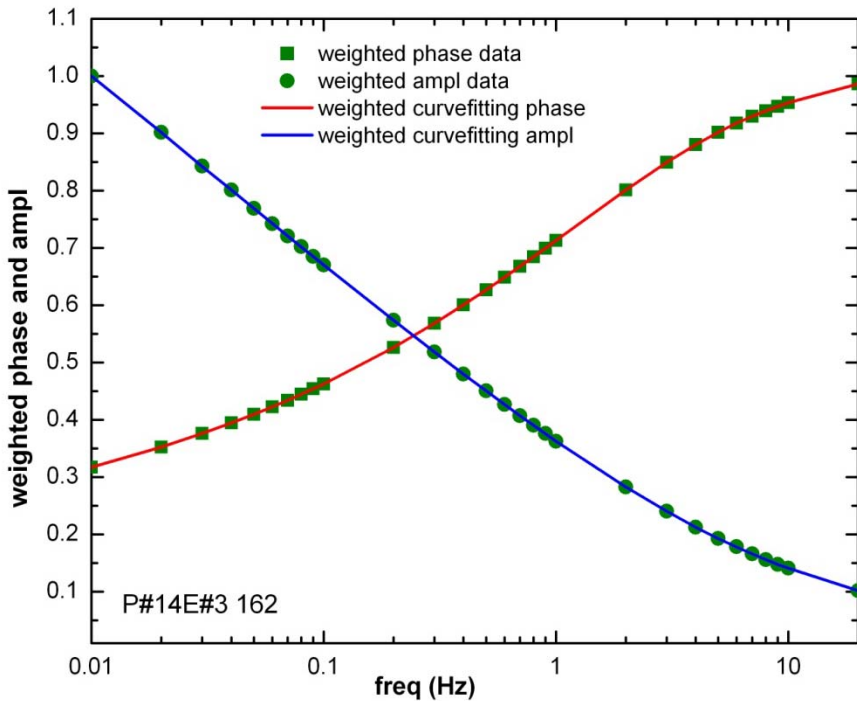


**Figure 5.19 Curve-fitting the amplitude and phase data**

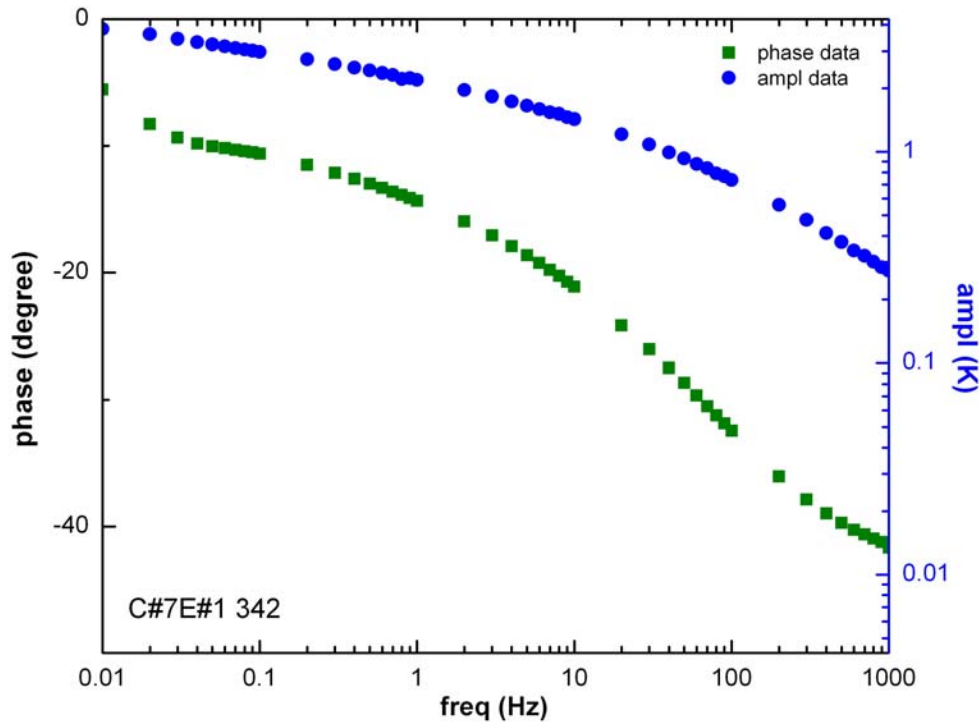


**Figure 5. 20 Amplitude and phase used for curve fitting**

(C#7E1 342 marked in the figure means that the studied data were obtained from Exp. #1 with sample C#7 whose resistance is  $342\ \Omega$ , similar for all figures thereafter)

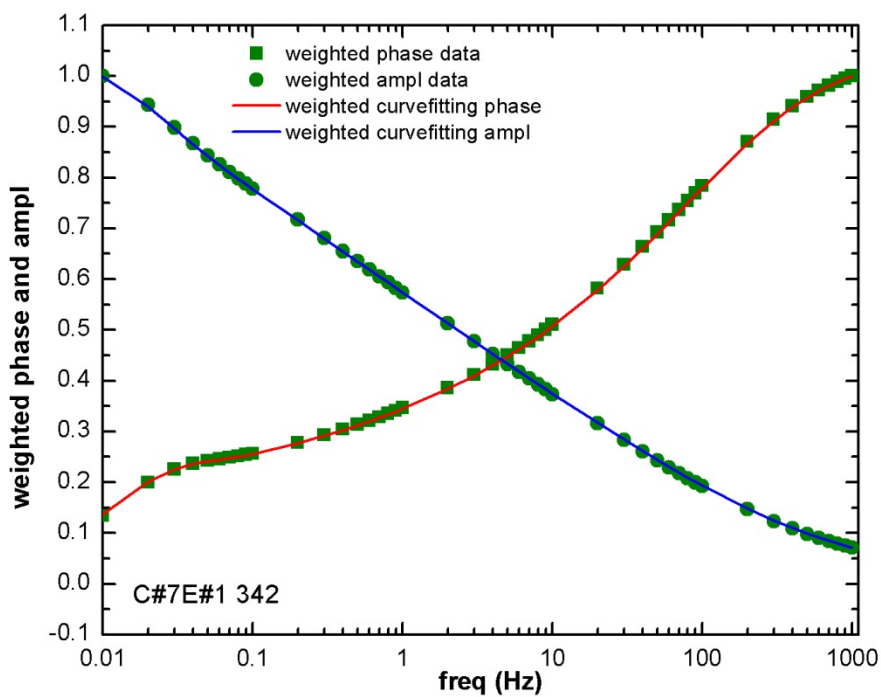


**Figure 5. 21 Curve-fitting the amplitude and phase data**

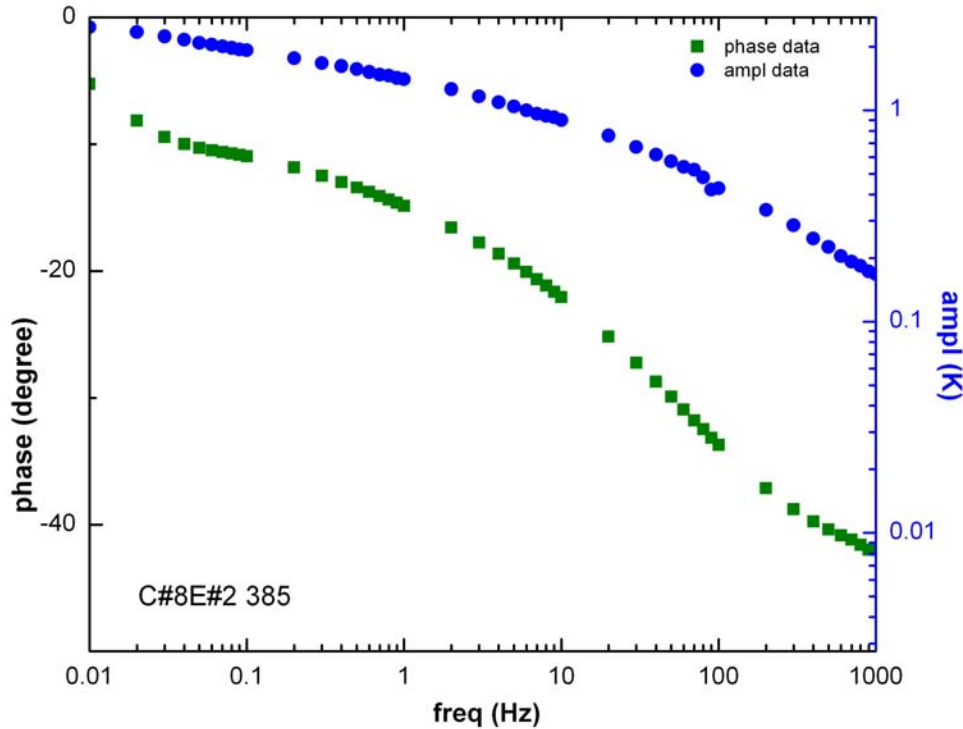


**Figure 5. 22 Amplitude and phase used for curve fitting**

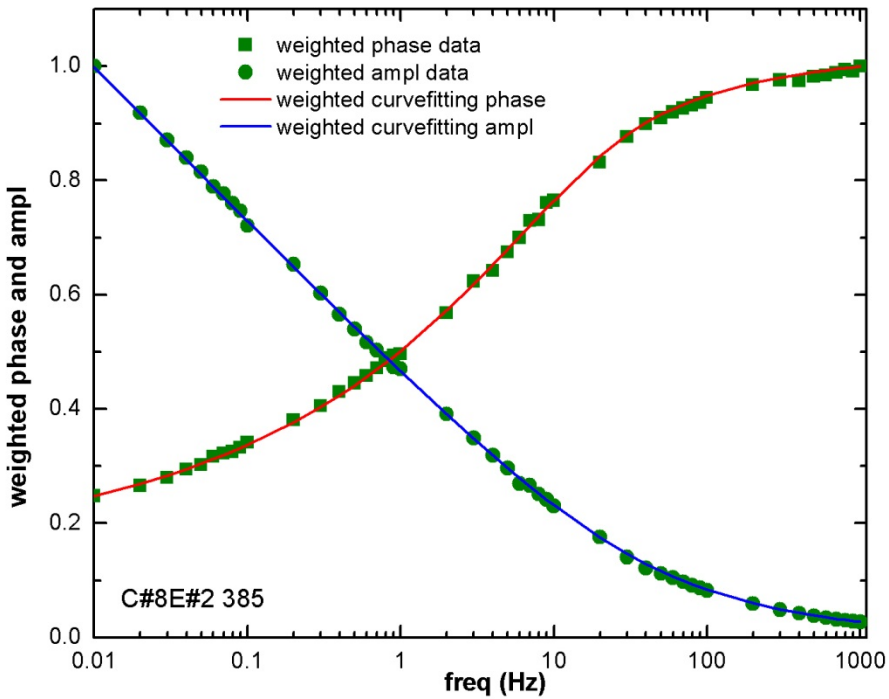


**Figure 5. 23 Curve-fitting the amplitude and phase data**

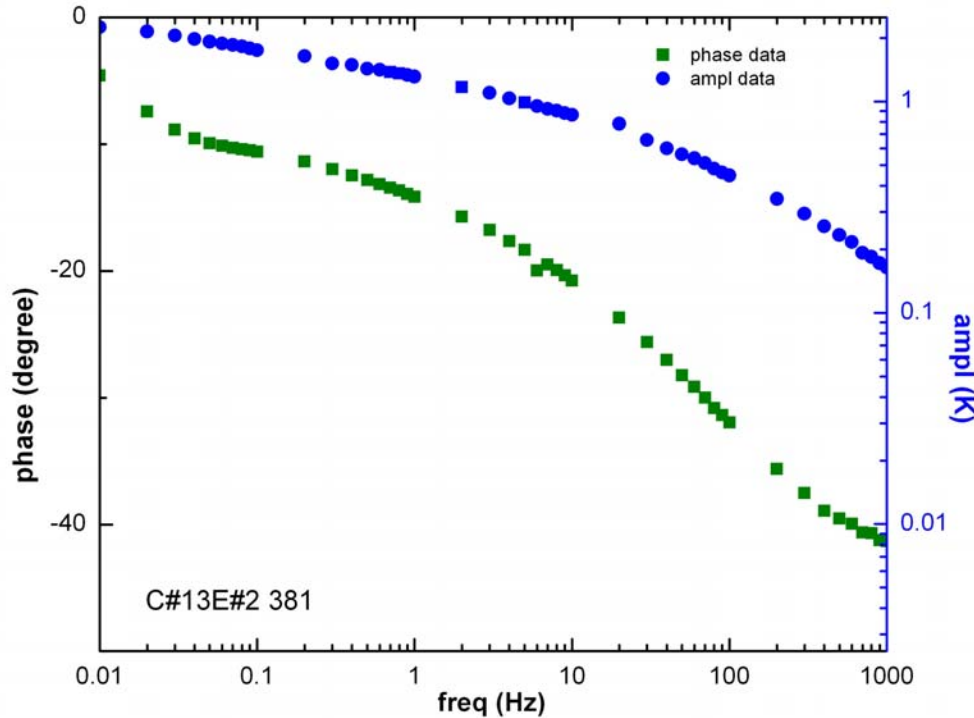


**Figure 5. 24 Amplitude and phase used for curve fitting**

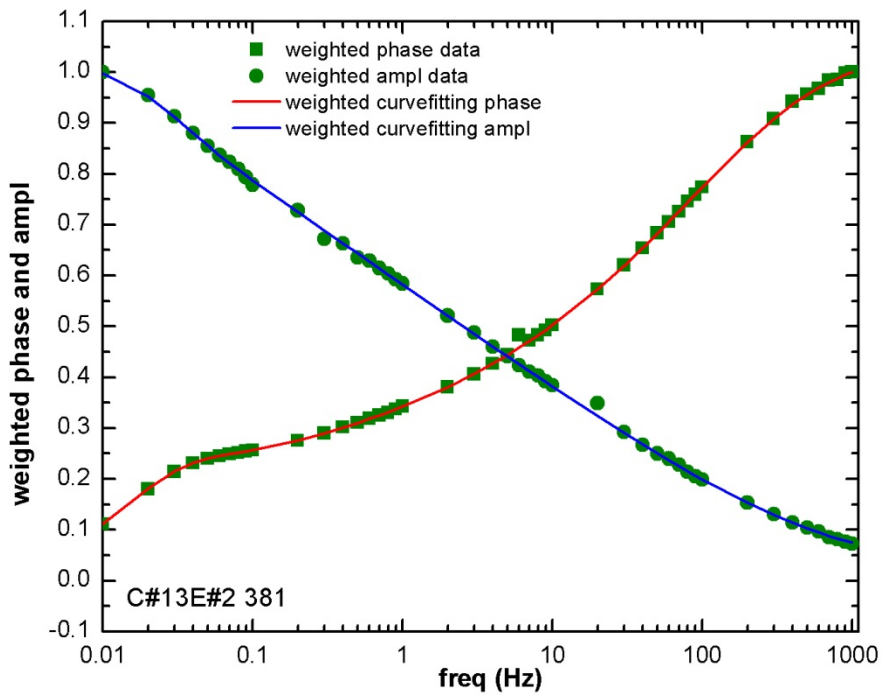


**Figure 5. 25 Curve-fitting the amplitude and phase data**

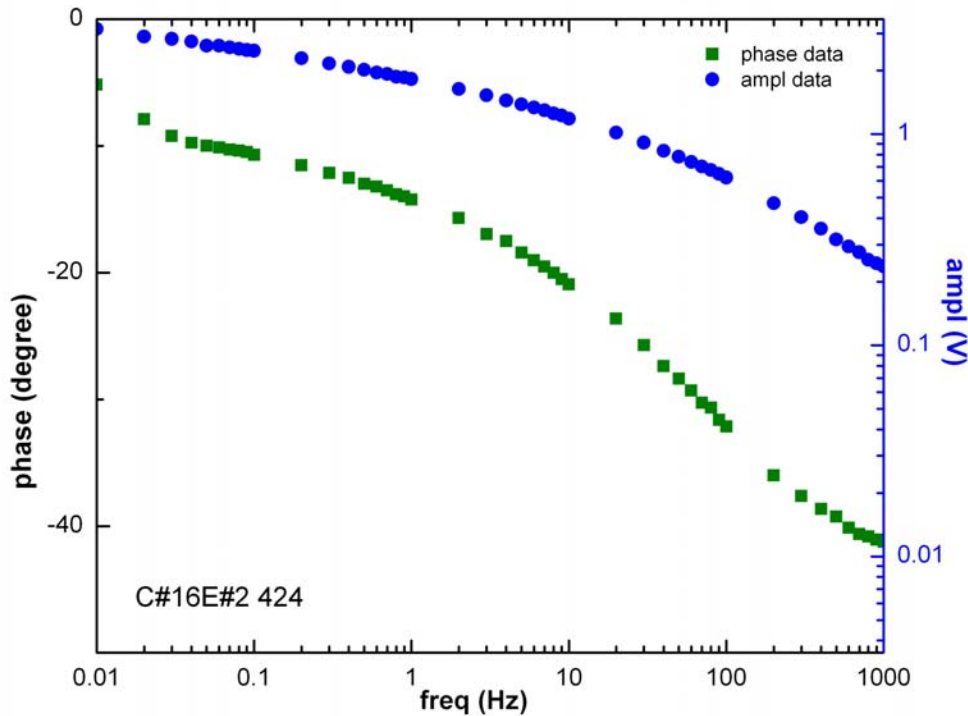


**Figure 5. 26 Amplitude and phase used for curve fitting**

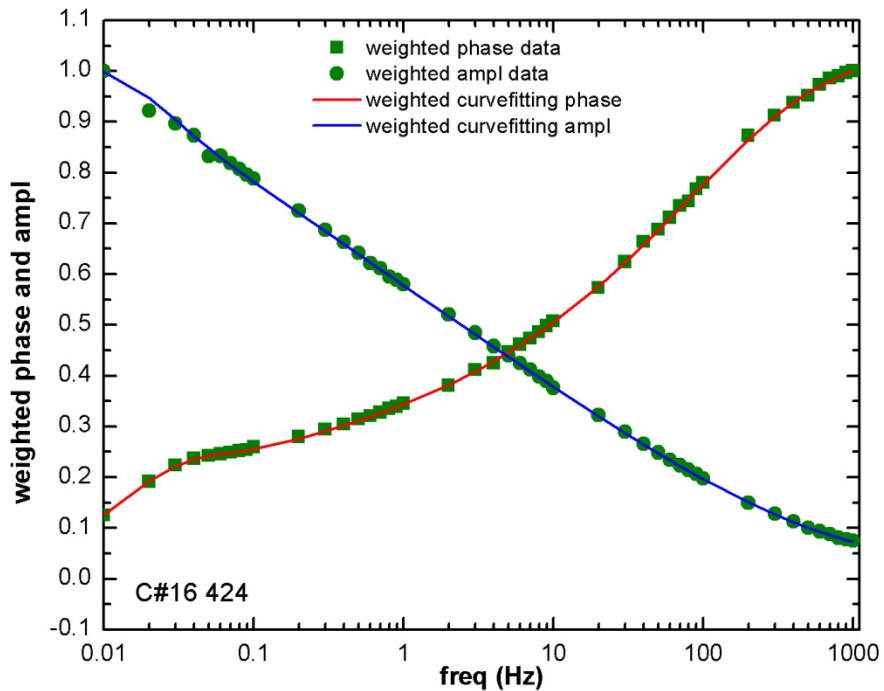
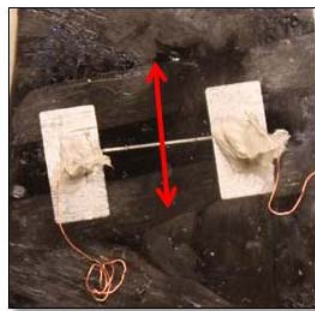
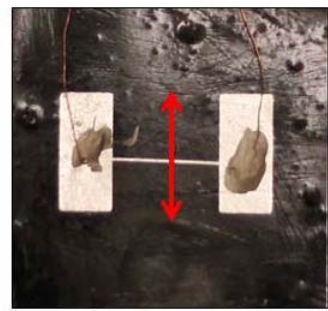


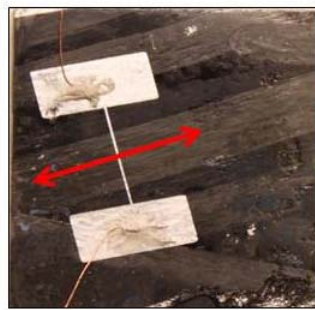
**Figure 5. 27 Curve-fitting the amplitude and phase data**



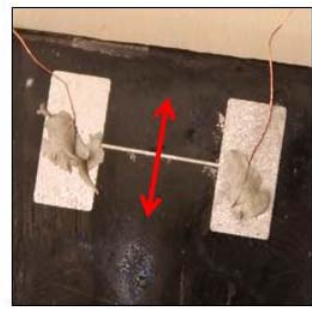
a) C#7



b) C#8



c) C#13



d) C#16

**Figure 5. 28 Photos of the surface of samples C#7, #8, #13 and #16**

# Chapter 6

## Conclusions and future work

### 6.1 Conclusions

The thermal property of composite materials has been a topic of interest for about a century. The two conventional approaches are based on the constituent components' properties of the composite materials and the steady-state heat transfer measurement. The  $3\omega$  technique to measure the thermal properties of isotropic materials, especially thin film materials, has been well established. However, using the  $3\omega$  method for measuring the thermal properties of anisotropic materials has been rarely studied. In this work, a measurement system consisting of the  $3\omega$  measurement technique and a two-dimensional anisotropic heat transfer model is developed to seek the anisotropic thermal properties of composite materials, specifically carbon-fiber/epoxy composite material.

The following accomplishments were achieved in this study:

1. Sample preparation procedures were developed for PMMA and carbon-fiber/epoxy composite samples. Before depositing platinum film, the work included cutting and polishing samples, applying epoxy layers for electrical isolation etc. Polishing and epoxy applying procedure needed to be repeated. Ultrasonic cleaning was necessary before applying epoxy layer each time. A platinum film was deposited on the surface of the sample with a mask under a sputtering target.

2. The  $3\omega$  experimental system was adapted and developed. A bridge circuit and a relatively complicated circuit containing a multiplying digital to analog converter and differential amplifiers were proposed and built. By comparison, the bridge circuit was adopted since it gives more accurate results. Computer control of the measurement system was realized.
3. System calibration was carried out by normal resister measurements where the platinum film was replaced with a regular resistor. The capacitance of cables in the circuit was determined by curve fitting the experimental phase and amplitude data and the model considering the effect of resistances and capacitances in the circuit.
4. An impedance analysis model was developed to convert the measured  $3\omega$  voltage data into temperature data, so that the temperature data can be used to compare with the model calculated temperature solution.
5. Smooth amplitude and phase data was collected from four PMMA and four carbon-fiber/epoxy composite samples over a wide frequency range. The results show great smoothness and consistence. It is observed that the value of voltage drop across the platinum film significantly affects the quality of the experimental data from PMMA samples.
6. An anisotropic two-dimensional heat conduction model was built and solved. A temperature solution in frequency domain with an affordable convergence rate was obtained based on the Green Function method. The effects of convection, sample thickness, sample width, and heater width were discussed.

7. A careful sensitivity analysis was carried out to study the feasibility of the multi-parameter inverse problem and the best frequency range to get useful data. It was concluded that the sensitivity coefficient of phase from the anisotropic model to the in-plane and through-thickness thermal conductivities are independent. The best frequency range for estimating in-plane thermal conductivity roughly falls in the region [50 Hz, 500 Hz] and the best frequency range for through-thickness thermal conductivity falls in the region [0.01 Hz, 0.1 Hz]. This enhances our confidence for obtaining the reasonable results through the  $3\omega$  measurement system since smooth and consistence data in these ranges can be obtained successfully.
8. An inverse parameter estimation model was established for seeking the unknown thermal properties. The anisotropic model applied for carbon fiber samples is sensitive to in-plane thermal conductivity, through-thickness thermal conductivity and thermal diffusivity, while the simplified isotropic model used for PMMA sample is only sensitive to thermal diffusivity. Both phase and amplitude data are utilized simultaneously for curve-fitting the sought-after parameters with a weighted least-square optimization method.
9. The measurement system was verified by successfully estimating the thermal diffusivity of PMMA samples to a value with a relative error of 0.46% to the handbook values.
10. The anisotropic thermal properties of four carbon-fiber/epoxy samples were obtained as  $k_x = 5.2 \sim 6.8 \text{ W/mK}$ ,  $k_y = 0.5 \sim 0.7 \text{ W/mK}$ . A comparison of the obtained thermal property result from this work and those from some

literatures is given. The obtained results generally agree with the results from literature.

Based on the achievements discussed above, the conclusion is that an effective measurement system consisting of the  $3\omega$  experimental technique and the two-dimensional heat transfer model for measuring the anisotropic thermal conductivities of bulk composite materials has been achieved.

## 6.2 Future work

The following are recommendations for future work.

1. Work is needed to improve the quality of experimental data at frequency range lower than 0.01 Hz and higher than 1000 Hz. See Section 4.6.1 for the reasons why collecting data at extremely high or low frequency range is especially challenging. Conducting the measurement at a vacuum environment could be used to minimize the disturbance from the noise in the surrounding.
2. Experiments on carbon-fiber/epoxy composite samples with platinum film deposited on more different directions relative to the fiber direction should be conducted to study the effect of the fiber orientation on the thermal properties.
3. If lab conditions allow, the photothermoelectric [1] technique may be also studied as an alternative measurement method to check the thermal property estimation results obtained from this work.
4. The measurement system proposed here consisting of the  $3\omega$  experimental technique and the two-dimensional heat conduction model may be effective for thin-film

material too. The experiment could start from 55  $\mu\text{m}$  thick anodic template Anidisc samples from Whatman, Inc. of 0.02  $\mu\text{m}$  pore diameter and  $\sim 30\%$  porosity, so that the anisotropic thermal conductivity estimation result could be compared with that of Borca's [101].

5. In this work, the heat capacity of the platinum heater is neglected, which is reasonable at low frequencies where the penetration depth is large. When the frequency turns larger, the heat capacity may shift the phase of temperature. Therefore, at high frequencies a more comprehensive heat conduction model considering the bulk properties for the density and the specific heat of the platinum film may be needed.

6. The thermal boundary resistance between the heater and the sample is neglected in this work. More experimental and theoretical work may be carried on to study its effect on the amplitude and phase of the average temperature rise of the heater.

# Reference

- [1] Cfaser haarrp, [online image], German Wikipedia, original upload 29. Okt 2004 by Anton (selfmade), retrieved from <[http://en.wikipedia.org/wiki/File:Cfaser\\_haarrp.jpg](http://en.wikipedia.org/wiki/File:Cfaser_haarrp.jpg)> June 18, 2011.
- [2] Raw carbon fiber thread, [online image], retrieved from <<http://www.howstuffworks.com/framed.htm?parent=carbon-fiber-oil-crisis.htm&url=http://www.dreamstime.com/>>, June 18, 2011.
- [3] Kohlenstofffasermatte, German Wikipedia, original upload 17. Apr 2005 by Hadhuey (selfmade), [online image], retrieved from <<<http://en.wikipedia.org/wiki/File:Kohlenstofffasermatte.jpg>> .
- [4] Today industries, Inc, Market Research Report: Strategic Business Expansion of Carbon Fiber, Torayca" Toray Industries press release (2005), retrieved from <[http://web.archive.org/web/20070204052035/http://www.toray.com/ir/press/pdf/050412\\_press.pdf](http://web.archive.org/web/20070204052035/http://www.toray.com/ir/press/pdf/050412_press.pdf)>.
- [5] H. B. Shim, M. K. Seo, M, and S. J. Park, Thermal conductivity and mechanical properties of various cross-section types carbon fiber-reinforced composites, Journal of Materials Science, 37 (2002) 1881-1885.
- [6] D. P. H. Hasselman, H. K. Y. Donaldson, and J. R. J. Thomas, Effective thermal conductivity of uniaxial composite with cylindrically orthotropic carbon fibers and interfacial thermal barrier, Journal of Composite Materials, 27 (1993) 637-644
- [7] D. P. H. Hasselman, K. Y. Donaldon, and J. R. Thomas, Effective thermal conductivity of uniaxial composite with cylindrically orthotropic carbon fibers and

- thermal barrier, Journal of Composite Materials, 27 (1993) 1353-1365.
- [8] A. Dasgupta, and R. K. Agarwal, Orthotropic thermal conductivity of plain-weave fabric composites using a homogenization technique, Journal of Composite Materials, 26 (1992) 2736-2758.
- [9] G. S. Springer, and S.W.Tsai, Thermal conductivities of unidirectional materials, Journal of Composite Materials, 1 (1967) 166-173.
- [10] J. D. Thornburgh, and C. D. Pears, Prediction of the thermal conductivity of filled and reinforced plastics, ASME paper 65-WA/HT-4 (1965).
- [11] J. P. Harris, B. Yates, J. Batchelor, and P. J. Carrington, The thermal conductivity of Kevlar fibre-reinforced composites, Journal of Materials Science, 17 (1982) 2925-2931.
- [12] M. W. Pilling, B. Yates, M. A. Black, and P. Tattersall, The thermal conductivity of carbon fibre-reinforced composites, Journal of Materials Science, 14 (1979) 1326-1328.
- [13] J. J. Brennan, L. D. Bentsen, and D. P. H. Hasselmann, Determination of the thermal conductivity and diffusivity of thin fibres by the composite method, Journal of Materials Science, 17 (1982) 2337-2342.
- [14] A. J. Whittaker and R. Taylor, Thermal transport properties of carbon-carbon fibre composites III. Mathematical Modelling, Proceedings: Mathematical and Physical Sciences, 430 (1990) 199-211.
- [15] J. T. Mottram and R. Taylor, Thermal conductivity of fibre-phenolic resin composites part II: numerical evaluation, Composites Science and Technology, 29 (1987) 211-232.
- [16] Z. Hashin, Analysis of composite material—a survey, Journal of Applied Mechanical, 50 (1983) 481-505.

- [17] L. E. Nielsen, The thermal and electrical conductivity of two-phase systems, and engineering chemistry fundamentals, Industrial and Engineering Chemistry Fundamentals, 13 (1974) 17-20.
- [18] J. T. Mottram and R. Taylor, Thermal conductivity of fibre-phenolic resin composites part II: numerical evaluation, Composites Science and Technology, 29 (1987) 211-232.
- [19] D. A. G. Bruggemann, Annals of Physics, 24 (1935) 636-679.
- [20] J. Ashton, J. Halpin, and P. Petit, Primer on Composite Materials: Analysis, Technomic publishing company, Stamford, Conn. (1969).
- [21] A. Krach, and S. G. Advani, Influence of void shape, void volume and matrix anisotropy on effective thermal conductivity of a three-phase composite, Journal of Composite Materials, 30 (1996) 933-946.
- [22] M. Zou, B. Yu, and D. Zhang, An analytical solution for transverse thermal conductivities of unidirectional fibre composites with thermal barrier, Journal of Physics D: Applied Physics, 35 (2002) 1867-1874.
- [23] R. Pichumani, Evaluation of thermal conductivities of disordered composite media using a fractal model, Journal of Heat Transfer, 121 (1999) 163.
- [24] R. Pitchumani, and S. C. Yao, Correlation of thermal conductivities of unidirectional fibrous composites using local fractal techniques, Journal of Heat Transfer, 113 (1991) 788.
- [25] T. Behzad, M. Sain, Measurement and prediction of thermal conductivity for hemp fiber reinforced composites, Polymer Engineering and Science, 47 (2007) 977-983.

- [26] S. Han, J. Lin, Y. Yamaha, D. Chung, Enhancing the thermal conductivity and compressive modulus of carbon fiber polymer-matrix composites in the through-thickness direction by nanostructuring the interlaminar interface with carbon black, *Carbon*, 46 (2008) 1060-1071.
- [27] H.-B. Shim, M.-K. Seo, and S.-J. Park, Thermal conductivity and mechanical properties of various cross-section types carbon fiber-reinforced composites, *Journal of Materials Science*, 37 (2002) 1881-1885.
- [28] B. Garnier, D. Delaunay, and J. V. Beck, Estimation of thermal properties of composite materials without instrumentation inside the samples, *International Journal of Thermophysics*, 13 (1992) 1097-1111.
- [29] R. D. Sweeting, "Measurement of thermal conductivity for fibre-reinforced composites", *Composites Part A: Applied Science and Manufacturing*, 35 (2004) 933-938.
- [30] G. Kalaprasad, P. Pradeep, G. Mathew, C. Pavithran, and S. Thomas, Thermal conductivity and thermal diffusivity analyses of low-density polyethylene composites reinforced with sisal, glass and intimately mixed sisal/glass fibres, *Composites Science and Technology*, 60 (2000) 2967-2977.
- [31] R. Agrawal, N. S. Saxena, M. S. Sreekala, and S. Thomas, Effect of treatment on the thermal conductivity and thermal diffusivity of oil-palm-reinforced phynolformaldehyde composites, *Journal of Polymer Science: Part B: Polymer Physics*, 38 (2000) 916-921.
- [32] R. Mangal, N. S. Saxena, M. S. Sreekala, S. Thomas, and K. Singh, Thermal properties of pineapple leaf fiber reinforced composites, *Materials Science and Engineering A*, 339 (2003) 281-285.

- [33] E. Karawacki, B. M. Suleiman, Izhar ul-Haq, Bui-Thi Nhi , An extension to the dynamic plane source technique for measuring thermal conductivity, thermal diffusivity, and specific heat of dielectric solids, *Review of Scientific Instruments*, 63 (1992) 4390.
- [34] S. E. Gustafsson, Transient plane source techniques for thermal conductivity and thermal diffusivity measurement of solid material, *Review of Scientific Instruments*, 62 (1991) 797.
- [35] E. Karawacki and B. M. Suleiman, Dynamic plane source technique for simultaneous determination of specific heat, thermal conductivity and thermal diffusivity of metallic samples, *Measurement Science and Technology*, 2 (1991) 744.
- [36] L. Sassi, F. Mzali, A. Jemnia , and S. B. Nasrallah, Hot-wire method for measuring effective thermal conductivity of porous media, *Journals of Porous Media*, 8 (2005) 97-114.
- [37] J. J. Healy, J. J. de Groot and J. Kestin, The theory of the transient hot-wire method for measuring thermal conductivity, *Physica B: Condensed Matter*, 82 (1976) 392-408.
- [38] P. Prelovsek and B. Uran, Generalised hot wire method for thermal conductivity measurements, *Journal of Physics E: Scientific Instruments*, 17 (1984) 674.
- [39] J. K. Horrocks and E. McLaughlin, Non-steady-state measurements of the thermal conductivities of liquid polyphenyls, *Proceedings of the royal society of London. Series A, Mathematical and Physical Sciences*, 273 (1963) 259-274.
- [40] O. Sandberg, P. Andersson, and G. Backstrom, Heat capacity and thermal conductivity from pulsed wire probe measurements under pressure, *Journal of Physics E : Scientific Instruments* , 10 (1977) 474.

- [41] S. E. Gustafsson, Ernest Karawacki, Transient hot strip probe for measuring thermal properties of insulating solids and liquids, *Review of Scientific Instruments*, 54 (1983) 744-747.
- [42] S. E. Gustafsson, E. Karawacki and M. N. Khan, Transient hot-strip method For simultaneously measuring thermal conductivity and thermal diffusivity of solids and fluids, *Journal of Physics D: Applied Physics*, 12 (1979) 1411.
- [43] Torgrim Log, Transient Hot-Strip Method for Simultaneous Determination of Thermal Conductivity and Thermal Diffusivity of Refractory Materials, *Journal of the American Ceramic Society*, 74 (1991) 650-653.
- [44] O. M. Corbino, Thermal oscillations in lamps of thin fibers with alternating current flowing through them and the resulting effect on the rectifier as a result of the presence of even-numbered harmonics, *Physikalische Zeitschrift*, 11 (1910) 413-417.
- [45] O. M. Corbino, Periodic resistance changes of fine metal threads, which are brought together by alternating streams as well as deduction of their thermo characteristics at high temperatures, *Physikalische Zeitschrift*, 12 (1911) 292-295.
- [46] Louis A. Rosenthal, Thermal response of bridgewires used in electroexplosive devices, *Review of Scientific Instruments*, 32 (1961) 1033-1036.
- [47] L. R. Holland, Physical properties of titanium III the specific heat, *Journal of Applied Physics*, 34 (1963) 2350-2357.
- [48] N.O. Birge and S.R. Nagel, Specific-heat spectroscopy of the glass transition, *Physical Review Letters*, 54 (1985) 2674–2677.
- [49] N.O. Birge and S.R. Nagel, Wide-frequency specific heat spectrometer, *Review of Scientific Instruments*, 58 (1987) 1464–1470.

- [50] N.O. Birge, P.K. Dixon, and N. Menon, Specific heat spectroscopy: origins status and applications of the  $3\omega$  method, *Thermochimica ACTA*, 304/305 (1997) 51–66.
- [51] R. Frank, V. Drach and J. Fricke, Determination of thermal conductivity and specific heat by a combined  $3\omega$ /decay technique, *Review of Scientific Instruments*, 64 (1993) 760–765.
- [52] P. K. Dixon and S. R. Nagel, Frequency-dependent specific heat and thermal conductivity at the glass transition in o-terphenyl mixtures, *Physical Review Letters*, 61 (1988) 341–344.
- [53] J. K. Nielsen and J. C. Dyre, Fluctuation-dissipation theorem for frequency-dependent specific heat, *Physical Review B: Condensed Matter and Materials Physics*, 54 (1996) 15754.
- [54] D. Oxtoby, Generalized hydrodynamics and specific heat spectroscopy of the glass transition, *Journal of Chemical Physics*, 85 (1986) 1549.
- [55] D. G. Cahill and R. O. Pohl, Thermal conductivity of amorphous solids above the plateau, *Physical Review B: Condensed Matter and Materials Physics*, 35 (1987) 4067–4073.
- [56] D. G. Cahill, Thermal conductivity measurement from 30 to 750 K: the  $3w$  method, *Review of Scientific Instruments*, 61 (1990) 802.
- [57] D. G. Cahill, M. Katiyar, and J. R. Abelson, Thermal conductivity of a-Si:H thin films, *Physical Review B: Condensed Matter and Materials Physics*, 50 (1994) 6077.
- [58] D. G. Cahill, S. K. Watson, and R. O. Pohl, Lower limit to the thermal conductivity of disordered crystals, *Physical Review B: Condensed Matter and Materials Physics*, 46 (1992) 6131–6140.

- [59] J. B. Hou, X. W. Wang, and P. W. Vellelacheruvu, Thermal characterization of single-wall carbon nanotube bundles using the self-heating  $3\omega$  technique, *Journal of Applied Physics*, 100 (2006) 124314 .
- [60] L. W. Wang, D. W. Tang, X. H. Zheng, Simultaneous determination of thermal conductivities of thin film and substrate by extending  $3\omega$ -method to wide-frequency range, *Applied Surface Science*, 253 (2007) 9024-9029.
- [61] P. E. Hopkins, L. M. Phinney, “Thermal Conductivity Measurements on Polycrystalline Silicon Microbridges Using the  $3\omega$  Technique”, *Journal of Heat Transfer*, 131 (2009) 043201.
- [62] S. M. Lee and S. I. Kwun, Heat capacity measurement of dielectric solids using a linear surface heater: application to ferroelectrics, *Review of Scientific Instruments*, 65 (1994) 966–970.
- [63] S. M. Lee and D.G. Cahill, Heat transport in thin dielectric film, *Journal of Applied Physics*, 81 (1997) 2590–2595.
- [64] T. Yamane, N. Nagai, S. Katayama and M. Todoki, Measurement of thermal conductivity of silicon dioxide thin films using a  $3\omega$  method, *Journal of Applied Physics*, 91 (2002) 9772–9776.
- [65] C.E. Raudzis, F. Schatz and D. Wharam, Extending the  $3\omega$  method for thin-film analysis to high frequencies, *Journal of Applied Physics*, 93 (2003) 6050–6055.
- [66] B.W. Olson, S. Graham and K. Chen, A practical extension of the  $3\omega$  method to multilayer structures, *Review of Scientific Instruments*, 76 (2005) 1–7.

- [67] J. Alvarez-Quintana and J. Rodriguez-Viejo, Extension of the  $3\omega$  method to measure the thermal conductivity of thin films without a reference sample, *Sensors Actuators A*, 142 (2008) 232–236.
- [68] T. Borca-Tasciuc, A. R. Kumar, G. Chen, Data reduction in  $3\omega$  method for thin-film thermal conductivity determination, *Review of Scientific Instruments*, 72 (2001) 2139–2147.
- [69] K. D. Harris, D. Vick, E. J. Gonzalez, T. Smy, K. Robbie, M. J. Brett, Porous thin films for thermal barrier coatings, *Surface & Coatings Technology*, 138 (2001) 185-191.
- [70] J. H. Kim, A. Feldman, D. Novotny, Application of the three omega thermal conductivity measurement method to a film on a substrate of finite thickness, *Journal of Applied Physics*, 86 (1999) 3959-3963.
- [71] S. W. Kim, H. Yu, C. H. Kang, S. H. Lee, and J. C. Kim, Thermal conductivity of chalcogenide As<sub>2</sub>S<sub>3</sub> thin films, *International Journal of Thermophysics*, 25 (2004) 1505–1517.
- [72] S. W. Kim, C. H. Kang, S. H. Kahn, S. H. Lee and J. C. Kim, Photoinduced change of thermophysical properties of chalcogenide As<sub>2</sub>S<sub>3</sub> thin films, *International Journal of Thermophysics*, 25 (2004) 1871-1879.
- [73] W. L. Liu, M. Shamsa, I. Calizo, A. A. Balandin, V. Ralchenko, A. Popovich, and A. Saveliev, Thermal conduction in nanocrystalline diamond films: effects of the grain boundary scattering and nitrogen doping, *Applied Physics Letters*, 89 (2006) 171915.
- [74] P. B. Kaul, K. A. Day, A. R. Abramson, Application of the three omega method for the thermal conductivity measurement of polyaniline, *Journal of Applied Physics*, 101 (2007) 2714650.

- [75] S. P. Gurrum, W. P. King, Y. K. Joshi, K. Ramakrishna, Size effect on the thermal conductivity of thin metallic films investigated by scanning joule expansion microscopy, Journal of Heat Transfer-Transactions of the ASME, 130 (2008) 082403.
- [76] X. Liu, J. L. Feldman, D. G. Cahill, R. S. Crandall, N. Bernstein, D. M. Photiadis, M. J. Mehl, and D. A. Papaconstantopoulos , High Thermal Conductivity of a Hydrogenated Amorphous Silicon Film, Physical Review Letters, 102 (2009) 035901.
- [77] J. Zhu, D. W. Tang, W. Wang, J. Liu, K. W. Holub, R. G. Yang, Ultrafast thermoreflectance techniques for measuring thermal conductivity and interface thermal conductance of thin films, Journal of Applied Physics, 108 (2010) 3504213.
- [78] H. S. Yang, D. G. Cahill, X. Liu , J. L. Feldman , R. S. Crandall , B. A. Sperling and J. R. Abelson , Anomalously high thermal conductivity of amorphous Si deposited by hot-wire chemical vapor deposition, Physical Review B, 81 (2010) 104203.
- [79] R. P. Bhatta, S. Annamalai, R. K. Mohr, Marek Brandys, Ian L. Pegg, and Biprodas Dutta, High temperature thermal conductivity of platinum microwire by  $3\omega$  method, Review of Scientific Instrument, 81 (2010) 114904.
- [80] R. Venkatasubramanian , Lattice thermal conductivity reduction and phonon localizationlike behavior in superlattice structures, Physical Review B, 61 (2000) 3091–3097.
- [81] S. T. Huxtable, A. R. Abramson, and C. L. Tien, A. Majumdar, C. LaBounty, X. Fan, G. Zeng, J. E. Bowers, A. Shakouri, and E. T. Croke, Thermal conductivity of Si/SiGe and SiGe/SiGe superlattices, Applied Physics Letters, 80 (2002) 1455693.

- [82] B. Yang, W. L. Liu, J. L. Liu, K. L. Wang, and G. Chen, Measurements of anisotropic thermoelectric properties in superlattices, *Applied Physics Letters*, 81 (2002) 3588.
- [83] S.R. Choi, J. Kim and D. Kim,  $3\omega$  method to measure thermal properties of electrically conducting small-volume liquid, *Review of Scientific Instruments*, 78 (2007) 1–6.
- [84] O. Bourgeois, T. Fournier, and J. Chaussy, Measurement of the thermal conductance of silicon nanowires at low temperature, *Journal of Applied Physics*, 101 (2007) 2400093.
- [85] M. N. Ou, T. J. Yang, S. R. Harutyunyan, Y. Y. Chen, C. D. Chen, and S. J. Lai, Electrical and thermal transport in single nickel nanowire, *Applied Physics Letters*, 92 (2008) 2839572.
- [86] J. Hou, X. Wang, C. Liu, and H. Cheng, Development of photothermal-resistance technique and its application to thermal diffusivity measurement of single-wall carbon nanotube bundles, *Applied Physics Letters*, 88 (2006) 181910.
- [87] P. B. Kyoo, P. Jaesung, and K. Dongsik, Note: Three-omega method to measure thermal properties of subnanoliter liquid samples, *Review of Scientific Instruments*, 81 (2010) 066104.
- [88] E. Yusibani, P. L. Woodfield, M. Fujii, K. Shinzato, X. Zhang, and Y. Takata, Application of the three-omega method to measurement of thermal conductivity and thermal diffusivity of hydrogen gas, *International Journal of Thermophysics*, 30 (2009) 397–415.
- [89] B. Yang and Z. H. Han, Temperature-dependent thermal conductivity of nanorod-based nanofluids, *Applied Physics Letters*, 89 (2006) 083111.

- [90] F. Chen, J. Shulman, Y. Xue, C.W. Chu and G.S. Nolas, Thermal conductivity measurement under hydrostatic pressure using the  $3\omega$  method, *Review of Scientific Instruments*, 75 (2004) 4578–4584.
- [91] D. W. Oh, A. Jain, J.K. Eaton, K.E. Goodson, and J.S. Lee, Thermal conductivity of aluminum oxide nanofluids using the  $3\omega$  method, *ASME International Mechanical Engineering Congress and Exposition*, (2006) IMECE2006-14196.
- [92] C. D. W. Jones, F. Pardo, C. S. Pai, J. E. Bower, J. F. Miner, F. P. Klemens, R. A. Cirelli, E. J. Ferry, J. A. Taylor, M. R. Baker, B. S. Dennis, W. M. Mansfield, A. Kornblit, R. C. Keller, J. V. Gates, and A. P. Ramirez,  $3\omega$  thermal conductivity measurements of thin film dielectrics on silicon for use in cantilever-based IR imaging, *Journal of Vacuum Science & Technology B*, 27 (2009) 1207.
- [93] T. Tong and A. Majumdar, Reexamining the 3-omega technique for thin film thermal conductivity characterization, *Review of Scientific Instruments*, 77 (2006) 1–9.
- [94] K. D. Cole, Steady-periodic Green's functions and thermal-measurement applications in rectangular coordinates, *Journal of Heat Transfer*, 128 (2006) 709-716.
- [95] H. Wang and M. Sen, Analysis of the 3-omega method for thermal conductivity measurement, *International Journal of Heat and Mass Transfer*, 52 (2009) 2102-2109.
- [96] A. Jacquot, B. Lenoir, A. Dauscher, M. Stölzer, and J. Meusel, Numerical simulation of the  $3\omega$  method for measuring the thermal conductivity, *Journal of Applied Physics*, 91 (2002) 4733.
- [97] L. Qiu, D. W. Tang, X. H. Zheng, and G. P. Su, The freestanding sensor-based  $3\omega$  technique for measuring thermal conductivity of solids: principle and examination, *Review of Scientific Instruments*, 82 (2011) 045106.

- [98] J. L. Battaglia, C. Wiemer and M. Fanciulli, An accurate low-frequency model for the  $3\omega$  method, *Journal of Applied Physics*, 101 (2007) 1–5.
- [99] B. Y. Tsui, C. C Yang, and K. L. Fang, Anisotropic thermal conductivity of nanoporous silica film, *IEEE Transactions on Electron Devices*, 51 (2004) 20-27.
- [100] A.R. Abramson, W.C. Kim, S.T. Huxtable, H. Yan, Y. Wu, A. Majumdar, C.-L. Tien, and P.Yang, Fabrication and characterization of a nanowire/polymer-based nanocomposite for a prototype thermoelectric device, *Journal of Microelectromechanical Systems*, 13 (2004) 505-513.
- [101] T. Borca-Tasciuc, G. Chen, Anisotropic thermal properties of nanochanneled alumina templates, *Journal of Applied Physics*, 97 (2005) 084303.
- [102] M. N. Ozisik, *Heat Conduction*, John Wiley and Sons, New York, 1985
- [103] K. D. Cole, J. V. Beck, A. Haji-Sheikh, and B. Litkouhi, *Heat Conduction Using Green's Functions*, 2nd edition, Taylor and Francis, New York, 2010.
- [104] K. D. Cole, Steady-periodic Green's functions and thermal-measurement applications in rectangular coordinates, *Journal of Heat Transfer*, 128 (2006) 709-716
- [105] A. Haji-Sheikh, Y. S. Hong, S. M. You, and J. V. Beck, Sensitivity analysis for thermophysical property measurements using the periodic method, *Journal of Heat Transfer*, 120 (1998) 568 -576.
- [106] J. V. Beck, and K. J. Arnold, *Parameter Estimation in Engineering and Science*, Wiley, NY, 1997.
- [107] Y. S. Touloukian, Thermophysical properties of matter, Purdue University, the TPRC data series, 10 (1970) 602.

- [108] R. C. Wetherhold, J. Wang, Difficulties in the theories for predicting transverse thermal conductivity of continuous fiber composites, *Journal of Composite Materials*, 28 (1994) 1491-1498.
- [109] Personal communication from Norman Newhouse, Lincoln Composites, Lincoln, NE, 68503.

# Appendix A.

## Experimental results from Sample P#9, #10 and #14

**Sample P#9** Figures A.1-A.2 show the amplitude and phase data of  $U_{AB}^{3\omega}$  collected from Exp. #1 under  $U_{CD}=5$  V and 3.5 V of PMMA sample P#9 whose electrical resistance is 225  $\Omega$  at room temperature. It can be seen both amplitude and phase data look lousy comparing to the rather nicer data from sample P#8. The possible reason is that the large voltage occupied by the platinum film due to small resistance of  $R_A$  ( $R_A = 10 \Omega$ ) causes deformation of the thin film so that the sensitivity of the film on the weak  $3\omega$  signal is reduced.

Fig. A.3 shows the amplitude of temperature  $\Delta T(2\omega)$  converted from  $U_{AB}^{3\omega}$  using the impedance analysis model. It can be seen that the magnitude of temperature rise is slightly larger than 3 K at frequency 0.01 Hz (the first frequency point the measurement starts with), while the temperature rise of the experiments with sample P#8 at frequency 0.01Hz is between 2 K and 3 K. Based on these temperature data including those relating to the samples P#10 and #14, it is reasoned that the proper temperature rise range might be 1.5-3 K, under which the  $3\omega$  signal caused by the temperature response is large enough for lock-in amplifier to be able to detect and not too large to bring deformation of the PMMA sample.

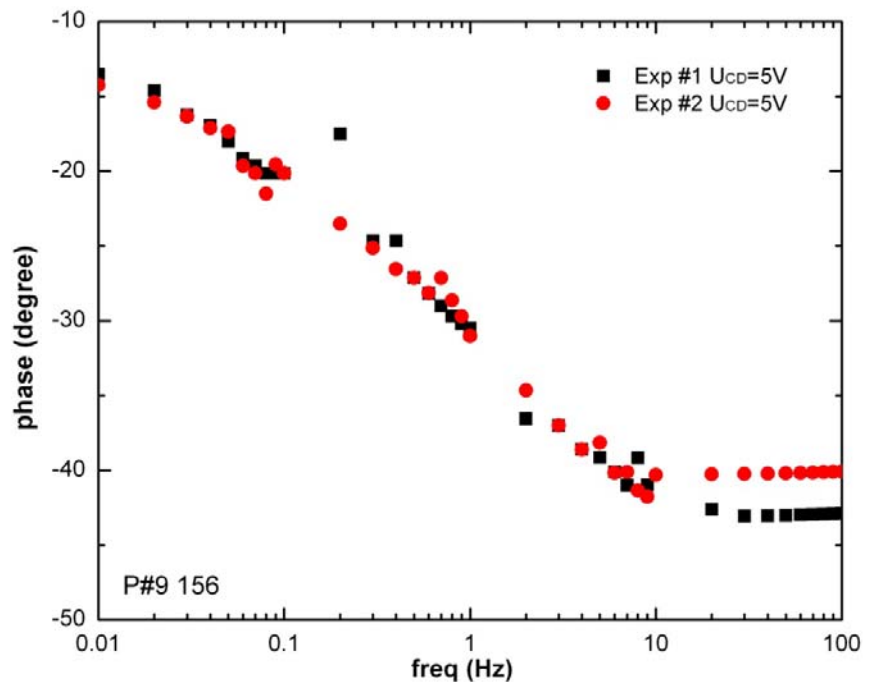
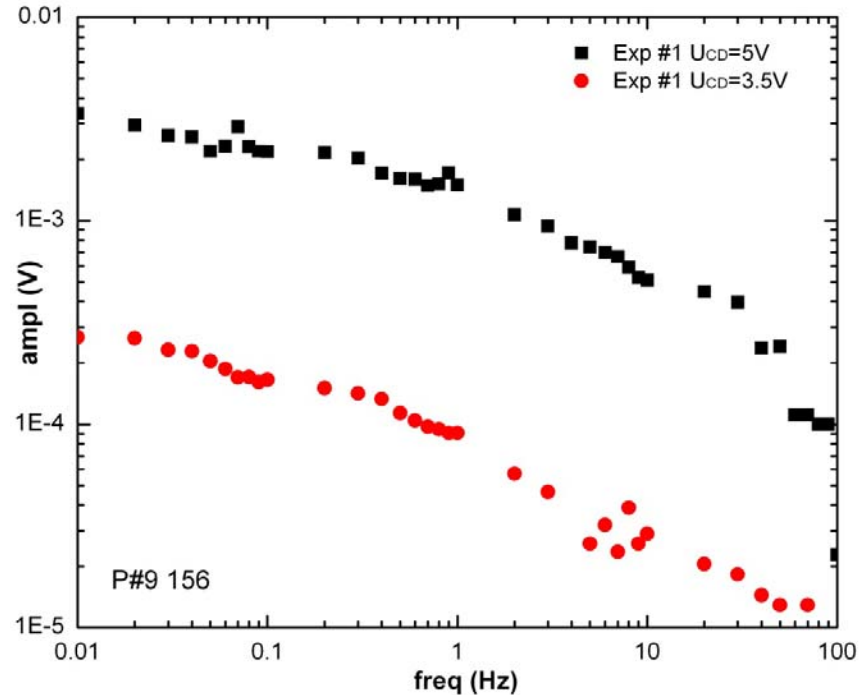
**Sample P#10** Figures A.4-A.6 show the amplitude and phase data of  $U_{AB}^{3\omega}$  collected from Exp. #1, #2 and #3 under different  $U_{CD}$  of PMMA sample P#10 whose electrical resistance is  $154 \Omega$  at room temperature. Both the amplitude and phase data from Exp. #1 and 2 show great smoothness, especially the phase data from the two experiments are consistent with each other very well. In comparison, the data from Exp. #3 are more noisy, which might be because the voltage across the platinum is so large that platinum film deformation occurs since in this case  $U_{CD}$  is relatively large ( $U_{CD}=5$  V), and the resistance value of  $R_A$  ( $R_A=5$  V) is relatively small.

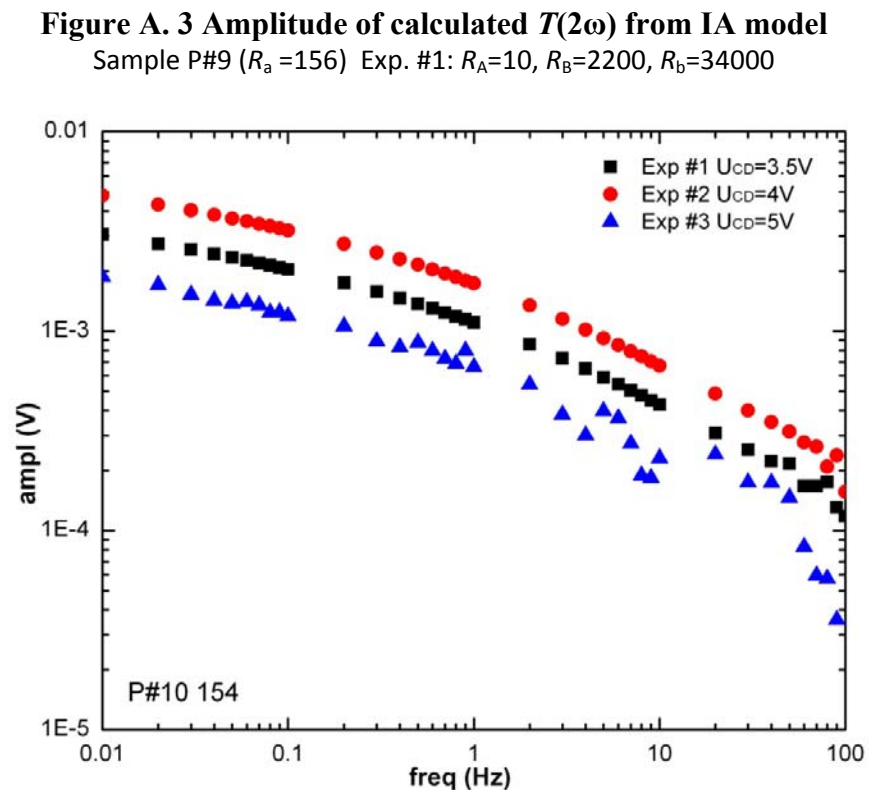
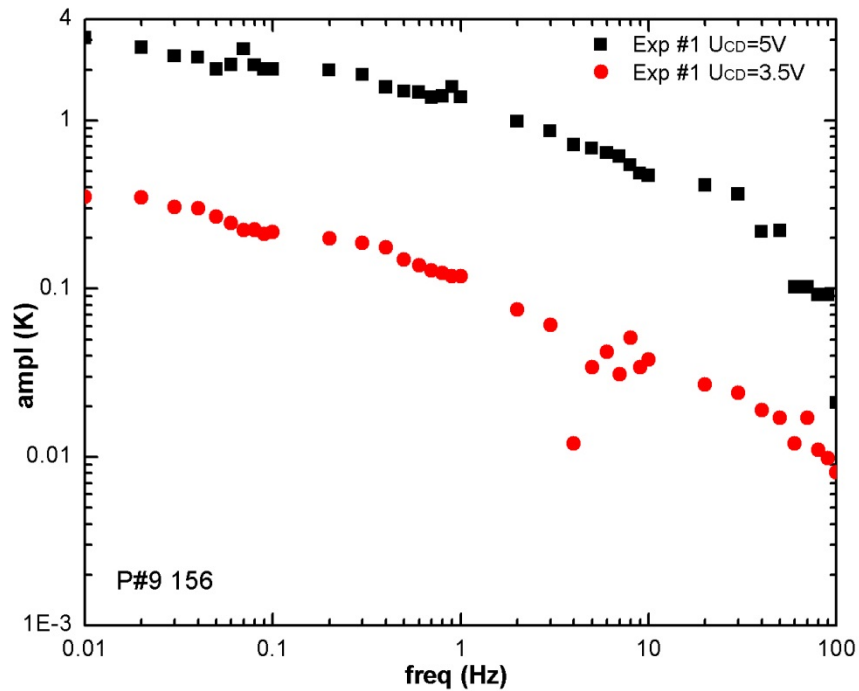
Figures A.7-A.8 plot the amplitude and phase data of temperature  $\Delta T(2\omega)$  converted from  $U_{AB}^{3\omega}$  using the impedance analysis model in frequency range [0.01 Hz-30 Hz] from Exp. #1 and #2. These data will be used for estimating the thermal parameters of sample P#10 in Chapter 5 and the obtained thermal property values from curvefitting these data and theoretical model agrees with handbook value very well.

**Sample P#14** Figures A9-A10 show the amplitude and phase data of  $U_{AB}^{3\omega}$  collected from Exp. #1, #2 and #3 under different  $U_{CD}$  of PMMA sample P#14 whose electrical resistance is  $162 \Omega$  at room temperature. It can be seen in frequency range [0.01 Hz-30 Hz] the amplitude and phase data from all the three experiments show great smoothness, especially the phase data from the two experiments are consistent with each other very well.

Figures A.11-A.12 plot the amplitude and phase data of temperature  $\Delta T(2\omega)$  converted from  $U_{AB}^{3\omega}$  using the impedance analysis model in frequency range [0.01 Hz-30 Hz] from the three experiments. It can be seen the maximum temperature rise in all these three experiments is also between 1.5 K and 3 K. Note that, in the three experiments,

different kinds of boundary conditions on the opposite-to-heating side are applied. The sample is placed on an aluminum block, a wood table and in air in the three experiments, respectively. In chapter 5, the Biot number corresponding different each experiment will be fit as a parameter along with other thermal properties.





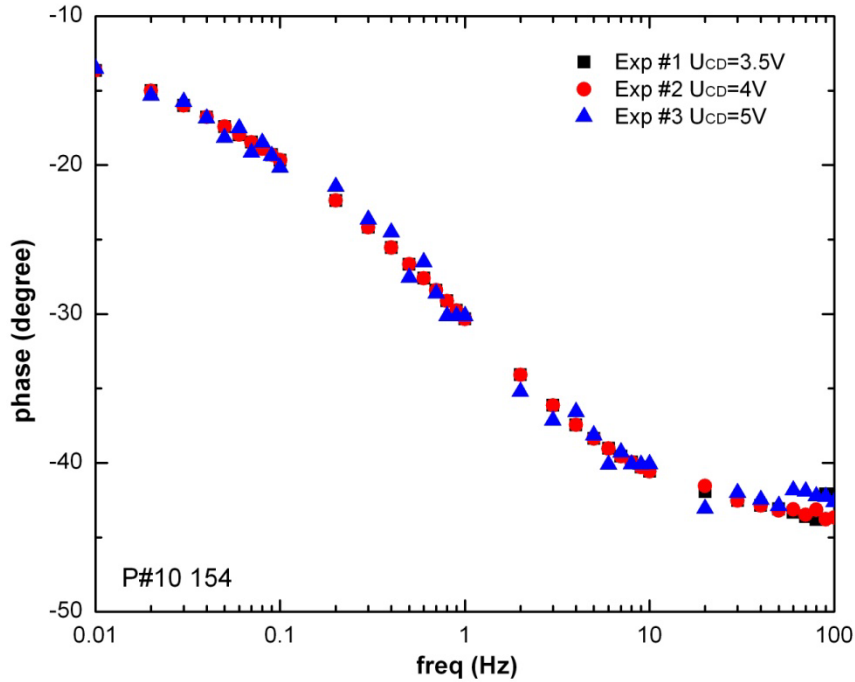
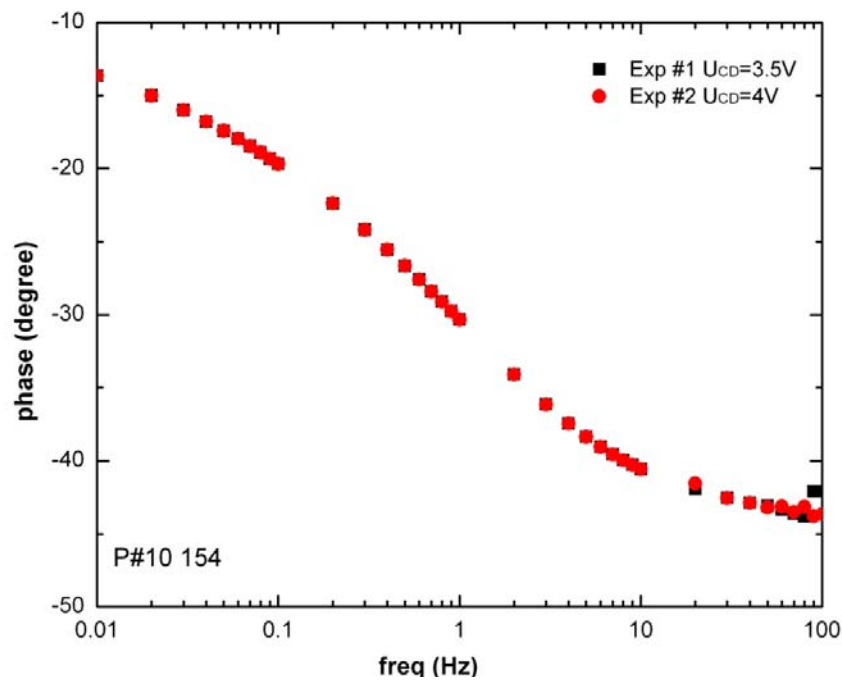


**Figure A. 5 Amplitude of  $U_{AB}^{3\omega}$  collected from measurement**

Sample P#10 ( $R_a = 154$ ) Exp. #1:  $R_A=30, R_B=2200, R_b=11200$

Exp. #2:  $R_A=40, R_B=2200, R_b=8400$

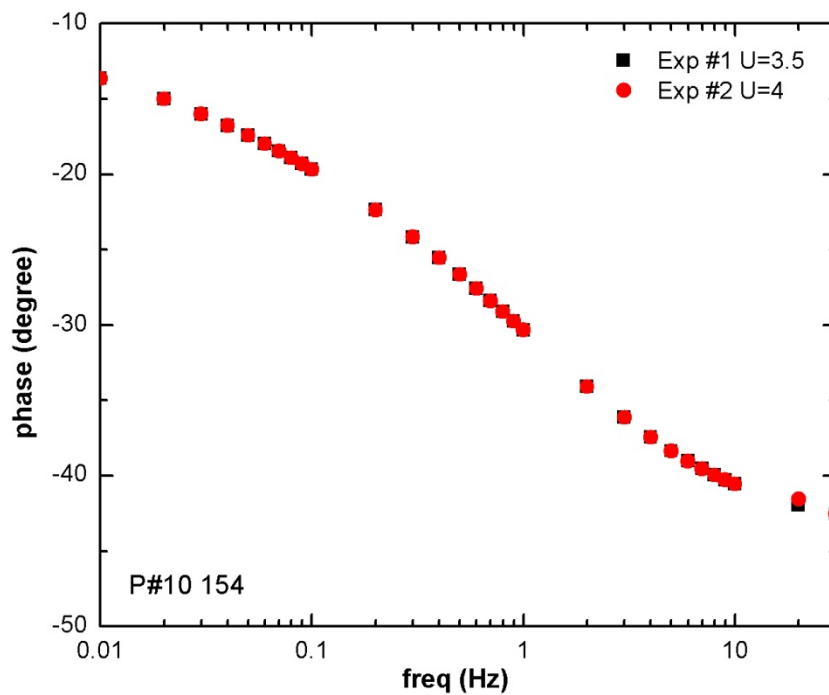
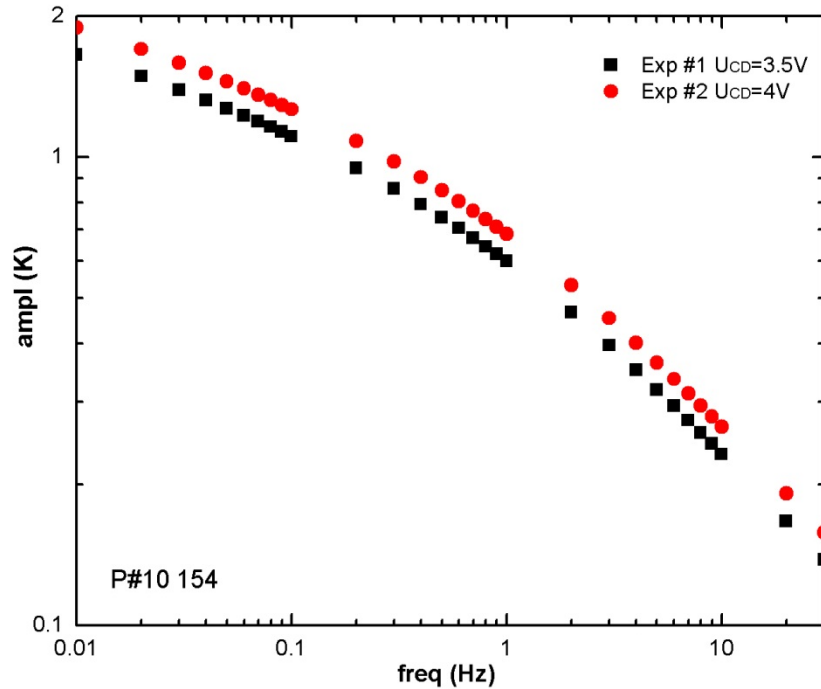
Exp. #3:  $R_A=5, R_B=2200, R_b=67000$



**Figure A. 6 Amplitude of  $U_{AB}^{3\omega}$  collected from measurement**

Sample P#10 ( $R_a = 154$ ) Exp. #1:  $R_A=30, R_B=2200, R_b=11200$

Exp. #2:  $R_A=40, R_B=2200, R_b=840$



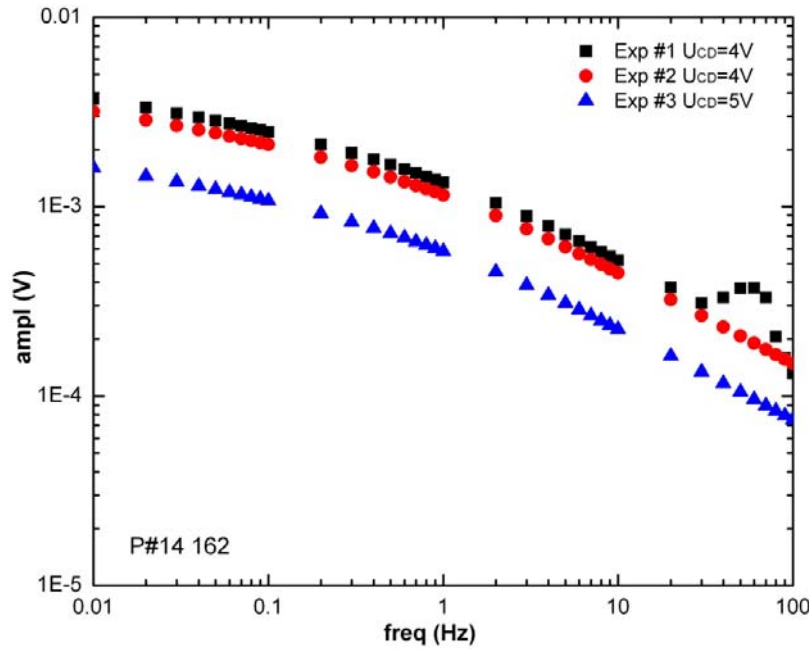


**Figure A. 9 Amplitude of  $U_{AB}^{3\omega}$  collected from measurement**

Sample P#14( $R_a = 162$ )  
 Exp. #1:  $R_A = 30, R_B = 2200, R_b = 11200$ ; sample placed on aluminum block  
 Exp. #2:  $R_A = 35, R_B = 2200, R_b = 11200$ ; sample placed on wood table  
 Exp. #3:  $R_A = 15, R_B = 2200, R_b = 11200$ ; sample placed in air

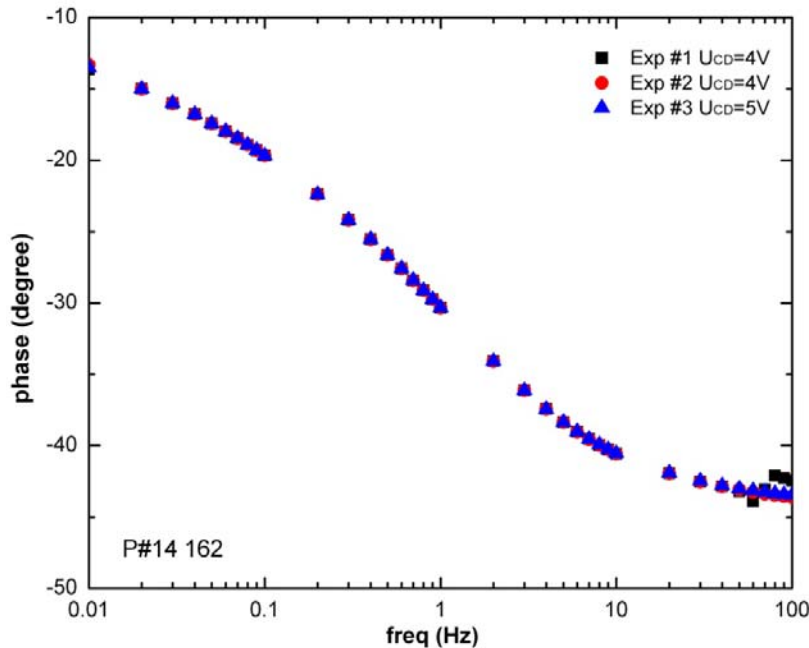
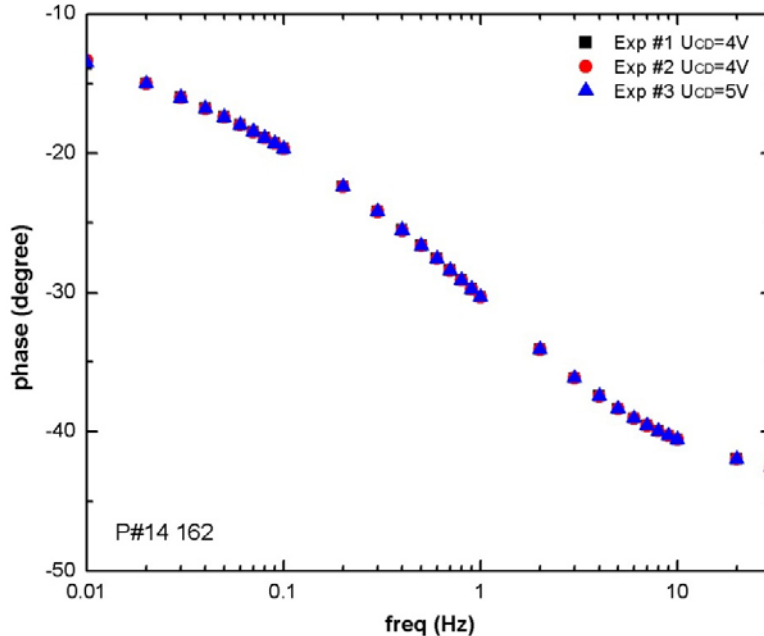
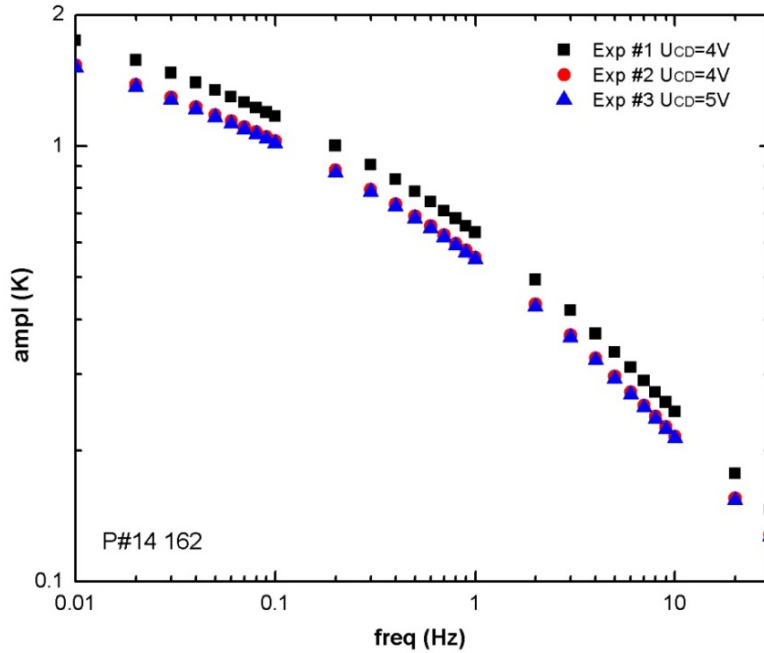


**Figure A. 10 phase of  $U_{AB}^{3\omega}$  collected from measurement**

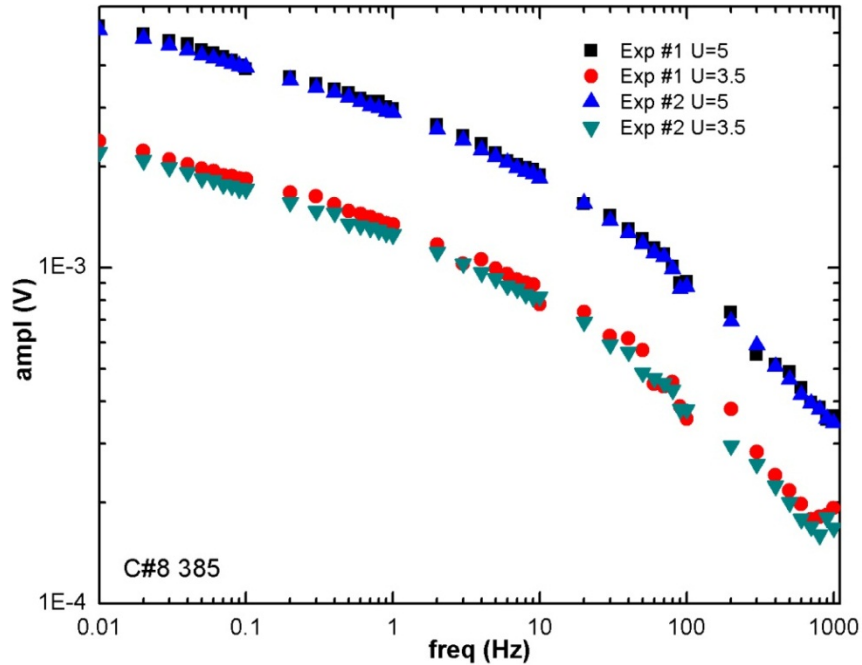
Sample P#14( $R_a = 162$ )  
 Exp. #1:  $R_A = 30, R_B = 2200, R_b = 11200$ ; sample placed on aluminum block  
 Exp. #2:  $R_A = 35, R_B = 2200, R_b = 11200$ ; sample placed on wood table  
 Exp. #3:  $R_A = 15, R_B = 2200, R_b = 11200$ ; sample placed in air



# **Appendix B.**

## **Experimental results from Sample C#8, #13 and #16**

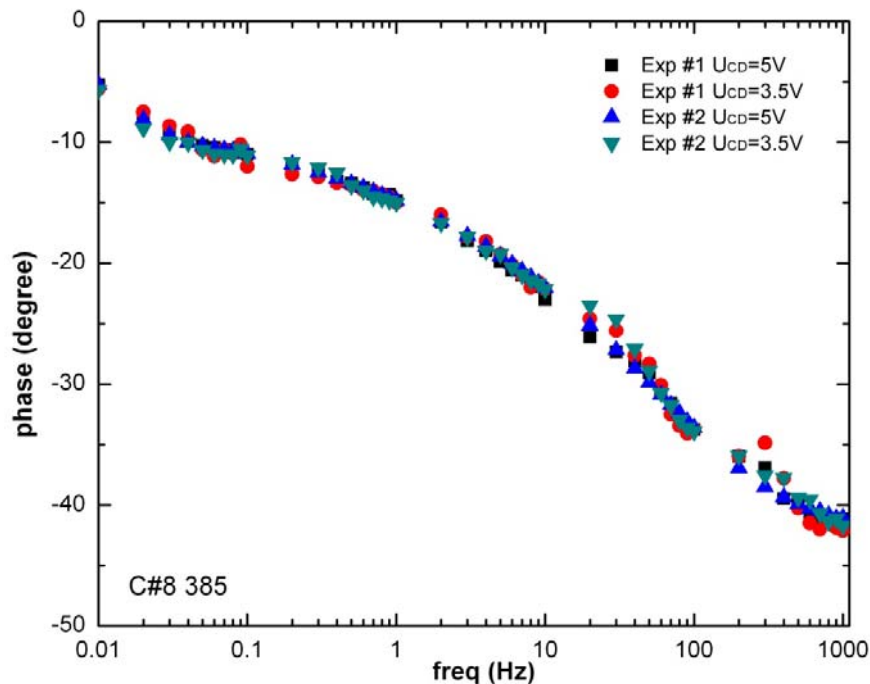
Figures B.1-B.6 show the samplitude and phase data of  $U_{AB}^{3\omega}$  collected from the measurements with carbon fiber sample C#8, C#13 and C#16 whose electrical resistance are  $385 \Omega$ ,  $381 \Omega$  and  $424 \Omega$  at room temperature, respectively. For each sample, two sets of experiments Exp. #1 and #2 where different resistor-combinations of  $R_A$ ,  $R_B$  and  $R_b$  are applied. In each experiment, amplitude and phase data are collected in frequency range [0.01 Hz-1000 Hz] at 46 discrete frequency points while all the other parameters are fixed. For each case with fixed resistor combination, two measurements were carried out where supplying signal  $U_{CD}^\omega$  with different magnitude of voltage ( $U_{CD}=5$  V, 3.5 V) were input. Figure B.7-B.12 present the amplitude and phase data of temperature  $\Delta T(2\omega)$  converted from  $U_{AB}^{3\omega}$  from Exp. #1 and #2 at  $U_{CD}=5$  V of the three samples.



**Figure B. 1 Amplitude of  $U_{AB}^{3\omega}$  collected from measurement**

Sample C#8 ( $R_a = 385$ ) Exp. #1:  $R_A=48.3, R_B=1773, R_b=13100$

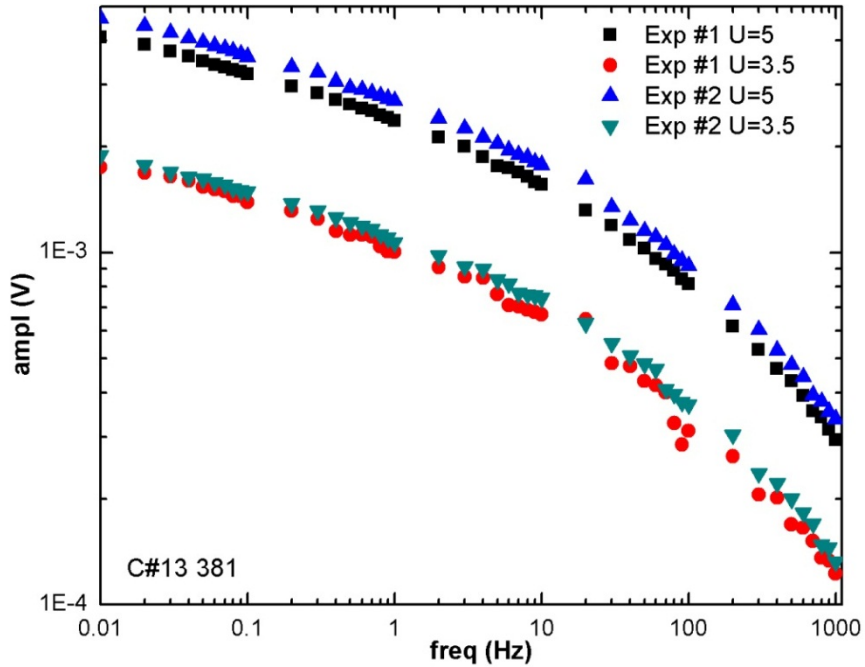
Exp. #2:  $R_A=30, R_B=2200, R_b=14268$



**Figure B. 2 Phase of  $U_{AB}^{3\omega}$  collected from measurement,**

Sample C#8 ( $R_a = 385$ ) Exp. #1:  $R_A=48.3, R_B=1773, R_b=13100$

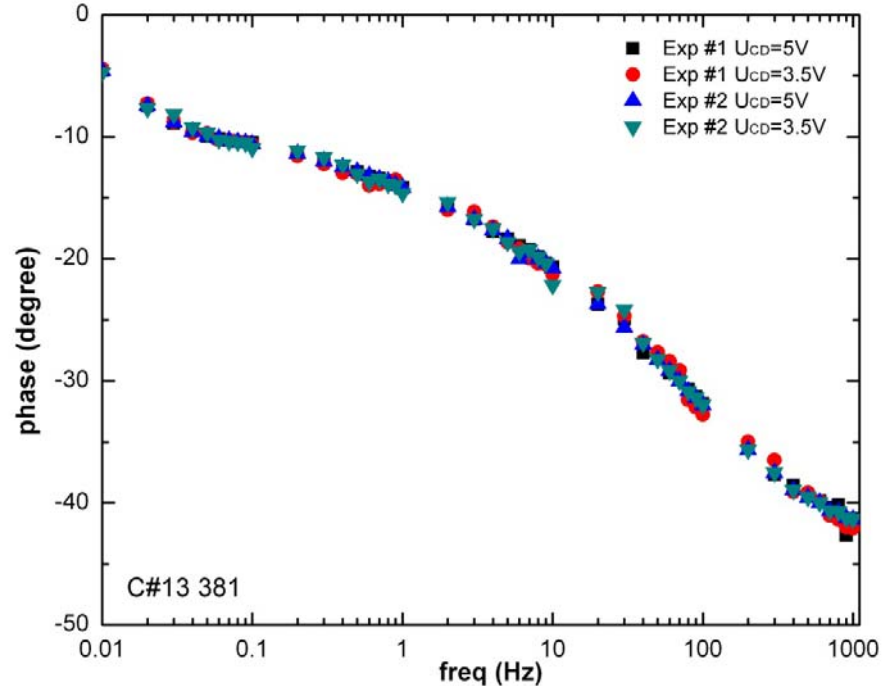
Exp. #2:  $R_A=30, R_B=2200, R_b=14268$



**Figure B. 3 Amplitude of  $U_{AB}^{3\omega}$  collected from measurement,**

Sample C#13 ( $R_a = 381$ ) Exp. #1:  $R_A=48.3, R_B=1773, R_b=14268$

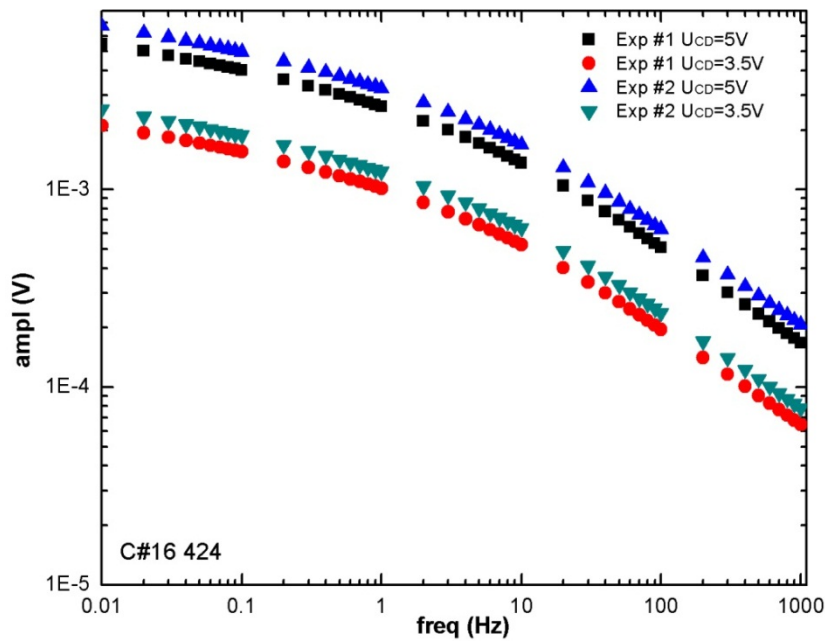
Exp. #2:  $R_A=48.3, R_B=1773, R_b=13100$



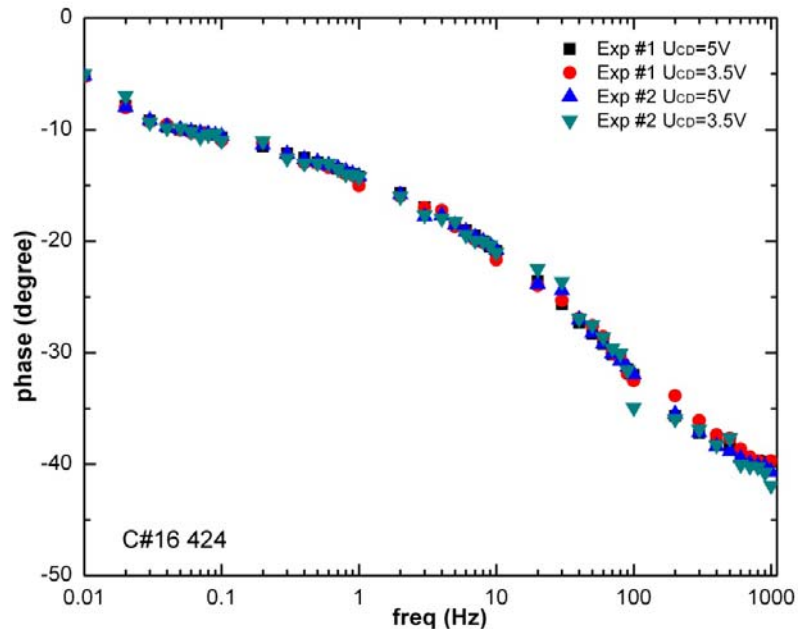
**Figure B. 4 Phase of calculated  $T(2\omega)$  from IA model**

Sample C#13 ( $R_a = 381$ ) Exp. #1:  $R_A=48.3, R_B=1773, R_b=14268$

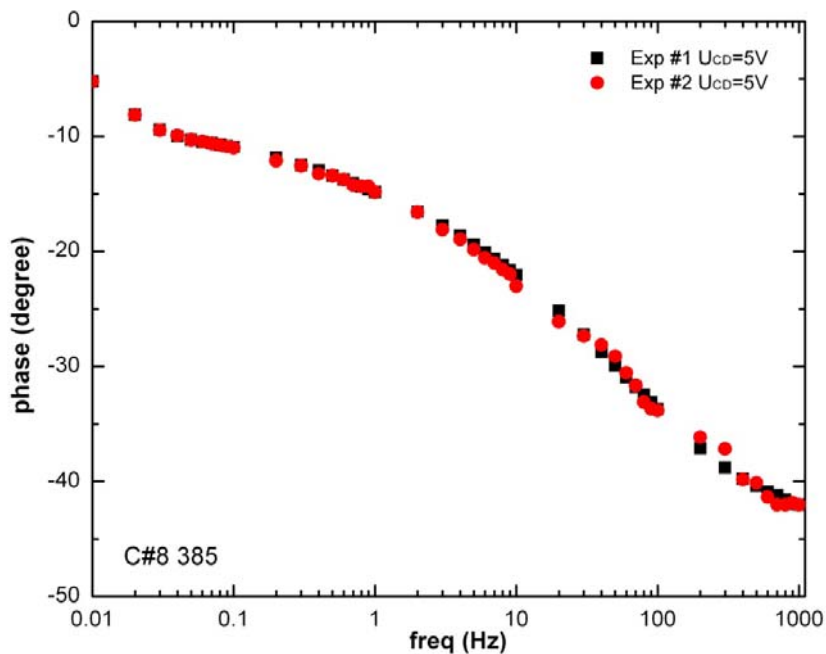
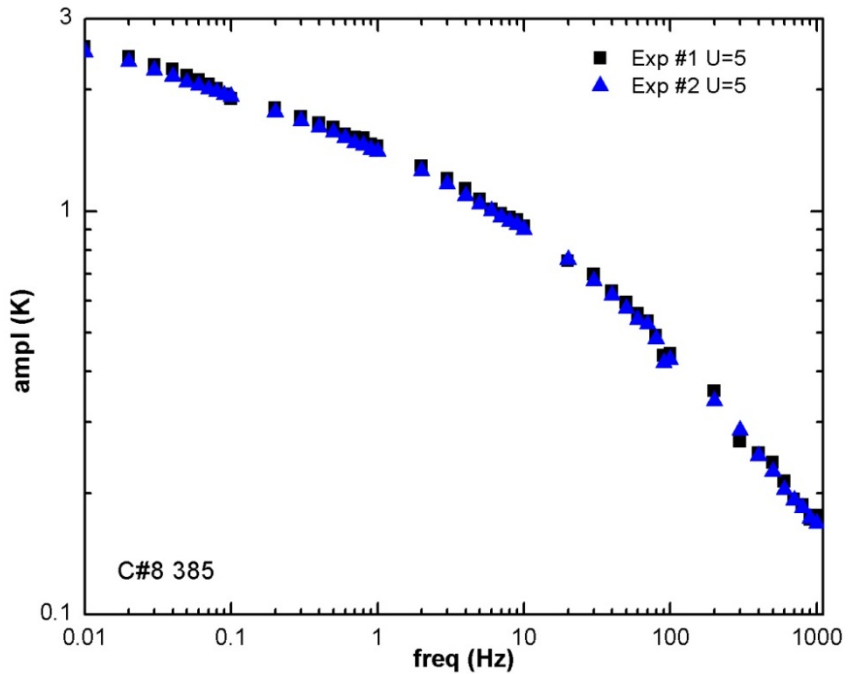
Exp. #2:  $R_A=48.3, R_B=1773, R_b=13100$

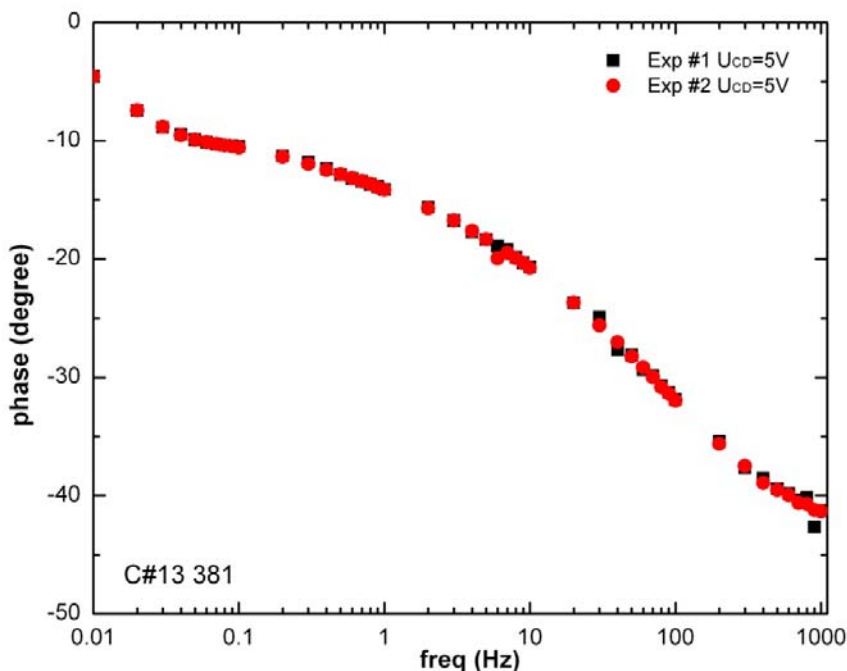
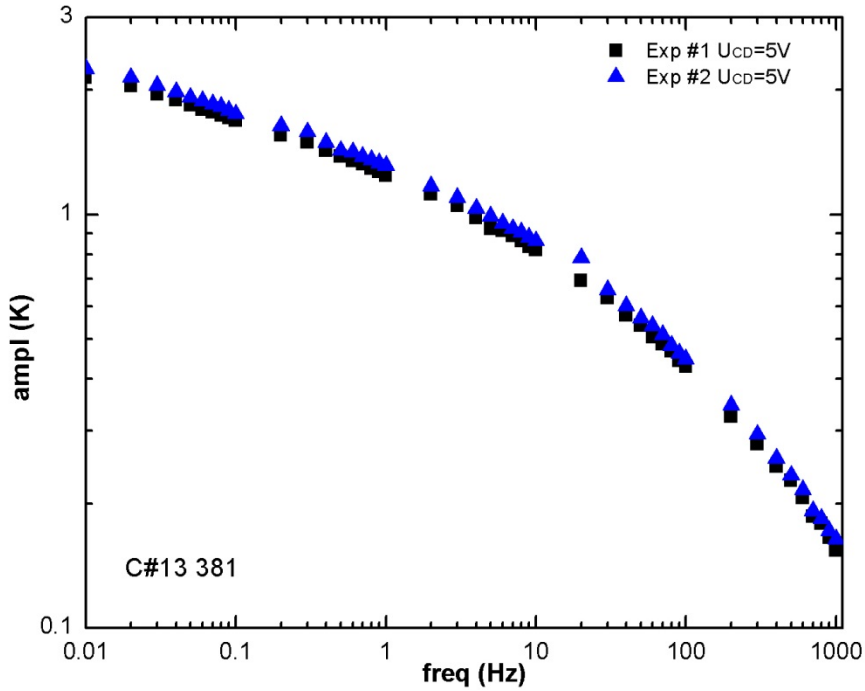


**Figure B. 5 Amplitude of  $U_{AB}^{3\omega}$  collected from measurement,**  
Sample C#16 ( $R_a = 424$ ) Exp. #1:  $R_A=51, R_B=2461, R_b=21200$   
Exp. #2:  $R_A=72, R_B=2461, R_b=21200$



**Figure B. 6 Phase of  $U_{AB}^{3\omega}$  collected from measurement**  
Sample C#16 ( $R_a = 424$ ) Exp. #1:  $R_A=51, R_B=2461, R_b=21200$   
Exp. #2:  $R_A=72, R_B=2461, R_b=21200$





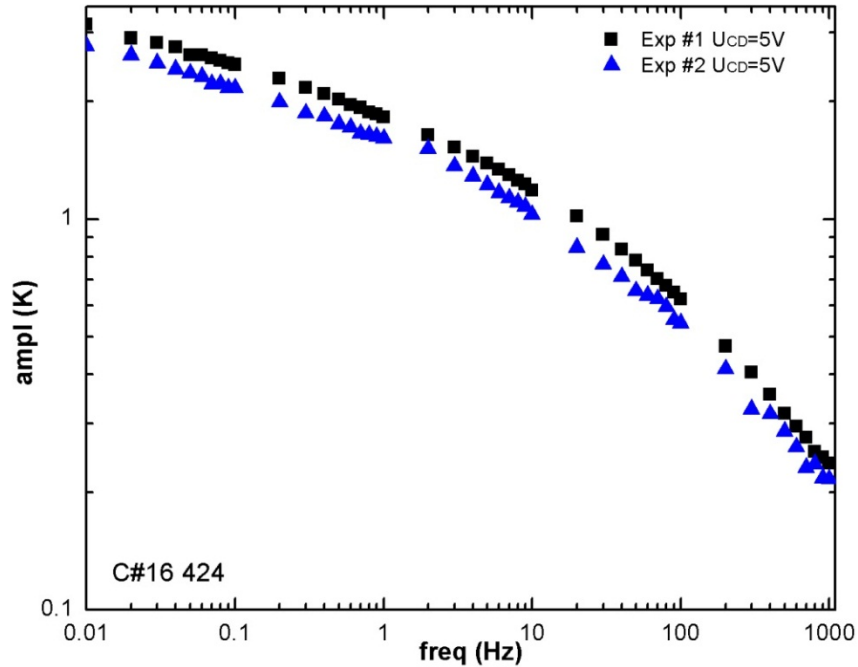


**Figure B. 11 Amplitude of calculated  $T(2\omega)$  from IA model**

Sample C#16 ( $R_a = 424$ ) Exp. #1:  $R_A = 51$ ,  $R_B = 2461$ ,  $R_b = 21200$

Exp. #2:  $R_A = 72$ ,  $R_B = 2461$ ,  $R_b = 14500$

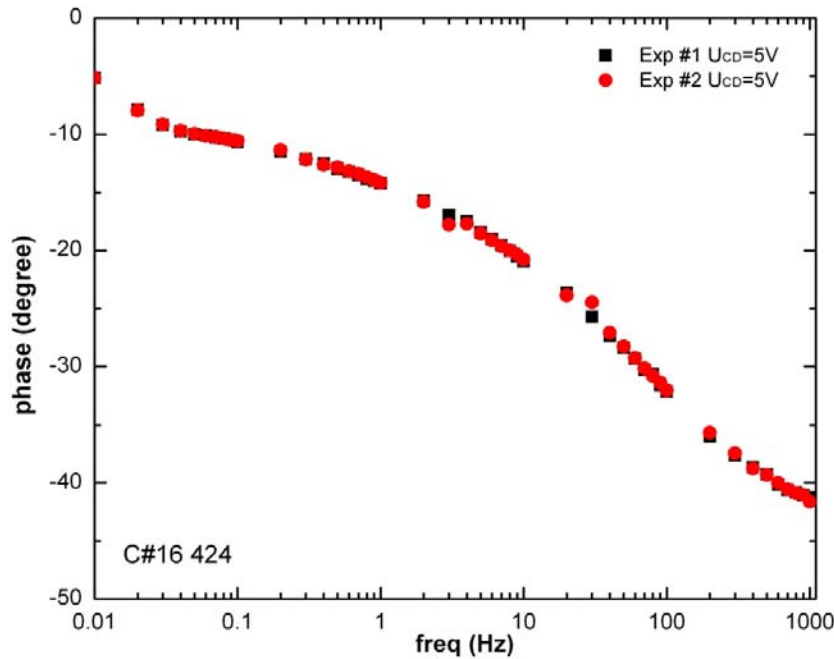


**Figure B. 12 Phase of calculated  $T(2\omega)$  from IA model**

Sample C#16 ( $R_a = 424$ ) Exp. #1:  $R_A = 51$ ,  $R_B = 2461$ ,  $R_b = 21200$

Exp. #2:  $R_A = 72$ ,  $R_B = 2461$ ,  $R_b = 14500$